UNIVERSITY OF CALIFORNIA, SAN DIEGO

Mechanically Compliant Electronic Materials for Wearable Photovoltaics and Human-Machine Interfaces

A dissertation submitted in partial satisfaction of the requirements for the degree Doctor of Philosophy

in

NanoEngineering

by

Timothy Francis O'Connor III

Committee in charge:

Professor Darren Lipomi, Chair
Professor Todd Coleman
Professor Shirley Meng
Professor Patrick Mercier
Professor Donald Sirbuly

2017

This Dissertation of Timothy Francis O'Connor III is approved, and it is acceptable in quality and form for publication on microfilm and electronically:

Chair

University of California, San Diego

2016

DEDICATION

This one is for single points and broken symmetry. For time and space, for matter and energy, for the forces, and for the light the ties them all together. For Aurora Borealis, for star monkies, for lucent love and zen beacons, for hellstorms and heavensgate, for dust and fire, for bass and symphony. For our ancestors down the unbroken chain of evolution, both human and stellar. For a universe in growth, seeking to understand ourself through billions of minds, and eyes, and ears, and hands, and noses, that it may know itself and its capabilities. This one is for the sun and moon, their dance drives day and night. This one's for the few in many. The weight of the many is carried on the shoulders of the few. This one is for Earth, our home, all that I have done, I have done for us, to help safeguard consciousness and higher order in this sector of the galaxy with the hopes that our success will lead to a human constellation, living symbiotically with our worlds using light to power our futures. Let's see what can be done next with this shield and this spear!

EPIGRAPH

It’s not about what’s necessary, it’s about what’s possible!

TABLE OF CONTENTS

SIGNATURE PAGE iii
DEDICATION iv
EPIGRAPH v
TABLE OF CONTENTS vi
LIST OF FIGURES viii
ACKNOWLEDGEMENTS x
VITA xiii
ABSTRACT OF THE DISSERTATION xvi
CHAPTER 1 – SOFT POWER: STRETCHABLE AND ULTRA-FLEXIBLE ENERGY SOURCES FOR WEARABLE AND IMPLANTABLE DEVICES 1
1.1 – ABSTRACT 1
1.2 – INTRODUCTION 2
1.3 – APPROACHES TO MAKING STRETCHABLE ELECTRONICS 4
1.4 – STRETCHABLE ENERGY HARVESTING TECHNOLOGIES 6
1.4.1 – PIEZOELECTRIC AND TRIBOELECTRIC DEVICES 6
1.4.2 – THERMOELECTRIC DEVICES 9
1.4.3 – PHOTOVOLTAIC DEVICES 12
1.5 – SYSTEM-LEVEL POWER REQUIREMENTS 16
1.6 – CONCLUSIONS AND CHALLENGES 18
1.7 – REFERENCES 20
CHAPTER 2 – STRETCHING AND CONFORMAL BONDING OF ORGANIC SOLAR CELLS TO HEMISPHERICAL SURFACES 24
2.1 – BROADER CONTEXT 24
2.2 – ABSTRACT 25
2.3 – INTRODUCTION 26
2.3 – RESULTS AND DISCUSSION 33
2.3.1 – DEPENDENCE OF MOLECULAR WEIGHT ON MECHANICAL COMPLIANCE OF P3ATS. 33
2.3.2 – DETERMINATION OF ONSET OF PLASTIC DEFORMATION 34
2.3.3 – CONFORMAL BONDING TO HEMISPHERICAL SUBSTRATES 34
2.3.4 – COMPUTATIONAL ANALYSIS OF STRAIN 36
2.3.5 – CRACKING BEHAVIOR 38
2.3.6 – MEASUREMENT OF PHOTOVOLTAIC PROPERTIES 40
2.3.6 – YIELD 43
2.4 – CONCLUSION 44
2.5 – EXPERIMENTAL METHODS 46
2.5.1 – MATERIALS 46
2.5.2 – FABRICATION OF DEVICES AND BONDING TO HEMISPHERICAL SURFACES 46
2.5.3 – FABRICATION OF DEVICES WITH THE CONVENTIONAL ARCHITECTURE 48
2.5.4 – FABRICATION OF DEVICES WITH THE INVERTED ARCHITECTURE 49
2.5.5 – COMPUTATIONAL MODELING OF STRAIN 50

2.5.6 – PHOTOVOLTAIC MEASUREMENTS. 50
2.6 – ACKNOWLEDGEMENTS 51
2.7 – REFERENCES 52
CHAPTER 3 – WEARABLE ORGANIC SOLAR CELLS WITH HIGH CYCLIC BENDING STABILITY: MATERIALS SELECTION CRITERIA 55
3.1 – ABSTRACT 55
3.2 – INTRODUCTION 56
3.3 – RESULTS AND DISCUSSION 58
3.4 – CONCLUSION 67
3.5 – METHODS 68
3.5.1 – MATERIALS 68
3.5.2 – FABRICATION OF WEARABLE SOLAR CELLS 69
3.5.3 – YIELD 70
3.5.4 – MECHANICAL SIMULATIONS. 71
3.5.5 – CYCLING STUDIES 72
3.5.6 – CRACK-ONSET MEASUREMENTS 72
3.5.7 – BARRIER STUDIES 73
3.5.8 – POWERING DEVICES 73
3.6 – ACKNOWLEDGEMENTS 74
3.7 – REFERENCES 74
CHAPTER 4 – THE LANGUAGE OF GLOVE: WIRELESS GESTURE DECODER WITH LOW-POWER AND STRETCHABLE HYBRID ELECTRONICS 78
4.1 – ABSTRACT 78
4.2 – INTRODUCTION 79
4.3 – MATERIALS AND METHODS 81
4.3.1 – FABRICATION OF PIEZORESISTIVE STRAIN SENSORS 81
4.3.2 – CHARACTERIZATION OF STRAIN SENSORS 81
4.3.3 – FABRICATION OF THE SENSOR GLOVE 82
4.3.4 – DESIGNING THE CIRCUIT BOARD 82
4.3.5 – FINITE ELEMENT ANALYSIS 82
4.3.6 – LETTER SELECTION 83
4.3.7 – CODE 83
4.3.8 – VIRTUAL HAND 83
4.4 – RESULTS AND DISCUSSION 84
4.5 – CONCLUSION 91
4.6 – SUPPORTING INFORMATION 93
4.6.1 – PARTS LIST AND COST 93
4.6.2 – FABRICATION SCHEMATIC OF PIEZORESISTIVE STRAIN SENSORS. 93
4.7.3 PCB SCHEMATICS AND CIRCUIT DIAGRAMS 94
4.6.4 – KEY GENERATION TABLE 101
4.6.5 – DEGENERATE LETTER DETERMINATION 101
4.7 – ACKNOWLEDGEMENTS 102
4.8 – REFERENCES 102

LIST OF FIGURES

Figure 1: Total power available from body-driven sources in comparison to sunlight and artificial light sources. 4
Figure 2: Images of representative samples of strategies for engineering stretchable electronics 6
Figure 3: Representative examples of piezoelectric and triboelectric devices that are possible for bio-integration. 8
Figure 4: Wearable thermoelectric devices. 11
Figure 5: Stretchable photovoltaic devices.. 14
Figure 6: Order of magnitude of typical power consumption of biomedical devices and the range of power generation by the four technologies outlined in this chapter. 18
Figure 7: Graphical abstract depicting schematic of the stretchable hemispherical solar cell. 24
Figure 8: Summary of the process used to transfer multilayer films of conjugated polymers to a hemispherical glass substrate. 28
Figure 9: Conventional (top) vs. inverted (bottom) geometries of organic solar cells 36
Figure 10: Computational analysis of the strain produced in the thin films when they are transferred to the hemispherical surfaces 38
Figure 11: Photographs of conjugated polymer films stretched and bonded to hemispherical surfaces 40
Figure 12: Representative photovoltaic characteristics of organic solar cells bonded to hemispherical substrates 42
Figure 13: Schematic drawings of the successful (a) and unsuccessful (b) processes intended to transfer the PEDOT:PSS top contact to the glass/PEDOT:PSS/PEI/P3AT:PCBM device bonded to a glass substrate.. 44
Figure 14: Fabrication of ultra-flexible, wearable OSCs. a) Schematic summary of the process used to fabricate wearable OSCs. 60
Figure 15: Crack onset strains on polymeric supports for different material 61
Figure 16: Mechanical deformation of OSCs on skin.. 62
Figure 17: Electrical characteristics of wearable solar cells with mechanical deformation and in the outdoor environment. 64
Figure 18: Applications of wearable OSCs. 67
Figure 19: Overview of the gesture-decoding glove. 86
Figure 20: Overview of the wearable piezoresistive sensors. 88
Figure 21: Characterization of the piezoresistance and FEA strain modeling of the sensors. 90
Figure 22: Process by which the glove converted gestures into the letters of ASL. 91
Figure 23: Cost of parts to fabricate the sensor glove. 93
Figure 24: Fabrication schematic of the piezoresistive sensors. 93
Figure 25: Image of the EAGLE CAD board. 94
Figure 26: EAGLE CAD circuit schematic for the power system.**Error! Bookmark not defined.**
Figure 27: EAGLE CAD circuit schematic for the microcontroller. 96

Figure 28: EAGLE CAD circuit schematic for the Bluetooth system. 97
Figure 29: EAGLE CAD circuit schematic for the thumb sensor. 97
Figure 30: EAGLE CAD circuit schematic for the index sensors. 98
Figure 31: EAGLE CAD circuit schematic for the middle finger sensors. 98
Figure 32: EAGLE CAD circuit schematic for the ring finger sensors. 99
Figure 33: EAGLE CAD circuit schematic for the pinky sensor system. 99
Figure 34: EAGLE CAD circuit schematic for the touch sensor (two were designed, only one was needed) 100
Figure 35: EAGLE CAD circuit schematic for the accelerometer/gyroscope. 100
Figure 36: Key generation table indicating which letters correspond to which keys. ... 101
Figure 37: Table depicting the serial outputs of the parameters used to differentiate between letters with degenerate keys. 101

ACKNOWLEDGEMENTS

I would like to express my highest acknowledgements and appreciation to the following humans, whom in concert with time and circumstance made this experience illuminating, empowering, inspiring, and worth undergoing!!

I acknowledge my advisor, Dr. Darren Lipomi, for his continuously growing wisdom and leadership which he shared with all of us, for his boundless care and understanding for our futures and wellbeings, and for his ability and vision to build and create. Seriously, Darren is some sort of high powered mutant never considered for mass production. I cannot express in this paragraph how grateful I am to have learned from him, but he is an incredible leader, mentor, and friend.

I acknowledge Dr. Suchol Savagatrup, who's friendship, intelligence, and organization are completely off the chain! Many of the projects covered in this dissertation are applications based on Suchol's hard work in fundamental materials research. I'm honored by the symbiosis of our research and I'm excited to see where your academic career takes you!

I acknowledge Dr. Alex Zaretski, who loves grapheme more than anyone I've ever met and who's determination, and creativity are a sight to behold! It was an honor to work with you to push the labs applications fronts and it was inspiring to watch you turn your dreams into reality and build a company. Cheers, Alex!!

I acknowledge Dr. Adam Printz, for his guidance and dedication. This guy! This guy is absolutely awesome, was always down to help and has a fantastic intuition for the

science, engineering, and for organizations. Heavy respect for you Adam, for being the first grad student in being a key part of the labs startup and culture.

I acknowledge Sam Root for his truly impressive and self-taught work in dynamics and simulations, and for his adventurous spirit! I learned so much from you Sam, thank you for joining me on some of my radical adventures.

I acknowledge Rachel Miller for being a capable and supportive apprentice! Rachel, you have a brilliant future ahead of you and I appreciate you for helping me pull these last projects off! I couldn't have done it without you!

And I acknowledge the all of the members of the Lipomi Lab for being the best group of humans to build something incredible with. This lab and its community represented purpose, friendship, and family to me, and I gave it my all because of you.

Life is more than what we do, but how we do it and who we do it with. It was an honor to contribute to our species wealth of knowledge and design new applications with the best teammates and friends around.

Chapter 1, in full, is a reprint of the material as it appears in "Soft Power: Stretchable and Ultra-Flexible Energy Sources for Wearable and Implantable Devices," Timothy F. O'Connor, Suchol Savagatrup, and Darren J. Lipomi. Stretchable Bioelectronics for Medical Devices and Systems, 2016. The dissertation author was the primary investigator and author of this paper.

Chapter 2, in full, is a reprint of the material as it appears in "Stretching and conformal bonding of organic solar cells to hemispherical surfaces," Timothy F. O'Connor, Aliaksandr V. Zaretski, Bijan A. Shiravi, Suchol Savagatrup, Adam D. Printz,

Mare Ivana Diaz, Darren J. Lipomi. Energy & Environmental Science, 2014. The dissertation author was the primary investigator and author of this paper.

Chapter 3, in full, is a reprint of the material as it appears in . “Wearable organic solar cells with high cyclic bending stability: Materials selection criteria,” Timothy F. O’Connor, Aliaksandr V. Zaretski, Suchol Savagatrup, Adam D. Printz, Cameron D. Wilkes, Mare Ivana Diaz, Eric J. Sawyer, and Darren J. Lipomi. Solar Energy Materials and Solar Cells, 2016. The dissertation author was the primary investigator and author of this paper.

Chapter 4, in full, is a reprint of the material as it appears in “The Language of Glove: Wireless gesture decoder with low-power and stretchable hybrid electronics,” Timothy F. O’Connor, Matthew Fach, Rachel Miller, Samuel E. Root, Patrick P. Mercier, and Darren J. Lipomi.PLoS ONE, 2017. The dissertation author was the primary investigator and author of this paper.

VITA

2010 Bachelor of Science in Applied Physics, Bowling Green State University

2012 Master of Science in Physics, Bowling Green State University

2013 Master of Science in NanoEngineering, University of California, San Diego

2017 Doctor of Philosophy in NanoEngineering, University of California, San Diego

PUBLICATIONS

18. **T. F. O'Connor**, M. Fach, R. Miller, S. Root, D. J. Lipomi. "The Language of Glove: Wireless Gesture Decoder with Low-Power and Stretchable Hybrid Electronics." *PLOS ONE*.

17. S. Savagatrup, A. Printz, **T. F. O'Connor**, I. Kim, D. J. Lipomi. "Efficient Characterization of Bulk Heterojunction Films by Mapping Gradients by Reversible Contact with Liquid Metal Top Electrodes." *Chemistry of Materials*, **2017,** 389.

16. **T. F. O'Connor,** S. Savagatrup, D.J. Lipomi. "Soft Power: Stretchable and Ultra-flexible Energy Sources for Wearable and Implantable Devices." Invited for: Stretchable Bioelectronics for Medical Devices and Systems. J. A. Rogers, D. H. Kim, and R. Ghaffari, Editors. Springer Publishing Company, **2016**.

15. **T. F. O'Connor**, A. V. Zaretski, S. Savagatrup, A. D. Printz, C. D. Wilkes, M. I. Diaz, E. J. Sawyer, D. J. Lipomi. "Wearable Organic Solar Cells with High Cyclic Bending Stability: Materials Selection Criteria." *Solar Energy Materials & Solar Cells*, **2015**, 144, 438.

14. **T. F. O'Connor**, K. M. Rajan, A. D. Printz, D. J. Lipomi. "Toward organic electronics with properties inspired by biological tissue." *Journal of Materials Chemisty B*, **2015**, 3, 4947.

13. A. V. Zaretski, H. Moetazedi, C. Kong, E. Sawyer, S. Savagatrup, E. Valle, **T. F. O'Connor**, A. D. Printz, D. J. Lipomi. "Metal-assisted exfoliation (MAE): Green, roll-to-roll compatible methods for transferring graphene to flexible substrates." *Nanotechnology*, **2015**, 26, 4.

12. S. Savagatrup, E. Chan, S. M. Renteria-Garcia, A. D. Printz, A. V. Zaretski, **T. F. O'Connor**, D. Rodriquez, E. Valle, D. J. Lipomi. "Plasticization of PEDOT:PSS by

Common Additives for Mechanically Robust Devices and Wearable Sensors." *Advanced Functional Materials*, **2015**, 25.

11. S. Savagatrup, A. D. Printz, **T. F. O'Connor**, A. V. Zaretski, D. Rodriquez, E. J. Sawyer, K. M. Rajan, R. I. Acosta, S. E. Root, D. J. Lipomi. "Mechanical degradation and stability of organic solar cells: molecular and microstructural determinants." *Energy and Environmental Science* **2015**, 8, 55.

10. E. J. Sawyer, S. Savagatrup, **T. F. O'Connor**, A. S. Makaram, D. J. Burke. A. V. Zaretski, A. D. Printz, D. J. Lipomi, "Toward Intrinsically Stretchable Organic Semiconductors: Mechanical Properties of High-Performance Conjugated Polymers." *Proc. SPIE*, **2014**, 9185, 991850U-1.

9. S. Savagatrup, A. D. Printz, **T. F. O'Connor**, A. V. Zaretski, D. J. Lipomi. "Molecularly Stretchable Electronics." *Chemistry of Materials*, **2014**, 26, 3028.

8. **T. F. O'Connor**, A. V. Zaretski, B. A. Shiravi, S. Savagatrup, A. D. Printz, M. I. Diaz, D. J. Lipomi. "Stretching and Conformal Bonding of Organic Solar Cells to Non-Planar Substrates." *Energy and Environmental Science*, **2014**, 7.

7. **T. F. O'Connor**, M. Zamkov. "Optical Properties of Nanocomposites." Invited for: UV-Vis and Photoluminescence Spectroscopy for Nanomaterials Characterization, Springer Publishing Company, **2013**.

6. D. Perera, R. Lorek, R. Khnayzer, P. Moroz, **T. F. O'Connor**, D. Khon, G. Diederich, E. Kinder, S. Lambright, F. Castellano, M. Zamkov. "Photocatalytic Activity of Core/Shell Semiconductor Nanocrystals Featuring Spatial Separations of Charges." *Journal of Physical Chemistry C*. **2012**, 116, 22786.

5. E. Khon, S. Lambright, D. Khon, B. Smith, **T. F. O'Connor**, P. Moroz, M. Imboden, G. Diederich, C. Perez-Bolivar, P. Anzenbacher, M. Zamkov. "Inorganic Solids of CdSe Nanocrystals Exhibiting High Emission Quantum Yield." *Advanced Functional Materials*. **2012**, 22, 3714.

4. **T. F. O'Connor**, M. Panov, A. Mereshchenko, A. Tarnovsky, R. Lorek, D. Perera, G. Diederich, S. Lambright, M. Imboden, M. Zamkov. "The Effect of the Charge-Separating Interface on Exciton Dynamics in Photocatalytic Colloidal Heteronanocrystals." *ACS Nano*. **2012**, 6, 8156.

3. E. Kinder, P. Moroz, G. Diederich, A. Johnson, M. Kirsanova, A. Nemchinov, **T. F. O'Connor**, D. Roth, M. Zamkov. "Fabrication of All-Inorganic Nanocrystal Solids through Matrix Encapsulation of Nanocrystal Arrays." *Journal of the American Chemical Society*, **2011**, 133, 20488.

2. K. P. Acharya, R. S. Khnayzer, **T. F. O'Connor**, G. Diederich, M. Kirsanova, A. Klinkova, D. Roth, E. Kinder, M. Imboden, M. Zamkov. "The Role of Hole Localization in Sacrificial Hydrogen Production by Semiconductor-Metal Heterostructured Nanocrystals." *Nano Letters,* **2011**, 11, 2919.

1. K. P. Acharya, E. Khon, **T. F. O'Connor**, I. Nemitz, A. Klinkova, R. S. Khnayzer, P. Anzenbacher, M. Zamkov. "Heteroepitaxial Growth of Colloidal Nanocrystals onto Substrate Films via Hot-Injection Routes." *ACS Nano*, **2011**, 5, 9299.

FIELDS OF STUDY

Major Fields: NanoEngineering and Applied Physics

Studies in Stretchable Electronic Materials and Devices
Professor Darren Lipomi

Studies in Nanocrystal Photophysics and Optoelectonic Devices
Professor Mikhail Zamkov

ABSTRACT OF THE DISSERTATION

Mechanically Compliant Electronic Materials for Wearable Photovoltaics and Human-Machine Interfaces

by

Timothy Francis O'Connnor III

Doctor of Philosophy in NanoEngineering

University of California, San Diego, 2017

Professor Darren Lipomi, Chair

Applications of stretchable electronic materials for human-machine interfaces are described herein. Intrinsically stretchable organic conjugated polymers and stretchable electronic composites were used to develop stretchable organic photovoltaics (OPVs), mechanically robust wearable OPVs, and human-machine interfaces for gesture recognition, American Sign Language Translation, haptic control of robots, and touch emulation for virtual reality, augmented reality, and the transmission of touch. The stretchable and wearable OPVs comprise active layers of poly-3-alkylthiophene:phenyl-

C_{61}-butyric acid methyl ester (P3AT:PCBM) and transparent conductive electrodes of poly(3,4-ethylenedioxythiophene)-poly(styrenesulfonate) (PEDOT:PSS) and devices could only be fabricated through a deep understanding of the connection between molecular structure and the co-engineering of electronic performance with mechanical resilience. The talk concludes with the use of composite piezoresistive sensors two smart glove prototypes. The first integrates stretchable strain sensors comprising a carbon-elastomer composite, a wearable microcontroller, low energy Bluetooth, and a 6-axis accelerometer/gyroscope to construct a fully functional gesture recognition glove capable of wirelessly translating American Sign Language to text on a cell phone screen. The second creates a system for the haptic control of a 3D printed robot arm, as well as the transmission of touch and temperature information.

CHAPTER 1 – SOFT POWER: STRETCHABLE AND ULTRA-FLEXIBLE ENERGY SOURCES FOR WEARABLE AND IMPLANTABLE DEVICES

Timothy F. O'Connor, Suchol Savagatrup, and Darren J. Lipomi*

Department of NanoEngineering, University of California, San Diego

9500 Gilman Drive, Mail Code 0448, La Jolla, CA 92093-0448

1.1 – ABSTRACT

The development of ultra-compliant power sources is prerequisite to the realization of imperceptible biomedical systems destined to be worn or implanted in the human body. This chapter assesses the viability of conformal piezo- and triboelectric, thermoelectric, and photovoltaic technologies as power sources for biomedical applications. It begins by identifying the amount of energy available to each these modes of power conversion and then gives a brief overview on the methods of fabricating stretchable electronic devices using deterministic structures, random composites, or molecularly stretchable electronic materials. The text then provides a detailed description of innovations in "soft power," where the mentioned design techniques have been employed to develop mechanically compliant power scavengers amenable to integration with stretchable medical devices. The chapter concludes with an analysis of system level power requirements and application specific compatibility, the result of which identifies piezoelectrics and triboelectrics as well suited for intermittent and implantable devices, such as low power pacemakers for piezoelectrics or higher power wearables and neural stimulators for triboelectrics. Thermoelectrics are highly compatible with epidermal and

wearable applications, and can be used as a consistent source of power for tattoo chemical or heat sensors, and photovoltaics can generate large amounts of power in full sun, for high power applications like cochlear implants, or less energy in diffuse or ambient light, for powering hearing aids.

1.2 – INTRODUCTION

An attractive aspect of biointegrated electronics from the standpoint of the research community is the opportunity to reimagine the components of conventional microelectronics.[1–7] Rigid integrated circuits on planar substrates—always connected to a stable source of power—must be transformed into form factors that can conform to the curved and soft surfaces of biological tissue, and which must store or harvest their own power. Delivering, managing, and harvesting energy to power these implantable and wearable devices are critical to the development of this technology.[8,9] Seamless integration of stretchable power sources into biomedical devices requires the development of "soft power"—highly deformable systems for harvesting and storing energy. This chapter will highlight strategies that enable the design and production of stretchable and ultra-flexible devices for energy harvesting. We define stretchability and ultra-flexibility by the capacity to withstand significant deformation without degradation in performance. We identify four relevant technologies (piezoelectric, triboelectric, thermoelectric, and photovoltaic), their potential applications based on availability of power sources, method of transduction, and the performance of the devices (i.e., power output, lifetime of the device, and mechanical properties), and methods of producing them in form factors that are highly deformable.

We preface this chapter by describing the availability of the viable sources of power, **Figure 1**. Scavenging energy from the human body could potentially be one of the most convenient methods of powering and extending the operation of biomedical devices.[8] At rest, the human body generates roughly 7 W of power (~4 W from heat, 2 W from breathing, and 1 W from blood pressure).[10] When in motion, the human body has an additional 130 W of kinetic power available, along with a small amount of power, on the order of 10 mW, that can be collected from small motions of extremities.[10] Physical methods of energy harvesting are usually based on transducers utilizing mechanical energy, such as heart beats,[11] blood flow,[12] walking,[13,14] breathing,[15] and stretching of muscles.[16] Methods of harvesting additional energy from the components of sweat—i.e., bioelectrocatalytic glucose oxidation[17–19]—are exciting developments in the field,[20] but our focus is on power that can be harvested from physical motions of the human body and from ambient light. In particular, the sun (which provides around 100 mW cm^{-2} under ideal conditions) and indoor light sources can provide power on the order of 1 mW cm^{-2}. Current wearable biomedical devices have power requirements ranging from 1 μW to 100s of mW, thus the energy available from the human body and external light sources may be sufficient to power these devices.[21] (For the sake of space, we do not cover mechanically compliant devices for energy storage, but direct the reader to the work of others in this area.[22–24])

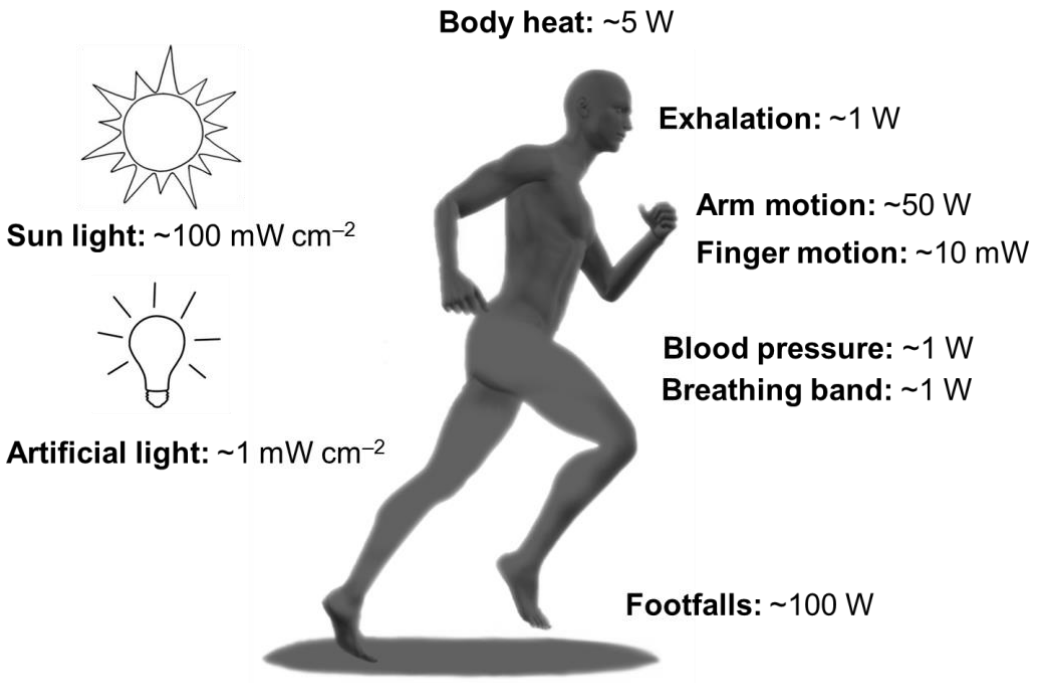

Figure 1: Total power available from body-driven sources in comparison to sunlight and artificial light sources. Adapted from Ref. [10]

1.3 – APPROACHES TO MAKING STRETCHABLE ELECTRONICS

Three main strategies have been identified for developing stretchable electronics (**Figure 2**).[25] The first involves the top-down fabrication of deterministic structures that render otherwise rigid materials (e.g., silicon, metals, and ceramics) stretchable by converting global strains into local deformations of the components on a macroscopic scale. These technologies often use an "island-bridge" approach, whereby rigid components (islands) fabricated on or in a stretchable matrix are connected by fractal or serpentine interconnects (bridges).[26,27] Devices can also be compressed to create sinusoidal structures through buckling instabilities.[28] These structures transfer the strain associated with elongation into a decrease in the amplitude (and corresponding increase

in the wavelength) of the buckled structures. The second method—random composites—takes advantage of high aspect ratio structures (i.e., nanowires or nanotubes) that form contiguous networks when deposited on or in some elastic support.[29–32] As the device is stretched, one-dimensional structures undergo configurational changes (i.e., rotation, straightening, sliding past each other), rather than fracturing, allowing electronic performance to be maintained whilst deformed. Using this method, stretchable electrodes have been fabricated that can accommodate over 400% strain.[33] The third, complementary approach is intrinsically stretchable electronics, where the active electronic layers themselves accommodate the strain.[25,29,34] These devices are generally made from solution processable organic materials, which in principle are amenable to high-throughput fabrication techniques.[35] The challenge of intrinsically—or "molecularly"[25]—stretchable systems is that electronic and mechanical properties are generally mutually antagonistic, and thus a material exhibiting state-of-the-art semiconducting properties with the mechanical properties of an elastomer has not yet been demonstrated.[36]

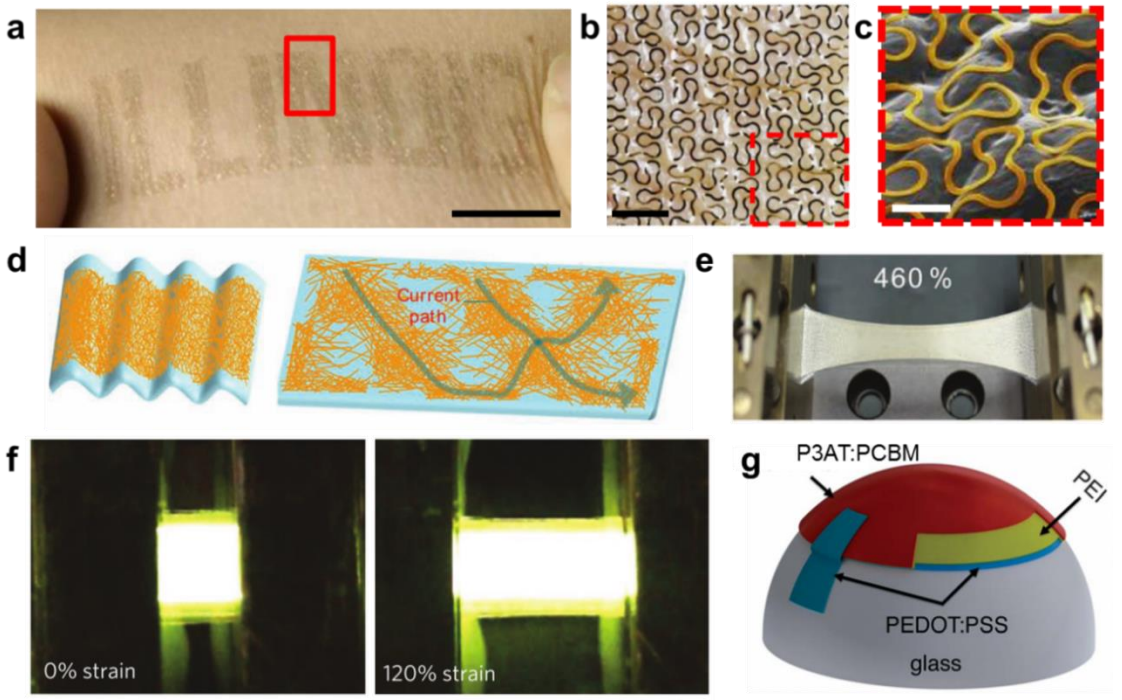

Figure 2: Images of representative samples of strategies for engineering stretchable electronics: deterministic patterning of waves and fractals (a–c), percolation of random networks and composites (d, e), and use of intrinsically stretchable elastomer (f, g). (a) Photograph of metallic wires in a fractal pattern adhered to skin (scale bar, 1 cm). A blow-up within the region indicated by the red box is shown in (b) the optical micrograph (scale bar, 1 mm); and in (c) the scanning electron micrograph (scale bar, 500 μm). (d) Schematic behavior of the very long Ag NW percolation network (VAgNPN) electrode and an Ecoflex substrate during stretching; (e) photograph of the surface morphology of an electrode on a pre-strained Ecoflex during a 460% stretching process. (f) Intrinsically stretchable light-emitting devices, employing SuperYellow, a polyphenylenevinylene derivatives. (g) Schematic diagram of hemispherical solar cells using intrinsically stretchable blend of P3AT and PCBM as the active layer. (a–c) Reproduced with permission from Ref. [27]. Copyright 2014, Nature Publishing Group (d, e) Reproduced with permission from Ref. [33]. Copyright 2012, Wiley-VCH Verlag GmbH & Co. KGaA (f) Reproduced with permission from Ref. [37]. Copyright 2013, Nature Publishing Group (g) Reproduced with permission from Ref. [38]. Copyright 2014, Royal Society of Chemistry.

1.4 – STRETCHABLE ENERGY HARVESTING TECHNOLOGIES

1.4.1 – PIEZOELECTRIC AND TRIBOELECTRIC DEVICES

Flexible biomechanical energy harvesters are continuing to show their potential in converting the kinetics of the human body into usable power or signals for devices like

pacemakers and pressure sensors, though many of these devices are made of thin films of rigid or brittle ceramics.[8,9,39–41] By nature of the transduction mechanism—which only requires physical deformation of the device structure—piezoelectric energy harvesters can be employed as power to both wearable and implantable devices. Due to the intermittency of their energy output and the fact that most of the energy put into the devices is used up to deform the crystal or material structure, piezoelectrics rarely provide the appropriate electronic outputs to continuously operate most biomedical devices without storage.[8] However, piezoelectrics can be used to extend the lifetime of implantable devices, and highly sensitive piezoelectrics can directly transduce physical stimuli for sensors that require no external power supplies.[8] Most high performance piezoelectric materials are brittle with high tensile moduli;[42] and the devices reviewed here are the state of the art for stretchable or soft piezoelectrics.

In work by McAlpine and co-workers, brittle lead zirconate titanate (PZT, $Pb[Zr_{0.52}TI_{0.48}]O_3$) nanoribbons were deterministically patterned into wave-like structures, allowing for flexing and stretching operating modes by transferring the mechanical strain to the amplitudes and wavelength of the buckled structures (**Figure 3a – 3c**).[42] The buckled PZT nanoribbons exhibited nearly a two order-of-magnitude increase in maximum tensile strain without failure over the non-buckled counterparts, 8% vs. 0.1%, by transferring the elongation to a reduction in the amplitude of the waves. Moreover, the structures also exhibited an enhanced electromechanical performance attributed to a flexoelectric contribution to the piezoelectric coefficient, leading to the peak power density of 2.5 W cm^{-3} under uniaxial deformation.[42]

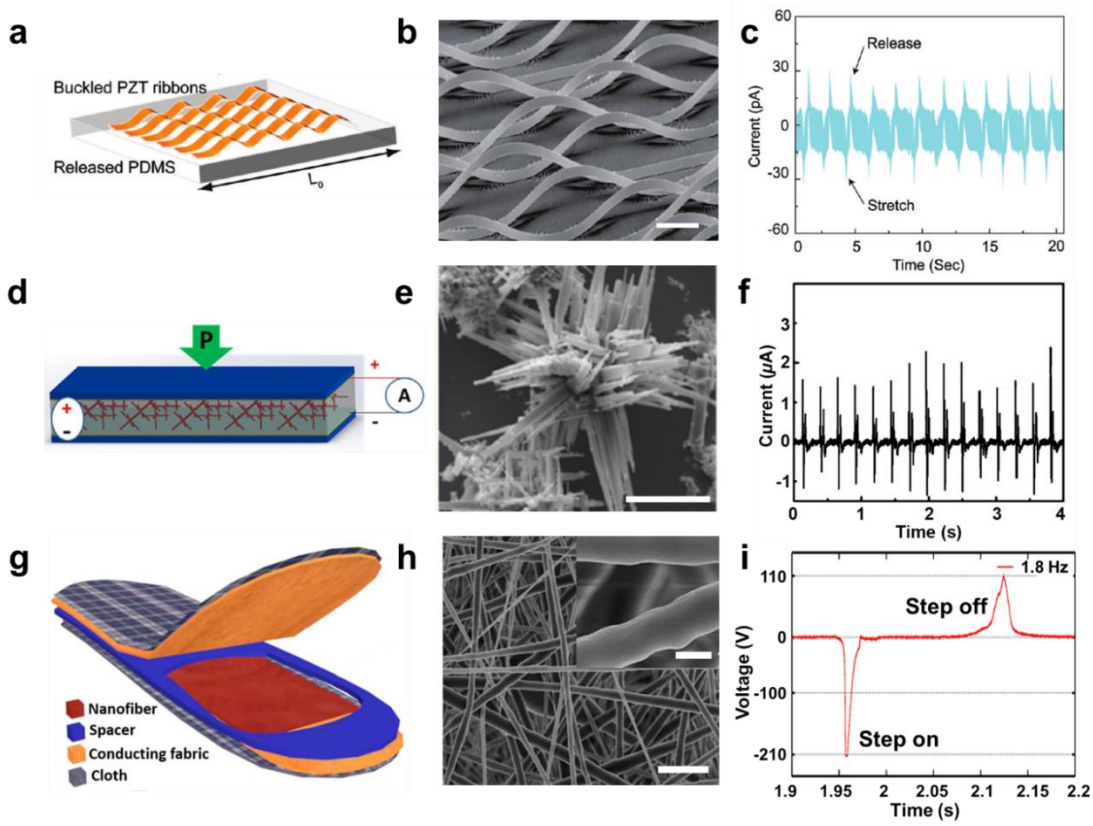

Figure 3: Representative examples of piezoelectric and triboelectric devices that are possible for bio-integration. (a) Schematic of lead zirconate titanate (PZT) nanoribbons and (b) scanning electron micrograph of the PZT ribbons transfer-printed to prestrained elastomeric substrate that produced the buckling morphology (scale bar, 20 μm). (c) Short-circuit current measured from devices comprising 5 PZT ribbons under periodic stretching of 8% strain. (d) Schematic of PMN-PT nanowire-based nanocomposite comprising PMN-PT nanowires embedded in elastomeric substrate, PDMS, and polyimide/gold electrodes. (e) High-magnification scanning electron micrograph of dispersed PMN-PT nanowires (scale bar, 5 μm). (f) Signal generation from PMN-PT nanocomposite showing the current generation under a periodic mechanical tapping. (g) Schematic diagram of the wearable all-fiber triboelectric nanogenerator (TENG)-based insole composed of electrospun piezoelectric polyvinylidene fluoride (PVDF) nanofibers. (h) Scanning electron micrograph PVDF nanofibers (scale bar, 10 μm; inset scale bar, 500 nm). (i) Voltage-time curve corresponding to the mechanical stimuli. (a–c) Reproduced with permission from Ref.[42]. Copyright 2011, American Chemical Society. (d–f) Reproduced with permission from Ref.[43]. Copyright 2013, American Chemical Society. (g–i) Reproduced with permission from Ref.[44]. Copyright 2015, Elsevier Ltd.

Examples of high performance devices exhibiting biaxial stretchability typically comprise functional nanocomposites in elastomeric substrates. Yao and coworkers demonstrated lead magnesium niobate-lead titanate (PMN-PT) nanoclusters (**Figure 3d –**

3f) embedded in elastomeric substrates that generated voltages ranging from 4.2 to 7.8 V in an open circuit and currents ranging from 1.58 to 2.29 μA, yielding maximum instantaneous power outputs of roughly 36 μW cm^{-2}.[43] The lowest strain in these devices that produced a piezoelectric response was approximately 0.01%, making them promising for applications in self-powered pressure sensors. Similarly, Huang et al. developed wearable triboelectric nanogenerators capable of harnessing highly available energy from walking (**Figure 3g – 3i**).[44] The all-fiber PVDF insoles were fabricated by electrospinning, which produced fibrils with nanostructured features that improved triboelectric performance. At a step frequency of 1.8 Hz (or typical walking speed of ~4 km h^{-1} with an average stride length), the devices produced a maximum output voltage, instantaneous power, and output current of 210 V, 2.1 mW, and 45 μA respectively.[44] The active materials take the form of nanowoven fabrics that can be integrated into mechanoelectric textiles, including shirts, pants, and insoles.[44,45] These devices can be potentially used to charge batteries or for neural stimulators.[8]

1.4.2 – THERMOELECTRIC DEVICES

Thermoelectric power generators (TEGs) can provide continuous power to wearable or subdermal biomedical devices and sensors. Unlike piezoelectric and triboelectric devices, TEGs offer a means of continuous, stable power, however they are limited by the small temperature gradients afforded by the limitations of human tolerance (between 2-5 K) and loss of latent heat though evaporation of sweat.[13] Notwithstanding these limitations, a light-weight, flexible TEG module was recently reported by Cho and coworkers.[46,47] The device comprised a screen printed inorganic porous thick film of n-

type bismuth telluride (Bi_2Te_3) and p-type antimony telluride (Sb_2Te_3), infiltrated with poly(3,4-ethylenedioxythiophene):poly(styrenesulfonate) (PEDOT:PSS) to increase the electrical conductivity and provide mechanical flexibility. The addition of PEDOT:PSS in the composite TEGs exhibited a 10% increase in the dimensionless figure-of-merit (ZT) over their screen printed, purely inorganic counterparts, and maintained high conductivity when devices were bent to 3 cm radii of curvature **(Figure 4a – 4b)**. At a temperature difference of 10 K, with the cold side held at 283 K, devices generated an output voltage of 19.1 mV and an output power density of 60 μW cm^{-2}.[46] To demonstrate the mechanical endurance and potential for wearable energy applications, a TEG consisting of seven thermoelectric couples was subjected to cyclic mechanical bending (radius of curvature of 4 cm) of over 1,000 cycles. **Figure 4c** shows fatigue strength of the device, which only exhibits minimal increase in resistance.

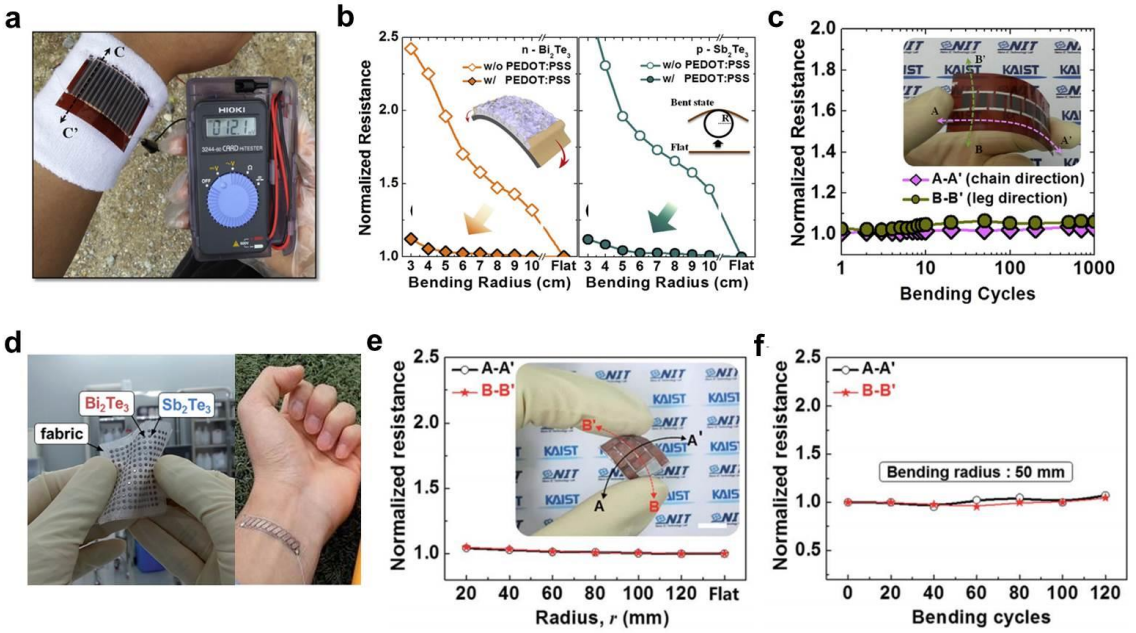

Figure 4: Wearable thermoelectric devices. (a–c) Hybrid inorganic-organic composite thermoelectric modules. (a) Device in operation on the human body. (b) Normalized resistance changes before (open points) and after (closed points) PEDOT:PSS infiltration as a function of bending radius for Bi_2Te_3 (left) and Sb_2Te_3 (right). (c) Resistance changes of the module as a function of the number of bending cycles with a bending radius of 40 mm. (d–f) Wearable thermoelectric generator fabricated on a glass fabric. (d) Image of 196 Bi_2Te_3 and Sb_2Te_3 dots on glass fabric of 40 mm x 40 mm (left) and a complete device mounted on human skin (right). (e) Resistance stability of the device under bending stress along two bending axes as a function of bending radius. (f) Stability of 120 bending cycles at bending radius of 50 mm. (a–c) Reproduced with permission from Ref.[46]. Copyright 2014, Elsevier Ltd. (d–f) Reproduced with permission from Ref.[47]. Copyright 2014, Royal Society of Chemistry.

In another study by the same group, Kim et al. improved the mechanical compliance of the TEGs by screen printing dots of Bi_2Te_3 and Sb_2Te_3 onto a woven glass fabric and subsequently sealed inside a PDMS encapsulant (**Figure 4d**).[47] The glass fabric, which served as a mechanically compliant substrate, also increased power generation by interrupting phonon propagation, thus reducing the thermal conductivity of the printed TE films. To demonstrate the use of this technology as a power source for

wearable biomedical devices, a device comprising eleven thermocouples in the shape of a bandage was bonded to the surface of the skin. The device created an output power of 3 μW, with an open circuit voltage of 2.9 mV, on a matched external load with an air temperature of 15 °C.[47] A similar prototype consisting of eight couples was subjected to mechanical testing, whereby the device showed no significant change (less than 5%) in the internal resistance with the allowed bending radius of 20 mm; furthermore, devices showed less than 7% decrease in internal resistance when repeatedly bent up to 120 cycles with a radius of curvature of 50 mm (**Figure 4e – 4f**).[47] The reported power density is sufficient to activate sub-microwatt or microwatt wearable devices such as a temperature sensor or a CMOS image sensor.[47]

1.4.3 – PHOTOVOLTAIC DEVICES

Unlike the two previous sections in which the energy outputs are limited by scavenging physical and thermal energy sources of the human body, photovoltaic (PV) devices have the potential to produce substantially more energy than piezoelectric and thermoelectric devices. However, the main limitations of PV devices for wearable applications will most likely be (1) the availability and the intensity of the light sources and (2) the surface area required for the photoactive components. The power output of PV devices will be significantly lower under diffuse outdoor light or ambient indoor light rather than ideal sunlight, and for devices with modest efficiency, larger active areas will be required for a viable power output. Despite the challenges related to indoor power, several photovoltaic technologies can be made in ultra-flexible or stretchable form factors while still providing useful power densities.[48]

Crystalline semiconductors of which most high performing solar cells are composed are extremely brittle; however, careful engineering of the materials and creative approaches to the layout of the devices can significantly increase the deformability of whole modules. One of the first examples of stretchable solar cells was introduced by Rogers and coworkers by exploiting the "island-bridge" approach.[49] Gallium-arsenide (GaAs) solar cells (roughly ~3.6 μm thick) were transfer-printed onto prestrained elastomeric PDMS substrate with thin gold interconnects between active devices (**Figure 5a – 5b**).[49] Trenches between each active device absorbed the strains caused by bending or stretching of the devices, allowing biaxial stretching of 20% strain (over 500 cycles) without degradation in performance (**Figure 5c**).[49] These devices performed identically in the relaxed and stretched states, providing the power conversion efficiency (*PCE*) under one sun condition (100 mW cm^{-2}) of approximately 13% (13 mW cm^{-2}).[49] Another example of transforming rigid materials into stretchable devices was described by Peng and coworkers; dye-sensitized solar cells were fabricated in a spring-like architecture to accommodate 30% uniaxial strain (**Figure 5d – 5e**).[50] The solar cell consisted of two stretchable fiber electrodes (a rubber fiber wrapped with conductive multi-walled carbon nanotube sheets and a modified active titanium wire), both of which were encapsulated by a transparent polyethylene tube. The device was completed filling the by filling cavity of the tube with a liquid redox electrolyte and sealing the device.[50] A single cell of the wire-like solar harvester exhibited *PCE* of 7.13% when unstretched.[50] Multiple devices were assembled into a stretchable "photovoltaic textile" comprising five cells connected in series and parallel. This assembly performed similarly when stretched

and retained ~90% of its original efficiency when subjected to 50 cycles of 20% strain (**Figure 5f**).[50]

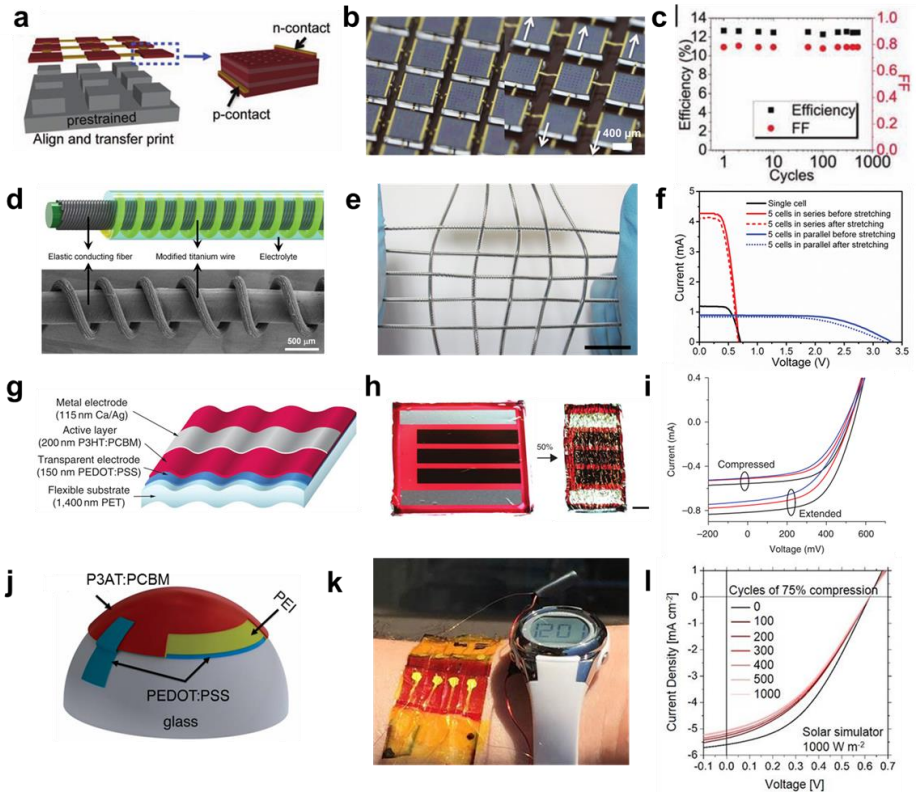

Figure 5: Stretchable photovoltaic devices. (a–c) Stretchable GaAs solar cells fabricated on "island-bridge" architecture (a) Schematic diagram. (b) Unstretched cells (left) and 20% biaxial strain (right).(c) Device performance as a function of the number of stretching cycle at 20% biaxial strain. (d–f) Stretchable and wearable dye-sensitized solar cells comprising elastic conducting fiber, modified titanium wire, and electrolyte. (d) Schematic diagram and scanning electron micrograph of the device. (e) Photograph of a stretchable photovoltaic textile after stretching (scale bar, 2 cm). (f) *J-V* curves of the photovoltaic textile in series and parallel before and after stretching. (g–i) Organic solar cells fabricated on ultrathin polyester substrates. (g) Schematic diagram. (h) Prestrained substrate of ultrathin polyester at flat (left) and 50% (right) quasi-linear compression (scale bar, 2 mm). (i) Device performance for 1 (black), 11 (red), and 22 (blue) cycles for both the fully extended and 50% compressed states. (j) Hemispherical solar cells using intrinsically stretchable blend of P3AT and PCBM as the active layer. (k) Wearable, ultra-flexible organic solar cells comprising the composite of P3HpT:PCBM powering a digital watch in natural sunlight (98 mW cm^{-2}). (l) The performance of wearable organic solar cells measured in air over 1,000 cycles of 75% compressive strain. (a–c) Reproduced with permission from Ref.[49]. Copyright 2011, Wiley-VCH Verlag GmbH & Co. KGaA. (d–f) Reproduced with permission from Ref.[50]. Copyright 2014, Wiley-VCH Verlag GmbH & Co. KGaA. (g–i) Reproduced with permission from Ref.[51]. Copyright 2012 Nature Publishing Group. (j) Reproduced with permission from Ref.[38]. Copyright 2014, Royal Society of Chemistry. (k–l) Reproduced with permission from Ref. [52].

Unlike the previous two examples, organic photovoltaics are typically much thinner (roughly ~200 nm); this thinness drastically increases the flexibility (provided a sufficiently thin substrate is used). In one of the most impressive demonstrations of ultra-flexibility of organic solar cells to date, Kaltenbrunner et al. fabricated ultra-thin organic solar cells based on a composite of poly(3-hexylthiophene) and [6,6]-phenyl C_{61} butyric acid methyl ester (P3HT:PCBM) on a 1.4 μm polyester foil (**Figure 5a**).[51] This solar cell holds the current record for specific power of organic solar cells (10 W g^{-1}) and can achieve bending radii of ~35 μm.[51] Using a similar approach to that described earlier by Lipomi et al.,[53] the authors showed that the devices can also be reversibly compressed to 50% of their original size when bonded to pre-stretched elastomeric substrates (**Figure 5b)**. Under one sun illumination (100 mW cm^{-2}), the *PCE* was measured to be around 4% (or power density of 4 mW cm^{-2}) before deformation, and around 3% (3 mW cm^{-2}) after 22 cycles of 50% compression (**Figure 5c**).[51]

Recently, our laboratory reported stretchable solar cells capable of being conformally bonded to hemispherical surfaces (**Figure 5j**).[38] The all organic, fully stretchable solar cell, comprising a composite of poly(3-octylthiophene) and PCBM (P3OT:PCBM), was prefabricated onto an elastomeric substrate, then transferred to a glass hemispherical surface through contact printing. The study was a demonstration of the significant increase in compliance of the resulting devices by increasing the molecular side chain length of semiconducting polymers.[54] Devices, fabricated from a composite of P3HT:PCBM (P3HT has six carbon atoms per side chain, $n = 6$), have superior electrical performance on a flat configuration but cracked under modest strain; while devices

comprising P3OT:PCBM (n = 8) performed worse on flat substrates but retained functionality when applied onto hemispherical substrate (conformal bonding required the solar cell to be stretched by ~24% strain).[38] Additionally, we found that poly(3-heptylthiophene) and PCBM (P3HpT:PCBM, n = 7) exhibited both high charge carrier mobilities and high compliance,[36] enabling us to fabricate an ultra-flexible, wearable organic solar cells capable of powering wearable devices.[52] This ultra-flexible device conforms to the human body and generated uninterrupted power over repeated compressive strain of 75% and a tensile strain of 5%.[52] These wearable solar cells provided up to 500 μW (power density of 1 mW cm^{-2}) when measured with natural sunlight (98 mW cm^{-2}), and ~5 μW (power density of 10 μW cm^{-2}) when measured indoors in diffuse artificial light.[52] These devices are promising for applications such as powering wearable applications (e.g., wearable biosensors) due to their relatively high power density, high specific power, and extreme mechanical durability

1.5 – SYSTEM-LEVEL POWER REQUIREMENTS

While we introduced many examples of power generation devices, it is crucial to address the viability of each option by evaluating its compatibility with different biomedical applications. We will base our discussion on the power generation capability of the power sources and the feasibility of incorporating them onto the given applications. **Figure 6** highlights the examples of several biomedical devices and the range of their typical power consumption, along with the range of energy generation for the technologies outlined previously in the chapter. Photovoltaic devices, under a full sun, could produce substantial amount of power to meet the typical power consumption of

most biomedical devices.[21] For example, given an active area of 100 cm^2 (roughly the size of standard index card), organic solar cells can potentially produce 300 mW while GaAs solar cells upward of 1.3 W. Purely from the energy production standpoint, these PV devices would be able to power hearing aids, foot drop implants,[55,56] and cochlear implants.[57] However, this energy production would be approximately two orders of magnitude lower in diffuse light and nonexistent without a light source. In addition, integration of PV devices and implantable devices will not be seamless and overcoming the users' barriers in terms of appeal, aesthetics, and comfort pose further challenges. Thermoelectric devices would be ideal to provide continuous power generation; despite the low efficiency arising from the low temperature gradient the body can endure, the power generated can be used to power small electronics and biosensors. For example, Mercier et al. fabricated an extremely low-power implantable chip that measures the endocochlear potential and transmits the measurement via a 2.4 GHz radio signal while consuming power on the order of 1 nW.[58] Tattoo-based technology, whose operating locations coincide with the largest temperature gradient on the human body, may also benefits from thermoelectric power generators. Epidermal electronics incorporate many electronic functionalities (e.g., temperature and strain sensors, transistors, light-emitting diodes, photodetectors, and radio frequency inductors)[59] and medical applications (e.g., pH sensor, sodium sensor, and ammonium sensor).[19,60] Piezoelectric and triboelectric devices provide possible sources of power for implantable devices that only consume energy intermittently. The main example is powering pacemakers by harvesting energy from the motions of the heart.[61] Improvements on current pacemakers are also aimed at reducing the power consumption by almost an order of magnitude.[12,62] Also, the large

amount of kinetic energy available in foot-falls makes triboelectric generators a viable technology for foot-drop neural stimulators, where energy generation and signal transduction could be performed simultaneously.

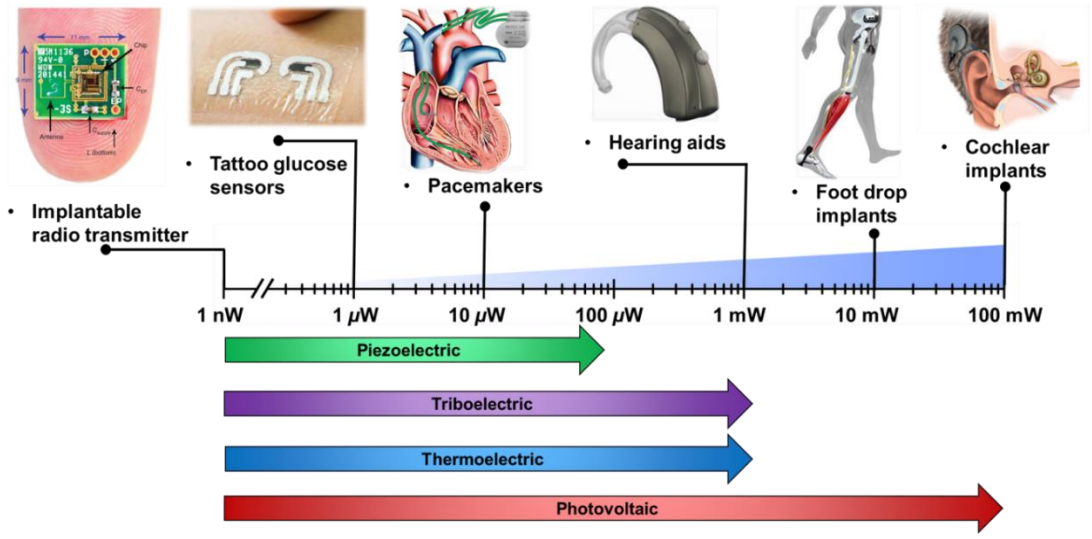

Figure 6: Order of magnitude of typical power consumption of biomedical devices and the range of power generation by the four technologies outlined in this chapter. Images reproduced with permission from Ref. [58], copyright 2012, Nature Publishing Group. Images adapted from Ref. [21,56,57,60]

1.6 – CONCLUSIONS AND CHALLENGES

Ultra-flexible and stretchable power sources will be essential components of future biointegrated medical devices. We have described several methods of energy harvesting that are compatible with biointegration; making devices compatible with soft, biological structures is tantamount to rendering them extraordinarily mechanically compliant. Before seamless integration between biomedical devices and power generators can be realized, more collaborative and multidisciplinary studies between the two fields of biology and electronics will be required. Understanding the transitional steps to bridge the two sides of science and engineering will most likely produce fruitful discovery and

unexpected problems that could potentially bring us closer to fully functional and self-powered biomedical devices.

Chapter 1, in full, is a reprint of the material as it appears in "Soft Power: Stretchable and Ultra-Flexible Energy Sources for Wearable and Implantable Devices," Timothy F. O'Connor, Suchol Savagatrup, and Darren J. Lipomi. Stretchable Bioelectronics for Medical Devices and Systems, 2016. The dissertation author was the primary investigator and author of this paper.

1.7 – REFERENCES

[1] Kim, D.-H.; Rogers, J. A. Adv. Mater. 2008, 20, 4887.

[2] Rogers, J. A.; Someya, T.; Huang, Y. Science. 2010, 327, 1603.

[3] Kim, D.-H.; Song, J.; Choi, W. M.; Kim, H.-S.; Kim, R.-H.; Liu, Z.; Huang, Y. Y.; Hwang, K.-C.; Zhang, Y.; Rogers, J. a. Proc. Natl. Acad. Sci. U. S. A. 2008, 105, 18675.

[4] Kaltenbrunner, M.; Sekitani, T.; Reeder, J.; Yokota, T.; Kuribara, K.; Tokuhara, T.; Drack, M.; Schwödiauer, R.; Graz, I.; Bauer-Gogonea, S.; Bauer, S.; Someya, T. Nature 2013, 499, 458.

[5] Ghezzi, D.; Antognazza, M. R.; Maccarone, R.; Bellani, S.; Lanzarini, E.; Martino, N.; Mete, M.; Perile, G.; Bisti, S.; Lanzani, G.; Benfenati, F. Nat. Photon. 2013, 7, 400.

[6] Xu, L.; Gutbrod, S. R.; Bonifas, A. P.; Su, Y.; Sulkin, M. S.; Lu, N.; Chung, H.-J.; Jang, K.-I.; Liu, Z.; Ying, M.; Lu, C.; Webb, R. C.; Kim, J.-S.; Laughner, J. I.; Cheng, H.; Liu, Y.; Ameen, A.; Jeong, J.-W.; Kim, G.-T.; Huang, Y.; Efimov, I. R.; Rogers, J. a. Nat. Commun. 2014, 5, 3329.

[7] O'Connor, T. F.; Rajan, K. M.; Printz, A. D.; Lipomi, D. J. J. Mater. Chem. B 2015, 3, 4947.

[8] Sue, C. Y.; Tsai, N. C. Appl. Energy 2012, 93, 390.

[9] Yun, J.; Patel, S. N.; Reynolds, M. S.; Abowd, G. D. IEEE Trans. Mob. Comput. 2011, 10, 669–683.

[10] Starner, T. IBM Syst. J. 1996, 35, 618.

[11] Li, Z.; Zhu, G.; Yang, R.; Wang, A. C.; Wang, Z. L. Adv. Mater. 2010, 22, 2534.

[12] Deterre, M.; Lefeuvre, E.; Zhu, Y.; Woytasik, M.; Boutaud, B.; Molin, R. D. J. Microelectromechanical Syst. 2014, 23, 651.

[13] Riemer, R.; Shapiro, A. J. Neuroeng. Rehabil. 2011, 8, 22.

[14] Rome, L. C.; Flynn, L.; Goldman, E. M.; Yoo, T. D. Science 2005, 309, 1725.

[15] Sun, C.; Shi, J.; Bayerl, D. J.; Wang, X. Energy Environ. Sci. 2011, 4, 4508.

[16] Yang, R.; Qin, Y.; Li, C.; Zhu, G.; Wang, Z. L. Nano Lett. 2009, 9, 1201.

[17] Coman, V.; Ludwig, R.; Harreither, W.; Haltrich, D.; Gorton, L.; Ruzgas, T.; Shleev, S. Fuel Cells 2010, 10, 9.

[18] Pan, C.; Fang, Y.; Wu, H.; Ahmad, M.; Luo, Z.; Li, Q.; Xie, J.; Yan, X.; Wu, L.; Wang, Z. L.; Zhu, J. Adv. Mater. 2010, 22, 5388.

[19] Bandodkar, A. J.; Jia, W.; Wang, J. Electroanalysis 2015, 27, 562.

[20] Katz, E. In Implantable Bioelectronics; Katz, E., Ed.; Wiley-VCH Verlag GmbH & Co. KGaA, 2014; p. 363.

[21] Deterre, M. Toward an energy harvester for leadless pacemakers, University of Paris-Sud, 2013.

[22] Kaltenbrunner, M.; Kettlgruber, G.; Siket, C.; Schwödiauer, R.; Bauer, S. Adv. Mater. 2010, 22, 2065.

[23] Xu, S.; Zhang, Y.; Cho, J.; Lee, J.; Huang, X.; Jia, L.; Fan, J. a; Su, Y.; Su, J.; Zhang, H.; Cheng, H.; Lu, B.; Yu, C.; Chuang, C.; Kim, T.-I.; Song, T.; Shigeta, K.; Kang, S.; Dagdeviren, C.; Petrov, I.; Braun, P. V; Huang, Y.; Paik, U.; Rogers, J. a. Nat. Commun. 2013, 4, 1543.

[24] Hu, L.; Wu, H.; La Mantia, F.; Yang, Y.; Cui, Y. ACS Nano 2010, 4, 5843–5848.

[25] Savagatrup, S.; Printz, A. D.; O'Connor, T. F.; Zaretski, A. V.; Lipomi, D. J. Chem. Mater. 2014, 26, 3028.

[26] Lacour, S. P.; Jones, J.; Wagner, S. Proc. IEEE 2005, 93, 1459.

[27] Fan, J. a; Yeo, W.-H.; Su, Y.; Hattori, Y.; Lee, W.; Jung, S.-Y.; Zhang, Y.; Liu, Z.; Cheng, H.; Falgout, L.; Bajema, M.; Coleman, T.; Gregoire, D.; Larsen, R. J.; Huang, Y.; Rogers, J. a. Nat. Commun. 2014, 5, 3266.

[28] Khang, D.-Y.; Rogers, J. a.; Lee, H. H. Adv. Funct. Mater. 2009, 19, 1526.

[29] Yu, Z.; Niu, X.; Liu, Z.; Pei, Q. Adv. Mater. 2011, 23, 3989.

[30] Liang, J.; Li, L.; Tong, K.; Ren, Z.; Hu, W.; Niu, X.; Chen, Y.; Pei, Q. ACS Nano 2014, 8, 1590.

[31] Lipomi, D. J.; Vosgueritchian, M.; Tee, B. C.-K.; Hellstrom, S. L.; Lee, J. a; Fox, C. H.; Bao, Z. Nat. Nanotech. 2011, 6, 788.

[32] Lacour, S. P.; Chan, D.; Wagner, S.; Li, T.; Suo, Z. Appl. Phys. Lett. 2006, 88, 204103.

[33] Lee, P.; Lee, J.; Lee, H.; Yeo, J.; Hong, S.; Nam, K. H.; Lee, D.; Lee, S. S.; Ko, S.

H. Adv. Mater. 2012, 24, 3326.

[34] Kettlgruber, G.; Kaltenbrunner, M.; Siket, C. M.; Moser, R.; Graz, I. M.; Schwödiauer, R.; Bauer, S. J. Mater. Chem. A 2013, 1, 5505.

[35] Krebs, F. C.; Espinosa, N.; Hösel, M.; Søndergaard, R. R.; Jørgensen, M. Adv. Mater. 2014, 26, 29.

[36] Savagatrup, S.; Printz, A. D.; Wu, H.; Rajan, K. M.; Sawyer, E. J.; Zaretski, A. V.; Bettinger, C. J.; Lipomi, D. J. Synth. Met. 2015, 203, 208.

[37] Liang, J.; Li, L.; Niu, X.; Yu, Z.; Pei, Q. Nat. Photonics 2013, 7, 817.

[38] O'Connor, T. F.; Zaretski, A. V.; Shiravi, B. A.; Savagatrup, S.; Printz, A. D.; Diaz, M. I.; Lipomi, D. J. Energy Environ. Sci. 2014, 7, 370.

[39] Hwang, G. T.; Park, H.; Lee, J. H.; Oh, S.; Park, K. Il; Byun, M.; Park, H.; Ahn, G.; Jeong, C. K.; No, K.; Kwon, H.; Lee, S. G.; Joung, B.; Lee, K. J. Adv. Mater. 2014, 26, 4880.

[40] Qi, Y.; McAlpine, M. C. Energy Environ. Sci. 2010, 3, 1275.

[41] Lee, M.; Chen, C. Y.; Wang, S.; Cha, S. N.; Park, Y. J.; Kim, J. M.; Chou, L. J.; Wang, Z. L. Adv. Mater. 2012, 24, 1759.

[42] Qi, Y.; Kim, J.; Nguyen, T. D.; Lisko, B.; Purohit, P. K.; McAlpine, M. C. Nano Lett. 2011, 11, 1331.

[43] Xu, S.; Yeh, Y. W.; Poirier, G.; McAlpine, M. C.; Register, R. A.; Yao, N. Nano Lett. 2013, 13, 2393.

[44] Huang, T.; Wang, C.; Yu, H.; Wang, H.; Zhang, Q.; Zhu, M. Nano Energy 2015, 14, 226.

[45] Jeong, C. K.; Lee, J.; Han, S.; Ryu, J.; Hwang, G.-T.; Park, D. Y.; Park, J. H.; Lee, S. S.; Byun, M.; Ko, S. H.; Lee, K. J. Adv. Mater. 2015, 27, 2866.

[46] We, J. H.; Kim, S. J.; Cho, B. J. Energy 2014, 73, 506.

[47] Kim, S. J.; We, J. H.; Cho, B. J. Energy Environ. Sci. 2014, 7, 1959.

[48] Lipomi, D. J.; Bao, Z. Energy Environ. Sci. 2011, 4, 3314.

[49] Lee, J.; Wu, J.; Shi, M.; Yoon, J.; Park, S. Il; Li, M.; Liu, Z.; Huang, Y.; Rogers, J. A. Adv. Mater. 2011, 23, 986.

[50] Yang, Z.; Deng, J.; Sun, X.; Li, H.; Peng, H. Adv. Mater. 2014, 26, 2643.

[51] Kaltenbrunner, M.; White, M. S.; Głowacki, E. D.; Sekitani, T.; Someya, T.; Sariciftci, N. S.; Bauer, S. Nat. Commun. 2012, 3, 770.

[52] O'Connor, T. F.; Zaretski, A. V.; Savagatrup, S.; Printz, A. D.; Wilkes, C. D.; Diaz, M. I.; Sawyer, E. J.; Lipomi, D. J. submitted.

[53] Lipomi, D. J.; Tee, B. C.-K.; Vosgueritchian, M.; Bao, Z. Adv. Mater. 2011, 23, 1771.

[54] Savagatrup, S.; Makaram, A. S.; Burke, D. J.; Lipomi, D. J. Adv. Funct. Mater. 2014, 24, 1169.

[55] Haugland, M.; Childs, C.; Ladouceur, M.; Haase, J.; Sinkjaer, T. In Proc. 5th Ann. IFESS Conf.; 2000; p. 59.

[56] Lyons, G. M.; Sinkjær, T.; Burridge, J. H.; Wilcox, D. J. IEEE Trans. Neural Syst. Rehabil. Eng. 2002, 10, 260.

[57] Baker, M. W. A Low-Power Cochlear Implant System, Massachusetts Institute of Technology, 2007.

[58] Mercier, P. P.; Lysaght, A. C.; Bandyopadhyay, S.; Chandrakasan, A. P.; Stankovic, K. M. Nat. Biotechnol. 2012, 30, 1240.

[59] Kim, D.-H.; Lu, N.; Ma, R.; Kim, Y.-S.; Kim, R.-H.; Wang, S.; Wu, J.; Won, S. M.; Tao, H.; Islam, A.; Yu, K. J.; Kim, T.; Chowdhurry, R.; Ying, M.; Xu, L.; Li, M.; Chung, H.-J.; Keum, H.; McCormick, M.; Liu, P.; Zhang, Y.-W.; Omenetto, F. G.; Huang, Y.; Coleman, T.; Rogers, J. A. Science 2011, 333, 838.

[60] Bandodkar, A. J.; Jia, W.; Yard, C.; Wang, X.; Ramirez, J.; Wang, J. Anal. Chem. 2015, 87, 394.

[61] Dagdeviren, C.; Yang, B. D.; Su, Y.; Tran, P. L.; Joe, P.; Anderson, E.; Xia, J.; Doraiswamy, V.; Dehdashti, B.; Feng, X.; Lu, B.; Poston, R.; Khalpey, Z.; Ghaffari, R.; Huang, Y.; Slepian, M. J.; Rogers, J. a. Proc. Natl. Acad. Sci. U. S. A. 2014, 111, 1927.

[62] Deterre, M.; Boutaud, B.; Dalmolin, R.; Boisseau, S.; Chaillout, J.-J.; Lefeuvre, E.; Dufour-Gergam, E. In Design, Test, Integration and Packaging of MEMS/MOEMS [DTIP], 2011 Symposium on; 2011; p. 387.

CHAPTER 2 – STRETCHING AND CONFORMAL BONDING OF ORGANIC SOLAR CELLS TO HEMISPHERICAL SURFACES

Timothy F. O'Connor, Aliaksandr V. Zaretski, Bijan A. Shiravi, Suchol Savagatrup, Adam D. Printz, Mare Ivana Diaz, and Darren J. Lipomi*

Department of NanoEngineering, University of California, San Diego
9500 Gilman Drive, Mail Code 0448, La Jolla, CA 92093-0448

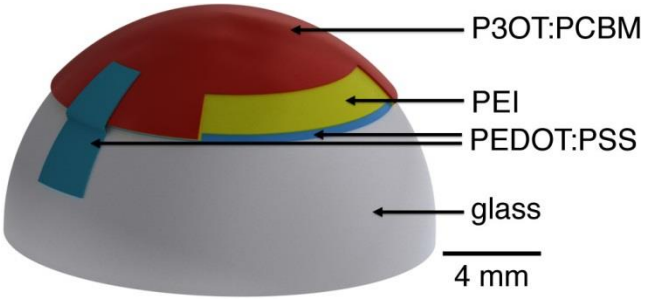

Figure 7: Graphical abstract depicting schematic of the stretchable hemispherical solar cell.

2.1 – BROADER CONTEXT

One of the prominent selling points of organic electronic materials and devices is the potential that they could be elastically and plastically deformed without fracture. In the context of organic solar cells, this mechanical compliance would facilitate roll-to-roll fabrication, robustness to the stresses encountered in the outdoor environment and in portable applications, integration with the moving parts of machines or the body, and bonding to non-planar surfaces such as vehicles and buildings. Organic semiconductors, however, are almost never optimized on the basis of mechanical properties, and most crack at modest strains. This paper demonstrates (1) the stretching and conformal bonding of whole organic solar cells to hemispherical surfaces and (2) the surprising

influence of the length of the alkyl solubilizing group on the plasticity of the semiconducting layer. This result suggests that seemingly minor differences in the structure of an organic semiconductor can have drastic consequences on the suitability of a particular material for applications demanding tensile deformation.

2.2 – ABSTRACT

This communication describes the stretching and conformal bonding (*i.e.*, decal-transfer printing) of organic solar cells in both the "conventional" and "inverted" configurations to hemispherical glass surfaces with radii of 8 mm. This action produces equivalent biaxial tensile strains of 24%, which many materials used in organic electronic devices cannot accommodate without fracture. Consideration of the mechanical properties of conjugated polymers reveals a surprising effect of a single structural parameter—the length of the alkyl side chain—on the elasticity and ductility of regioregular polythiophene. This analysis enables selection of materials that can accommodate sufficient tensile strain for non-planar applications. For polymer-fullerene solar cells, devices based on the elastic and ductile poly(3-octylthiophene) (P3OT) exhibit typical photovoltaic properties when bonded to hemispherical glass substrates, while those based on the relatively brittle poly(3-hexylthiophene) (P3HT) exhibit extensive cracking, which degrades the photovoltaic effect significantly. The results suggest that mechanical properties should be taken into account when designing and selecting organic semiconductors for applications that demand significant deformation.

2.3 – INTRODUCTION

Organic electronic devices—e.g., solar cells, transistors, and displays based on π-conjugated polymers and small molecules—are treated as potentially low-cost and mechanically compliant alternatives to their inorganic counterparts.[1, 2] The high flexibility of organic electronic devices, however, is largely a function of the thinness of the active materials and substrates; it is not necessarily a function of the intrinsic mechanical compliance of organic semiconductors. In fact, the peak strains imposed on the active materials while bent are rarely greater than 2%—a modest level of deformation that nonetheless fractures some of the most well-known organic semiconductors[3] and polymer-small molecule composites.[4, 5] This paper demonstrates two major effects: (1) the ability to stretch and bond an especially ductile organic electronic device to hemispherical surfaces and (2) the unexpectedly large effect of a single structural parameter—the length of the alkyl side chain—on the compliance and ductility of thin films comprising poly(3-alkylthiophenes) (P3ATs) and P3AT:fullerene composites. We demonstrate that an analysis of the mechanical properties of organic semiconductors is necessary to select materials for applications that will require appreciable (>2%) strains. Such applications include those that demand resistance to mechanical failure (for portability)[6, 7] and integration with moving parts,[8] textiles,[9] and curved surfaces other than cylinders.[10] We use the results of our investigation to show that the most popular active layer for organic photovoltaics, poly(3-hexylthiophene) (P3HT) mixed with [6,6]-phenyl C_{61} butyric acid methyl ester (PCBM), cannot be stretched to conform to a hemispherical surface without cracking, but that a substitution of materials informed by our analysis enables sufficient deformation and transfer (**Figure 8**). We believe that the

mechanical properties of an organic semiconductor should be given a high priority when selecting materials for a given application. Our observations may suggest the design of new materials that combine state-of-the-art electronic properties with favorable mechanical ones.

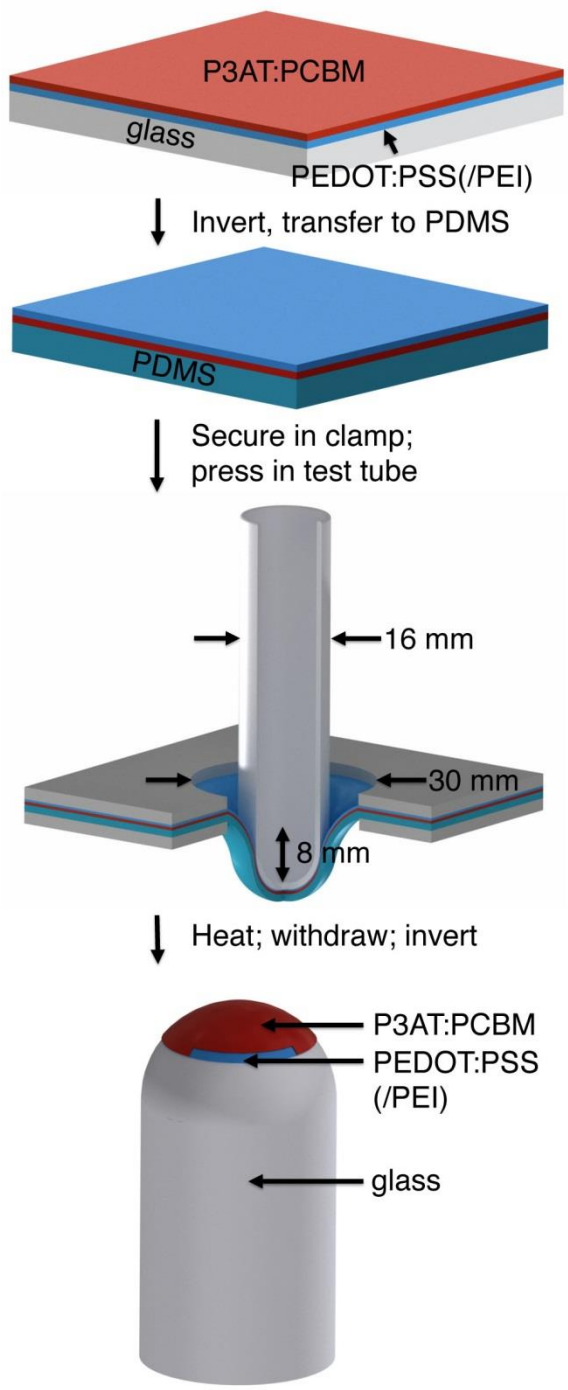

Figure 8: Summary of the process used to transfer multilayer films of conjugated polymers to a hemispherical glass substrate. Passivated glass is spin-coated with poly(3,4-ethylenedioxythiophene):poly(styrene sulfonate) (PEDOT:PSS) and P3AT:PCBM. The multilayer film is transferred to a poly(dimethylsiloxane) (PDMS) slab and secured in a clamp bearing a circular aperture. A test tube is pressed into the suspended PDMS/P3AT:PCBM/PEDOT:PSS substrate, heated, and withdrawn. Slow withdrawal separates the conjugated polymer films and leaves it attached to the hemispherical surface of the test tube.

The field of stretchable electronics encompasses and extends the field of flexible electronics.[11-14] The use of buckled,[15] wavy,[16] or serpentine microstructures,[17] stretchable interconnects,[18] controlled fracture,[19] or dispersion of conductive particles in a deformable insulator[20, 21] are all methods used to fabricate devices that are, on the whole, stretchable. The outcome of most of these strategies is that the active material is not subjected to significant strain.[22] Designing materials—semiconductors in particular—that retain their electronic properties when deformed represents a significant scientific challenge.[23, 24] There are, however, very few examples in the literature where whole organic electronic devices have accommodated significant tensile deformation with little loss in function. Pei and coworkers, for example, demonstrated a plastically deformable light-emitting device comprising a blue emitter based on a polyfluorene backbone. When this emissive layer was sandwiched between electrodes comprising carbon nanotubes, the whole device could be heated and deformed plastically by ≥45% with its ability to emit light intact.[24] Another successful example is that of Müller et al., who demonstrated that a diblock copolymer comprising P3HT and polyethylene segments with weight fractions up to 90% maintains significant charge mobility when stretched by 600%,[23] but there are many applications (*e.g.*, solar cells), for which it will not be desirable to have a large insulating component in the active layer. Most pure films of organic semiconductors and devices comprising multiple layers are significantly less compliant than the two examples cited above.

Measurements of the mechanical properties of conjugated polymers have revealed that not all of these materials can be treated as equally deformable. For example, Tahk et

al. measured the tensile modulus of polyaniline to be 30 MPa (though likely plasticized by residual solvent), and that of the molecular semiconductor pentacene to be ~15 GPa.[3] These authors and others[5] have shown that a 1:1 mixture of poly(3-hexylthiophene) (P3HT) and [6,6]-phenyl C_{61} butyric acid methyl ester (PCBM) had a tensile modulus five times greater that than of the pure polymer.[3] O'Connor et al. have observed an apparent trade-off between electronic performance and mechanical compliance.[25] These investigators observed that increasing the crystallinity of pure films of PBTTT by thermal annealing[4] and of P3HT:PCBM blends by the speed of solvent evaporation[25] increases the charge-carrier mobility and photovoltaic efficiency while rendering the films substantially more brittle (the best-performing PBTTT and P3HT:PCBM films fractured at strains <2.5%).[4, 25] The pioneering work of Smith and Heeger studied the mechanical properties of early conjugated polymers such as polyacetylene,[26] poly(2,5-thienylene vinylene),[27] and regiorandom polythiophene.[28] The demands of applications such as organic solar cells and field-effect transistors, however, have led to a dramatic increase in the number of soluble, regioregular, low-bandgap, donor-acceptor, and structurally complex polymers available,[29] and these polymers are rarely optimized on the basis of mechanical properties. General guidelines that link the structural characteristics of these polymers to their mechanical properties would be useful for any device intended for portability,[30] prolonged outdoor service,[31] or biological integration.[10, 32]

While unsubstituted conjugated polymers such as poly(acetylene) can exhibit high stiffness (tensile modulus 50 GPa) and strength (ultimate tensile strength 900 MPa) when oriented,[26] unsubstituted materials are generally not processible from solution. Alkyl pendant groups impart solubility to the polymer, but also drastically change the

mechanical properties of the material.[28] These side chains reduce the number of covalently bonded units along the axis of the main chain per unit volume and also reduce the secondary interactions between the main chain.[33] Both effects tend to reduce the modulus and strength (and conductivity) of the polymer.[33] While these effects are deleterious for materials intended for use in structural applications,[33] renewed interest in stretchable semiconductors holds compliance and ductility in high regard.[4, 23, 34] In applications demanding reversible deformation or one-time bonding to non-planar substrates, the goal is not to maximize electronic performance, but to find materials exhibiting an acceptable compromise between mechanical and optoelectronic properties.

We looked to the regioregular poly(3-alkylthiophene)s (P3ATs) as a model system to investigate the influence of alkyl side chain on the intrinsic stretchability of conjugated polymers. While P3ATs are well known, their properties have not been compared in a context relevant to stretchable devices. In a series of P3ATs where A = butyl (B), hexyl (H), octyl (O), and dodecyl (DD), the compliance and ductility increased with increasing length of the alkyl chain from P3BT to P3OT, while the properties of P3OT and P3DDT were similar.[35] These measurements were corroborated by theoretical calculations—which elaborated on earlier methods described by Seitz[36] and Tahk[3]—that accounted for differences in the glass transition temperatures along with structural parameters.[35] The largest differences in mechanical properties between adjacent polymers in the series occurred between P3HT and P3OT, whose tensile moduli differed by nearly an order of magnitude: 1.09 GPa for P3HT and 0.15 GPa for P3OT.

The incorporation of fullerenes in films of conjugated polymers has several important consequences for the mechanical properties and interfacial adhesion of bulk

heterojunction films. Previous reports have shown that the tensile modulus of P3HT:PCBM (1:1) films (4.3 GPa) was nearly five times greater than that of the pure polymer (0.92 GPa).[3, 5] We have also measured the crack-onset strains of P3HT (9%) and P3HT:PCBM (3%) on PDMS substrates, and found that fullerenes increase the brittleness of the films relative to the pure polymers.[35] Other deleterious effects of PCBM on the compliance of devices include lowered cohesive energy of the bulk heterojunction (from 2.5 J m^{-2} to 0.5 J m^{-2} for P3HT:PCBM blends containing from 25% to 100% PCBM)[7] and lowered adhesion of bulk heterojunction films to the PEDOT:PSS electrode (1.6 J m^{-2} for the pure polymer and 0.1 J m^{-2} for the pure fullerene).[6] The influence of PCBM on the moduli of conjugated polymers is predictable in some circumstances by composite theory, as described by Tahk et al,[3] but the exact dependence is a strong function of the identity of the polymer[5] and processing conditions, especially the way in which the rate of solvent evaporation affects the crystallinity of the polymer.[25]

Blends of P3HT and P3OT with [6,6]-phenyl C_{61} butyric acid methyl ester (PCBM) also exhibited dramatically different propensities to fracture, which can be regarded as a measure of ductility. P3HT:PCBM cracked at an average strain of 3%, while P3OT:PCBM did not crack until 47% strain.[35] We reasoned that substitutions of materials based on an analysis of the structural parameters that influence the mechanical properties of conjugated polymers could enable applications in stretchable and conformable electronics not accessible by standard materials. Thus, we developed procedures to stretch and transfer organic solar cells based on P3HT and those based on P3OT to hemispherical substrates in order to compare the performance in this mechanically demanding geometry.

2.3 – RESULTS AND DISCUSSION

2.3.1 – DEPENDENCE OF MOLECULAR WEIGHT ON MECHANICAL COMPLIANCE OF P3ATS.

Most polymeric materials exhibit an increase in tensile modulus with molecular weight.[37] This effect, however, tends to saturate above a sufficiently high molecular weight.[37] Another trend predicts that increased polydispersity index (PDI) produces increased compliance.[37] Given that different synthetic methods and levels of purification can yield different molecular weights and polydispersities, we measured the tensile modulus of a commercial sample of P3HT (M_w = 29,000 g mol^{-1}, PDI = 2.0, as determined by gel permeation chromatography using polystyrene standards). We then synthesized a sample of P3HT in our laboratory by the Grignard Metathesis polymerization[38] and quenched the reaction after approximately 10 s to produce a sample with low molecular weight (M_w = 7,500 g mol^{-1}, PDI = 1.2). The tensile moduli of both samples were similar: 1.09 ± 0.15 GPa for the commercial sample and 1.05 ± 0.35 GPa for the low-M_w sample (synthesized in-house). The P3OT (obtained commercially) had a greater M_w, 108,000 g mol^{-1} (PDI = 2.5), but a much smaller tensile modulus (0.15 ± 0.05 GPa) than the P3HT samples. These data suggest that the M_w does not significantly affect the mechanical properties of the materials in the range of M_w of the samples studied, and that the M_w of P3OT cannot explain its significantly greater compliance compared to that of P3HT. We believe that the length of the alkyl chain was the principal

determinant of the difference in mechanical properties observed between the P3HT and P3OT.

2.3.2 – DETERMINATION OF ONSET OF PLASTIC DEFORMATION

We note that the descriptor "stretchability" can be subdivided into elasticity and plasticity. For form factors that require one-time bonding to curved substrates, tensile modulus can be used as a metric for overall compliance, but it does not predict the ductility and cracking behavior of films. We measured the approximate yield strain of P3HT and P3OT using the strain at which buckles first appeared ("buckling-onset" strain) as a proxy. In this experiment, we bonded the P3AT films to PDMS substrates and stretched the PDMS/P3AT samples using a computer-controlled linear actuator and applied cyclic strains in increments of 1%, that is 0% → 1% → 0% → 2% → 0% etc. Upon each return to 0% strain, we examined the films with a microscope and took the minimum strain at which buckles formed to be an approximation of the onset of plastic deformation. P3OT exhibited a greater range of elastic behavior before the onset of plastic deformation: the onset of buckling occurred after stretching to 11% strain for P3OT and after stretching to 4% strain for P3HT.

2.3.3 – CONFORMAL BONDING TO HEMISPHERICAL SUBSTRATES

To bond a thin film (or stack of films) conformally to a hemispherical surface requires the film to accommodate compressive or tensile deformation so that wrinkles are not generated.[39] **Figure 8** summarizes the process—based on kinetically controlled

transfer printing[40]—we used to fabricate the devices. Briefly, the devices were fabricated on passivated glass substrates, transferred to poly(dimethylsiloxane) (PDMS) membranes, mounted in a stage bearing a circular aperture, and transferred to the hemispherical terminus of a glass test tube by pushing the test tube into the PDMS membrane bearing the conjugated polymer layers. A computer-controlled linear actuator was used to impose precise displacements of the test tube. Heating and slow withdrawal of the test tube transferred the part of the film in contact with the hemispherical terminus of the tube to its surface. We used two configurations, which are summarized in **Figure 9**. In the conventional geometry, PEDOT:PSS behaved as the bottom, high-work-function electrode, on top of which the P3AT:PCBM film was deposited. Eutectic gallium-indium (EGaIn), deposited after bonding of the PEDOT:PSS/P3AT:PCBM films to the hemispherical surface, served as the low-work-function top electrode. In the inverted geometry, PEDOT:PSS treated with polyethyleneimine (PEI) behaved as the bottom, low-work-function electrode.[41] A film of untreated PEDOT:PSS, laminated to the device in a step subsequent to the procedure depicted in **Figure 8**, served as the high-work-function electrode.[42]

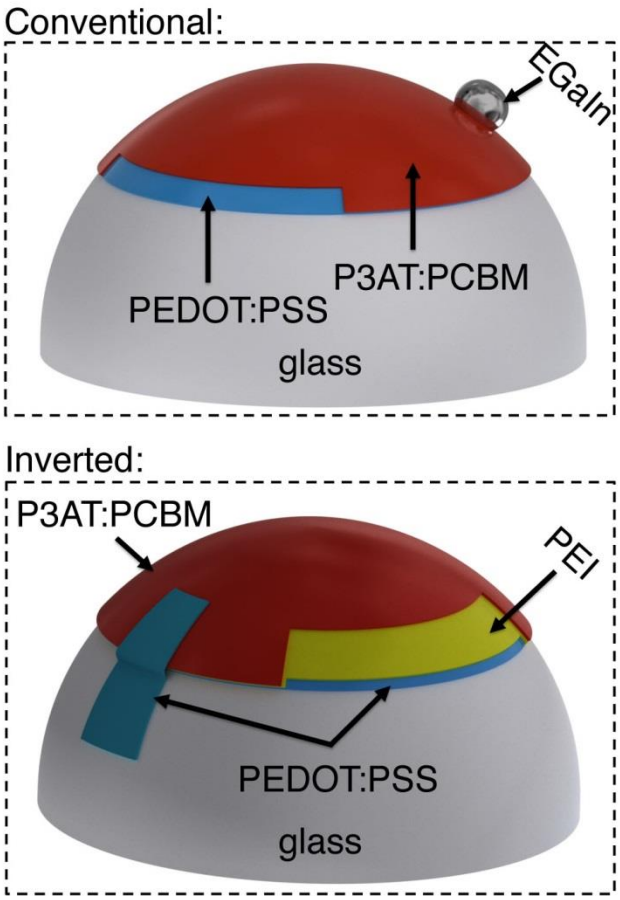

Figure 9: Conventional (top) vs. inverted (bottom) geometries of organic solar cells discussed in the text. In the conventional geometry, a droplet of eutectic gallium-indium (EGaIn) provides the low-work-function top contact (cathode). In the inverted geometry, a layer of PEDOT:PSS bearing a thinner layer of polyethyleneimine (PEI), applied to the glass substrate, behaves as the low-work-function electrode.

2.3.4 – COMPUTATIONAL ANALYSIS OF STRAIN

We selected materials for this experiment based on a computational analysis whose goal was to predict the minimum strain required to stretch a planar sheet over a hemispherical surface without generating wrinkles. **Figure 10** shows the results of our simulation. It assumes no slippage of the film against the hemispherical surface during the process of transfer from the PDMS to the hemisphere. This assumption is justified by

a visual inspection of the films during the transfer: once the film made contact with the hemispherical surface, it did not continue to crack with additional displacement of the test tube into the PDMS membrane. Moreover, when we drove the test tube into the substrate from the opposite direction (such that the conjugated polymer films were on the convex surface of the deflected PDMS membrane) we observed cracking patterns consistent with the simulation on the convex surface, as shown in **Figure 10**. That is, the density of cracks was greatest at the apex. According to our simulation of the strain on the concave surface, the maximum strain of 24% occurred at an arc-length of 4.42 mm from the apex of the hemisphere (r = 8 mm). Our analysis of the mechanical properties of P3ATs suggested that a film of P3HT:PCBM would be severely damaged as a result of the transfer, while P3OT:PCBM would survive the transfer. Our placement of the PEDOT:PSS top contact in the inverted geometry (as shown schematically in **Figure 9**) was chosen to overlap with the region of the greatest predicted deformation.

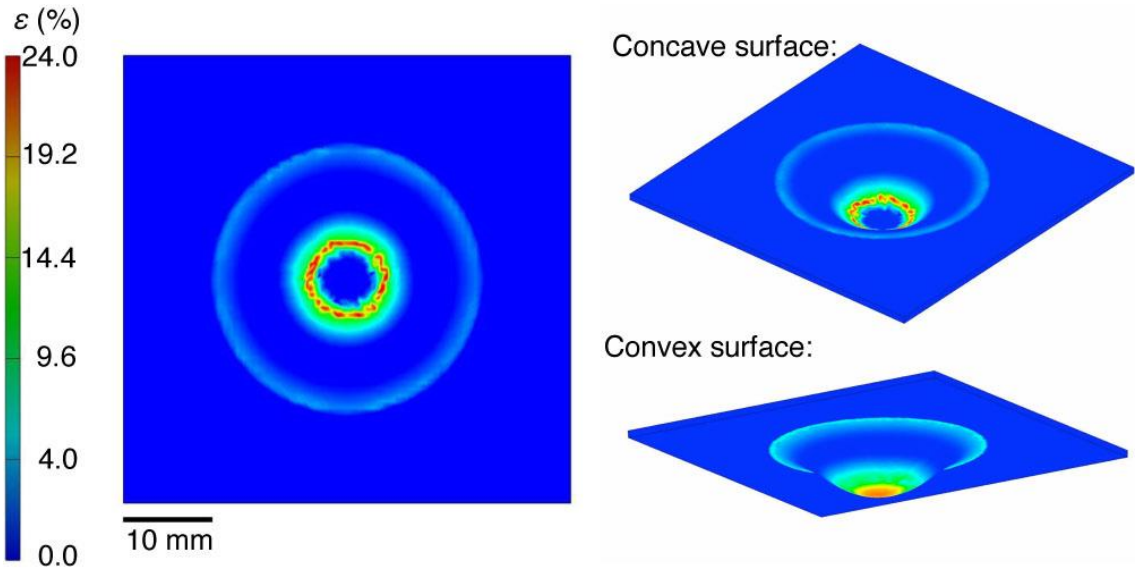

Figure 10: Computational analysis of the strain produced in the thin films when they are transferred to the hemispherical surfaces. The 2D map (left) represents the strain generated at the surface of the PDMS membrane bearing the multilayered conjugated polymer film. This is the same view shown in the 3D rendering of the concave surface (top right). The distribution of strain observable in the convex surface (bottom right), which is dissimilar from that of the concave surface, is a consequence of the finite thickness of the PDMS membrane, and that the convex surface is not pinned by contact with the glass hemisphere during the process of deformation, as is the concave surface.

2.3.5 – CRACKING BEHAVIOR

Photographs of films comprising a single layer of the two P3ATs blended with PCBM are shown in **Figures 11a** and **11b**. The P3HT:PCBM film exhibited extensive rupturing; the P3OT:PCBM film, in contrast, was undamaged. We also observed striking differences in the cracking behavior of P3AT:PCBM films on PDMS substrates when stretched with and without an intervening layer of PEDOT:PSS. We attribute the apparent increase in ductility of the P3HT:PCBM film when PEDOT:PSS was used to the behavior of PEDOT:PSS as a layer that promotes adhesion between PDMS and conjugated polymer films.[5] Improved adhesion between a thin film and a stretchable substrate increase the effective ductility of the film by distributing strain uniformly. In a

poorly adhered film, global tensile strains localize to delaminated regions and thus form cracks at much smaller strains than for systems with better adhesion.[43] This effect has been observed in stretched films of copper on polyimide substrates with and without chromium adhesion layers.[43] The presence of PEDOT:PSS significantly reduced the extent of cracking—though still enough to cause catastrophic failure of the device—in PEDOT:PSS/P3HT:PCBM films (**Figure 11c**). The bilayer film comprising PEDOT:PSS/P3OT:PCBM was undamaged (**Figure 11d**). Interestingly, while PEDOT:PSS improved the effective ductility of P3HT:PCBM in these experiments, it had a deleterious effect on the effective ductility of P3OT:PCBM. PEDOT:PSS on PDMS substrates has a crack-onset strain of ~12%[44] which is intermediate between that of P3HT:PCBM (3%)[35] and P3OT:PCBM (47%).[35] The cracking of PEDOT:PSS underneath P3OT:PCBM thus drives the formation of cracks in the top layer.

Given that the presence of residual solvent can reduce the tensile modulus and increase the ductility of conjugated polymer samples (as Tahk et al. observed for polyaniline[3]), we measured the crack-onset strain for an as-cast sample of P3HT and found it to be indistinguishable to that of a sample that was dried in vacuum (<200 mtorr) for 60 min. This experiment suggests that the length of the alkyl chain, rather than the plasticizing effects of residual solvent, is the principal determinant of the mechanical properties of the two P3ATs examined in this work.

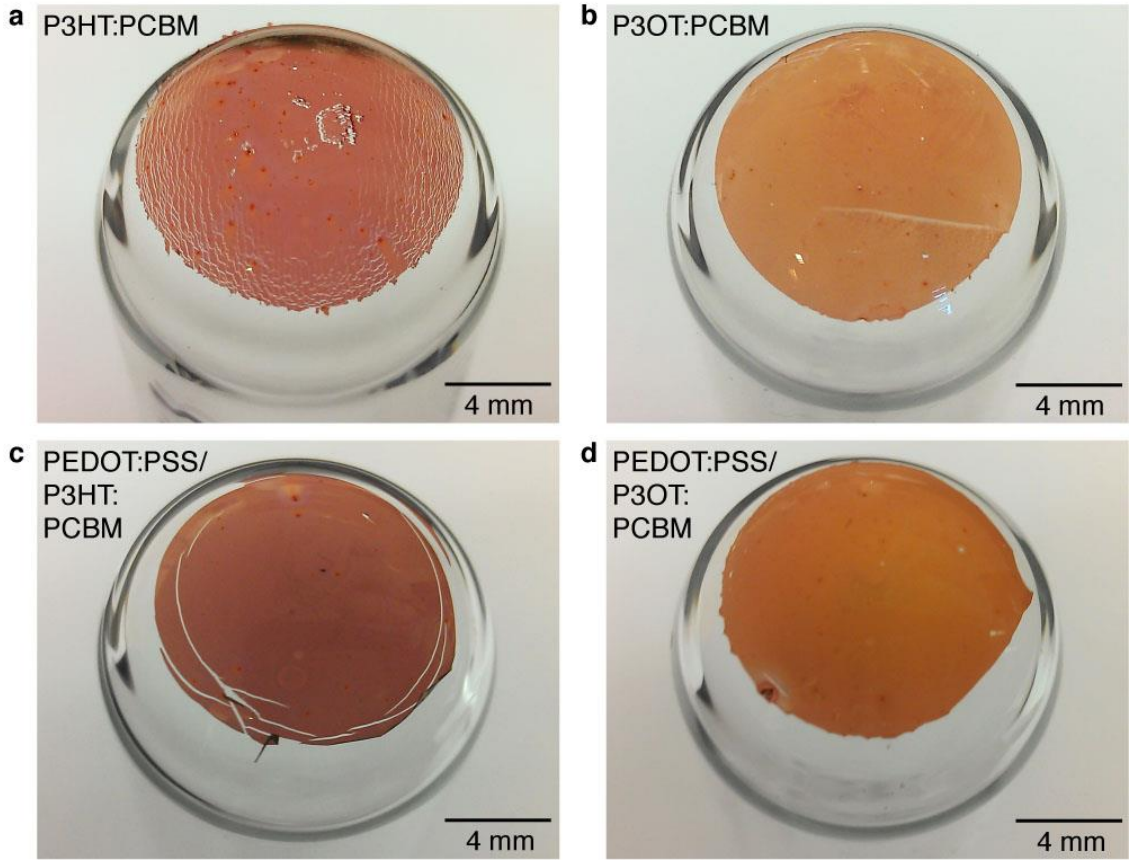

Figure 11: Photographs of conjugated polymer films stretched and bonded to hemispherical surfaces. (a) P3HT:PCBM film exhibiting extensive fracturing. (b) Intact P3OT:PCBM film. (c) Bilayer film comprising PEDOT:PSS/P3HT:PCBM exhibiting concentric cracking pattern which is not observed in the PEDOT:PSS/P3OT:PCBM film (d).

2.3.6 – MEASUREMENT OF PHOTOVOLTAIC PROPERTIES

To test the effect of the deformation on the optoelectronic behavior of the devices, we measured the photovoltaic properties using a solar simulator (**Figure 12**). **Figure 12a** demonstrates that the damage caused by cracking limits the applicability of P3HT:PCBM in devices demanding mechanical compliance. In this device, a droplet of EGaIn was positioned in the region on the film that experienced the maximum strain. The current density vs. voltage (*J*-*V*) for these devices resembled resistors in parallel with solar cells.

We attribute this behavior to areas in which the EGaIn penetrated through cracks in the active layer and made direct contact with the PEDOT:PSS. In contrast, the devices comprising undamaged P3OT:PCBM films in the conventional geometry exhibited behavior characteristic of devices on planar substrates (**Figure 12a**). The *J*–*V* characteristics of an inverted device with the structure glass/PEDOT:PSS/PEI/P3OT:PCBM with a laminated PEDOT:PSS top contact are shown in **Figure 12b**. The footprint of the EGaIn droplet and the laminated PEDOT:PSS top contact[42] defined the active regions of the conventional and inverted devices, respectively. Optical microscopy did not reveal any cracks in the PEDOT:PSS top electrode after transfer in the inverted geometry.

Compared to the device in the conventional geometry with the EGaIn top electrode, the all-organic device exhibited a reduction in open-circuit voltage (V_{OC}) but an increase in short-circuit current density (J_{SC}) by approximately 27%. While we selected P3OT on the basis of its ability to survive conformal transfer, we did not optimize devices for efficiency, which we estimate to be around 0.36% for the inverted devices. There are several possible sources of inefficiency, the most prominent of which is the inferior charge-transport properties of P3OT, whose hole mobility as measured in field-effect transistors is ten to fifty times lower than that of P3HT.[45] Additionally, our process for transferring the films to hemispherical substrates proceeded in ambient air, and required a heating step. The geometry in which we measured these devices—with the cylindrical shaft of the test tube oriented toward the light source—probably reduced the diffuse contribution to the AM 1.5G spectrum impinging on the active area. The curved geometry also deflected the path of the light in ways we did not model. For the inverted

device, which has a transparent "top" anode, it was possible to measure the photovoltaic properties in two configurations: with the light incident on the glass surface (glass-incident) and the light incident directly on the device layers (device-incident, **Figure 12b**). We attribute the greater current density (27%) in the device-incident configuration to reduced reflective losses due to the glass surface and increased contributions from diffuse photons impinging on the active area.

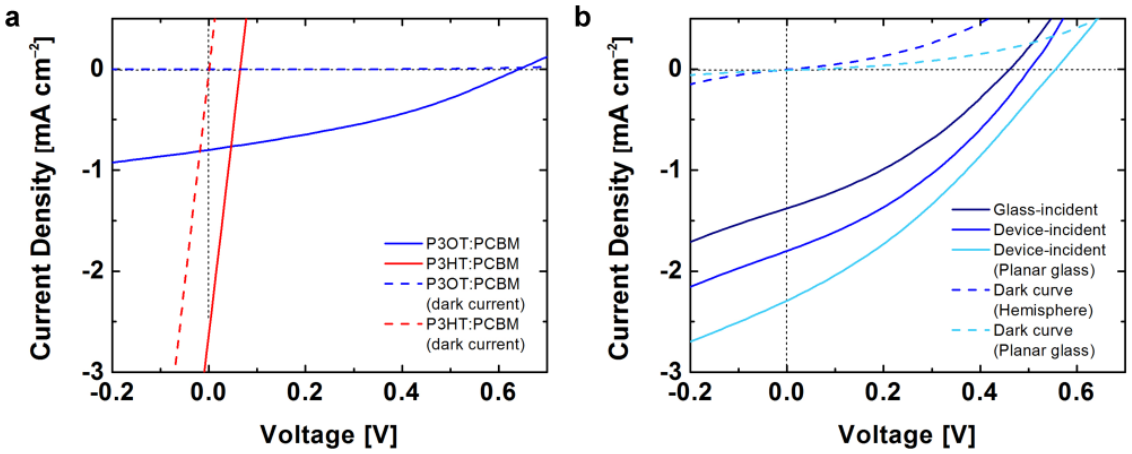

Figure 12: Representative photovoltaic characteristics of organic solar cells bonded to hemispherical substrates. (a) Current density vs. voltage (J-V) for devices in the conventional geometry: glass/PEDOT:PSS/P3AT:PCBM/EGaIn. and P3OT:PCBM devices stretched and bonded to hemispherical surfaces. Extensive cracking produced a J-V plot resembling a short circuit. (b) Current density vs. voltage for an all-organic device in the inverted geometry: glass/PEDOT:PSS/PEI/P3OT:PCBM/PEDOT:PSS. The chart includes three plots: the device on the hemispherical surface with the light impinging on the concave surface (glass-incident) and the convex surface (device-incident) and a separate device prepared on planar glass (also device-incident).

We attempted to fabricate inverted devices using P3HT:PCBM as the active material, but were unsuccessful, because the process of transferring the PEDOT:PSS top contact inadvertently delaminated the PEDOT:PSS/PEI/P3HT:PCBM film already present on the hemispherical substrate. This inadvertent delamination was initiated at

edges (as shown schematically in **Figure 13** in the case of planar glass). The extensive cracking of the brittle P3HT:PCBM film caused extensive delamination of the active material in every attempt at transferring the top contact. In the uncracked P3OT:PCBM devices, the transfer was facilitated by the physical contiguity of the active layer.

2.3.6 – YIELD

We estimate a yield in transferring films comprising active layer material, P3AT:PCBM, and partial devices, PEDOT:PSS/(PEI)/P3AT:PCBM from FOTS-treated glass to PDMS of >90% ($N > 50$), and the yield of transferring these films from PDMS to the hemispherical glass surface was >95% ($N > 45$). In inverted architectures, which require the transfer of a PEDOT:PSS top contact, the yield of transfer of the top contacts was ≥50% ($N > 10$). Using the most successful version of the process we developed, we measured a photovoltaic effect in 100% (7/7) of conventional cells employing EGaIn as a top contact, and ~28% (2/7) of inverted cells employing PEDOT:PSS as both the top and bottom electrodes. We believe that sub-optimal yields and efficiencies are in part a consequence of the manual processes used, most of which proceeded in ambient air. Automated processing in an inert environment would, we believe, improve the yields and efficiencies substantially.

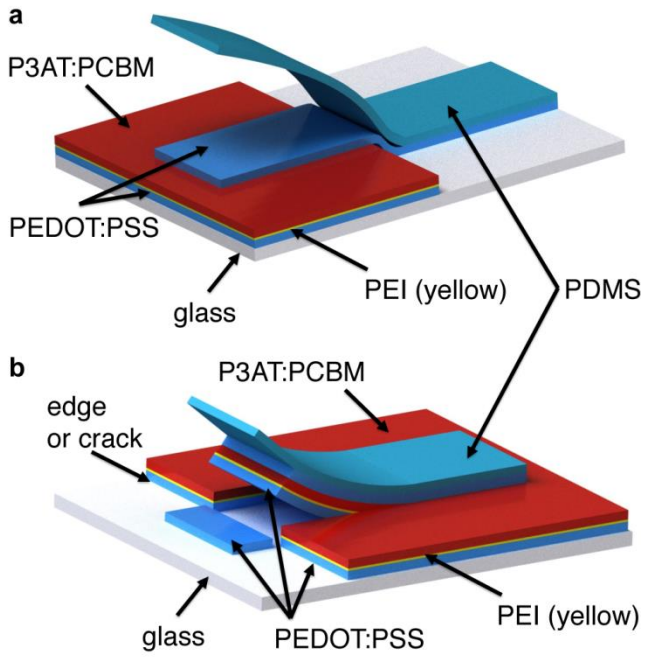

Figure 13: Schematic drawings of the successful (a) and unsuccessful (b) processes intended to transfer the PEDOT:PSS top contact to the glass/PEDOT:PSS/PEI/P3AT:PCBM device bonded to a glass substrate. The process is shown on planar glass, but the same effects were observed on hemispherical glass. In image (a) the transfer proceeded from a physically continuous region of the active layer to a region of bare glass, and the PEDOT:PSS film is transferred intact. In image (b), the transfer is initiated from—or passes over—an edge (which could be produced by a crack). Instead of transferring the PEDOT:PSS top contact, the layers already present on the glass substrate are inadvertently delaminated. We attribute successful transfer in mode (a) to the physical contiguity of the active layer (as in P3OT:PCBM devices) and unsuccessful transfer in mode (b) to extensive cracking (as in P3HT:PCBM devices).

2.4 – CONCLUSION

This paper described a process to stretch and transfer conjugated polymer films and complete, all-organic solar cells to hemispherical surfaces. The process was enabled by a consideration of the mechanical properties of conjugated polymers, in particular, that the elasticity of regioregular polythiophenes increases by a factor of seven with an increase in the length of the alkyl pendant groups, from hexyl to octyl with increasing length of the alkyl chain, with a corresponding increase in ductility. A computational

simulation of the strain required to bond a thin film to a hemispherical substrate enabled our prediction that the increased ductility of P3OT:PCBM over P3HT:PCBM would permit bonding of the more ductile polymer-fullerene composite without wrinkling or cracking. Our experiments and analysis suggest that mechanical properties must be considered when selecting materials destined to experience mechanical deformation, and that seemingly minor structural variations—*i.e.,* the addition of two methylene units in the pendant group—can either enable or prevent a material from performing in an application. Our results may suggest the design of new materials that maximize both electronic performance and mechanical compliance.

There are two classes of unconventional form factors to which stretchable electronic systems are applicable: those that require reversible response to strain for integration with moving parts of machines or the body and those that require one-time bonding to a non-planar surface. The former category requires elasticity, while for the latter ductility is sufficient. The work described falls into the latter category, as the films accommodated the strain principally by plastic deformation. Applications of one-time bonding of plastically deformable electronic devices to non-planar surfaces could include integration with windshields or eyeglasses for semitransparent heads-up displays, integration with the curved surfaces of biomedical implants (as in electronic eye cameras[39] or artificial retinas[10]), or bonding to nonplanar surfaces for applications requiring biofeedback (e.g., fatigue-sensing steering wheels and human-interactive robotics). Deformable organic solar cells in particular may find use in similar applications and also when bonded to architectural elements or the exteriors of vehicles in ways that neither compromise aesthetics nor aerodynamics. The selection of materials

on the basis not only of electronic but also of mechanical properties is required. We believe our observations may provide some insights into the realization of truly “plastic” electronics.

2.5 – EXPERIMENTAL METHODS

2.5.1 – MATERIALS

For the hemispherical substrates, we used borosilicate test tubes (d = 16 mm, l = 125 mm) from Fischer Scientific. Planar glass substrates were microscope slides obtained from Premiere. PEDOT:PSS (Clevios PH1000) was purchased from Heraeus. The solid content of the PH 1000 solution was 1–1.3% and had a ratio of PEDOT to PSS of 1:2.5 by weight. (Tridecafluoro-1,1,2,2,-tetrahydrooctyl)-trichlorosilane (FOTS) was purchased from Gelest. Zonyl FS-300 (Zonyl), DMSO, ortho-dichlorobenzene (ODCB), poly(3-hexylthiophene) (P3HT), poly(3-octylthiophene) (P3OT), [6,6]-phenyl C_{61} butyric acid methyl ester (PCBM, >99%), and eutectic gallium-indium (EGaIn, ≥99.99%) were purchased from Sigma-Aldrich and used as received. The PDMS was prepared by puddle-casting a mixed and degassed PDMS prepolymer with a thickness of 1 mm (Dow Corning Sylgard 184, with a ratio of base to crosslinker of 10:1 by mass) in a polystyrene petri dish. It was then cured at ambient temperature for 48 h and cut into 4 cm × 4 cm squares. The surface cured at the air interface was used for all experiments.

2.5.2 – FABRICATION OF DEVICES AND BONDING TO HEMISPHERICAL SURFACES

We began by cutting 2.5 cm × 2.5 cm glass slides and sonicating them for 10 min each in deionized water with Alconox, pure deionized water, acetone, and isopropanol. In between each sonication step the slides were blown dry with compressed air. After the final sonication and drying step, the slides were treated in a plasma cleaner (30 W, 200 mtorr ambient air, 3 min) and subsequently placed in a vacuum desiccator containing a vial of ~100 μL FOTS. Dynamic vacuum was applied for a minimum of 3 h. The PEDOT:PSS was filtered through a syringe filter (1 μm glass microfiber filter) to remove large particles. The composition of PEDOT:PSS was 94% by weight PEDOT:PSS, 5% by weight DMSO, and 1% by weight Zonyl. We spin-coated the solution onto the FOTS-treated glass at 700 rpm for 60 s then 2 krpm for 60 s. The slides were then dried on a hot plate in ambient air for 30 min at 150 °C. For devices to be measured in the inverted architecture, we spin-coated PEI at a concentration of 1% in methoxyethanol at a speed of 3 krpm for 60 s atop the dried PEDOT:PSS layer. This layer was annealed on a hotplate in air at 110 °C for 10 min.

The active layer solution was prepared with a 1:1 solution of P3HT:PCBM or P3OT:PCBM in ODCB and stirred overnight at room temperature (40 mg mL^{-1} total). We then filtered these solutions through a 0.2 μm PTFE syringe filter and spin-coated them onto the FOTS-treated slides bearing a film of PEDOT:PSS(/PEI) at 500 rpm for 180 s then 2 krpm for 20 s. Dust was removed from the 4 cm × 4 cm PDMS squares using Scotch tape. We placed the clean surface of the PDMS against the PEDOT:PSS/P3AT:PCBM bilayer and established a conformal seal with the aid of gentle pressure from tweezers, such that the film was centered in the PDMS stamp. One edge of

the PDMS was held and lifted at a rate of ~10 cm s^{-1}so as to quickly peel the PDMS off; this fast action transferred the film from the glass to the PDMS.

The PDMS/P3AT:PCBM/(PEI/)PEDOT:PSS substrates were mounted in a clamp bearing a circular aperture (d = 30 mm). The hemispherical bottoms of borosilicate test tubes were wiped with isopropanol and plasma treated (30W, 500 mtorr air, 3 min). The tubes were subsequently mounted onto the computer-controlled linear actuator. The test tube was advanced toward the immobilized PDMS membrane until it made contact, and then driven 8 mm into the PDMS membrane at a rate of 0.25 mm s^{-1}. This action deformed the PDMS membrane, which conformed to the hemispherical bottom of the test tube. Once at its maximum displacement, heat was applied to the convex side of the PDMS substrate for 30 s, which reached a temperature of 75 °C, as measured with a thermocouple. The test tube was then withdrawn from the suspended PDMS membrane at a rate of 0.25 mm s^{-1}. Slow withdrawal transferred the PEDOT:PSS(/PEI)/P3AT:PCBM film to the hemispherical surface in the area of contact with the test tube.

2.5.3 – FABRICATION OF DEVICES WITH THE CONVENTIONAL ARCHITECTURE

Starting with a test tube whose hemispherical bottom surface bore a PEDOT:PSS/P3AT:PCBM bilayer film, a region of PEDOT:PSS was exposed by wiping away the P3AT:PCBM layer using a swab soaked with chloroform. Silver paint was then used to facilitate contact between the PEDOT:PSS and the copper wire. A droplet of EGaIn was placed manually onto a portion of the active layer ~4.5 mm from the apex of

the hemisphere. A second copper wire was then inserted into the EGaIn droplet and secured to the glass tube with tape.

2.5.4 – FABRICATION OF DEVICES WITH THE INVERTED ARCHITECTURE

For devices with the inverted architecture, we laminated a top contact of PEDOT:PSS on top of the three-layer structure PEDOT:PSS/PEI/P3OT:PCBM. We used a modification of the procedure described by Janssen and coworkers to transfer the top PEDOT:PSS electrode to the P3OT:PCBM surface.[42] Briefly, partially cured PDMS substrates (10:1 base to crosslinker) were prepared by puddle casting and cured at 70 °C for 25 min, then immediately placed in a refrigerator (8 °C) to reduce the rate of crosslinking. These PDMS substrates were treated in a plasma cleaner (30 W, 500 mtorr ambient air, 10 s) and PEDOT:PSS (containing 5% DMSO) was subsequently spin-coated. The PDMS/PEDOT:PSS substrates were allowed to dry in air for 5 min, after which they were cut into strips. The substrates were then immediately placed onto the partially completed hemispherical devices with the PEDOT:PSS layer in contact with the P3OT:PCBM layer, heated to ~80 °C for 30 s with a heat gun, then allowed to cool to room temperature. After cooling, the PDMS was mechanically peeled from the hemisphere. This action left the PEDOT:PSS top contacts in place. We made electrical contact with the PEDOT:PSS top contacts by attaching a copper wire using silver paint as a conductive adhesive. Wiping away a few square mm of the P3AT:PCBM film exposed a region of PEDOT:PSS/PEI film, to which we also made contact by attaching a copper wire with silver paint.

2.5.5 – COMPUTATIONAL MODELING OF STRAIN

We modeled the distribution of strain needed for the conjugated polymer films to conform to the hemispherical substrates using finite element analysis static linear mechanical simulations. A representative 3D model of the experimental set-up was created in Autodesk Inventor 2014 software suite. We input the corresponding dimensions and mechanical properties of each component of the experimental system into the software, as follows. The end of the glass test tube was modeled as a solid glass hemisphere with the radius of 8 mm. A square PDMS membrane (50 mm × 50 mm × 1 mm) was sandwiched between two steel plates, each having a 30 mm circular aperture through the center. The contacts between the membrane and the plates were setup as bonded (no slipping). Translation of the glass hemisphere was constrained to the axis orthogonal to the plane of the membrane through the center of the circular apertures in the steel plates. The contact between the glass hemisphere and the PDMS membrane was setup as to have no slipping (in the experimental system, the conjugated polymer films were on the side of the PDMS membrane facing the glass hemisphere). These contact parameters generated simulated results that were most representative of our experimental data. Further, the orthogonal load of 0.75 N was applied to the flat surface of the hemisphere. The load resulted in the axial displacement of the hemisphere by 8 mm into (and deforming) the PDMS membrane. The simulation assumed that the PDMS substrate accommodated all of the deformation, and that the glass hemisphere remained rigid.

2.5.6 – PHOTOVOLTAIC MEASUREMENTS.

We performed all photovoltaic measurements in a nitrogen-filled glovebox using a solar simulator approximating the AM 1.5G spectrum with a flux of 100 mW cm^{-2} (ABET Technologies 11016-U up-facing unit calibrated with a reference cell with a KG5 filter).

2.6 – ACKNOWLEDGEMENTS

This work was supported by the Air Force Office of Scientific Research (AFOSR) Young Investigator Program, grant number FA9550-13-1-0156. Additional support was provided by laboratory startup funds from the University of California, San Diego. A. Z. acknowledges a fellowship from SoCal Clean Energy Technology Acceleration Program from the von Liebig Center at UCSD sponsored by the US Department of Energy. S. S. acknowledges a fellowship from the National Science Foundation Graduate Research Fellowship Program under Grant No. DGE-1144086. M. I. D. acknowledges support from the Calit2 High School Summer Scholars Program at UCSD. The authors thank Dr. Ryan Chiechi and Thomas Voortman for measurements of molecular weight of the polymer.

Chapter 2, in full, is a reprint of the material as it appears in “Stretching and conformal bonding of organic solar cells to hemispherical surfaces,” Timothy F. O'Connor, Aliaksandr V. Zaretski, Bijan A. Shiravi, Suchol Savagatrup, Adam D. Printz, Mare Ivana Diaz, Darren J. Lipomi. Energy & Environmental Science, 2014. The dissertation author was the primary investigator and author of this paper.

2.7 – REFERENCES

[1] M. Kaltenbrunner, M. S. White, E. D. Glowacki, T. Sekitani, T. Someya, N. S. Sariciftci and S. Bauer, Nat. Comm., 2012, 3, 770.

[2] G. Li, R. Zhu and Y. Yang, Nat. Photonics, 2012, 6, 153-161.

[3] D. Tahk, H. H. Lee and D. Y. Khang, Macromolecules, 2009, 42, 7079-7083.

[4] B. O'Connor, E. P. Chan, C. Chan, B. R. Conrad, L. J. Richter, R. J. Kline, M. Heeney, I. McCulloch, C. L. Soles and D. M. DeLongchamp, ACS Nano, 2010, 4, 7538-7544.

[5] D. J. Lipomi, H. Chong, M. Vosgueritchian, J. G. Mei and Z. N. Bao, Sol. Energy Mater. Sol. Cells, 2012, 107, 355-365.

[6] S. R. Dupont, M. Oliver, F. C. Krebs and R. H. Dauskardt, Sol. Energy Mater. Sol. Cells, 2012, 97, 171-175.

[7] V. Brand, C. Bruner and R. H. Dauskardt, Sol. Energy Mater. Sol. Cells, 2012, 99, 182-189.

[8] D. J. Lipomi, B. C.-K. Tee, M. Vosgueritchian and Z. N. Bao, Adv. Mater., 2011, 23, 1771-1775.

[9] F. C. Krebs, M. Biancardo, B. Winther-Jensen, H. Spanggard and J. Alstrup, Sol. Energy Mater. Sol. Cells, 2006, 90, 1058-1067.

[10] D. Ghezzi, M. R. Antognazza, R. Maccarone, S. Bellani, E. Lanzarini, N. Martino, M. Mete, G. Pertile, S. Bisti, G. Lanzani and F. Benfanati, Nat. Photonics, 2013, online. DOI: 10.1038/NPHOTON.2013.34.

[11] S. Wagner and S. Bauer, MRS Bull., 2012, 37, 207-213.

[12] Z. Suo, MRS Bull., 2012, 37, 218-225.

[13] T. Sekitani and T. Someya, Adv. Mater., 2010, 22, 2228-2246.

[14] J. A. Rogers, T. Someya and Y. G. Huang, Science, 2010, 327, 1603-1607.

[15] Y. G. Sun, W. M. Choi, H. Q. Jiang, Y. G. Y. Huang and J. A. Rogers, Nat. Nanotechnol., 2006, 1, 201-207.

[16] J. Jones, S. P. Lacour, S. Wagner and Z. G. Suo, J. Vac. Sci. Tech. A, 2004, 22, 1723-1725.

[17] D. H. Kim, N. S. Lu, R. Ma, Y. S. Kim, R. H. Kim, S. D. Wang, J. Wu, S. M.

Won, H. Tao, A. Islam, K. J. Yu, T. I. Kim, R. Chowdhury, M. Ying, L. H. Xu, M. Li, H. J. Chung, H. Keum, M. McCormick, P. Liu, Y. W. Zhang, F. G. Omenetto, Y. Huang, T. Coleman and J. A. Rogers, Science, 2011, 333, 838-843.

[18] J. Lee, J. A. Wu, M. X. Shi, J. Yoon, S. I. Park, M. Li, Z. J. Liu, Y. G. Huang and J. A. Rogers, Adv. Mater., 2011, 23, 986-991.

[19] I. M. Graz, D. P. J. Cotton and S. P. Lacour, Appl. Phys. Lett., 2009, 98, 071902.

[20] T. Sekitani and T. Someya, MRS Bull., 2012, 2012, 236-245.

[21] T. Sekitani, Y. Noguchi, K. Hata, T. Fukushima, T. Aida and T. Someya, Science, 2008, 321, 1468-1472.

[22] D. J. Lipomi and Z. N. Bao, Energ. Environ. Sci., 2011, 4, 3314-3328.

[23] C. Muller, S. Goffri, D. W. Breiby, J. W. Andreasen, H. D. Chanzy, R. A. J. Janssen, M. M. Nielsen, C. P. Radano, H. Sirringhaus, P. Smith and N. Stingelin-Stutzmann, Adv. Funct. Mater., 2007, 17, 2674-2679.

[24] Z. B. Yu, X. F. Niu, Z. Liu and Q. B. Pei, Adv. Mater., 2011, 23, 3989-3994.

[25] O. Awartani, B. Lemanski, H. W. Ro, L. J. Richter, D. M. DeLongchamp and B. T. O'Connor, Adv. Energy Mater., 2013, 3, 399-406.

[26] Y. Cao, P. Smith and A. J. Heeger, Polymer, 1991, 32, 1210-1218.

[27] S. Tokito, P. Smith and A. J. Heeger, Synthetic Met., 1990, 36, 183-194.

[28] J. Moulton and P. Smith, Polymer, 1992, 33, 2340-2347.

[29] A. Facchetti, Chem. Mater., 2011, 23, 733-758.

[30] F. C. Krebs, M. Jorgensen, K. Norrman, O. Hagemann, J. Alstrup, T. D. Nielsen, J. Fyenbo, K. Larsen and J. Kristensen, Sol. Energy Mater. Sol. Cells, 2009, 93, 422-441.

[31] F. C. Krebs, T. D. Nielsen, J. Fyenbo, M. Wadstrom and M. S. Pedersen, Energ. Environ. Sci., 2010, 3, 512-525.

[32] C. J. Bettinger and Z. N. Bao, Adv. Mater., 2010, 22, 651-655.

[33] A. R. Postema, K. Liou, F. Wudl and P. Smith, Macromolecules, 1990, 23, 1842-1845.

[34] D. J. Lipomi, M. Vosgueritchian, B. C.-K. Tee, C. H. Fox, J. A. Lee and Z. N. Bao, Nat. Nanotechnol., 2011, 6, 788-792.

[35] S. Savagatrup, A. S. Makaram, D. J. Burke and D. J. Lipomi, Adv. Funct. Mater., 2013, DOI: 10.1002/adfm.201302646.

[36] J. T. Seitz, J. Appl. Polym. Sci., 1993, 49, 1331-1351.

[37] L. E. Nielsen and R. R. Landel, Mechanical Properties of Polymers and Composites, CRC Press, New York, 1994.

[38] R. D. McCullough, Adv. Mater., 1998, 10, 93-116.

[39] H. C. Ko, M. P. Stoykovich, J. Z. Song, V. Malyarchuk, W. M. Choi, C. J. Yu, J. B. Geddes, J. L. Xiao, S. D. Wang, Y. G. Huang and J. A. Rogers, Nature, 2008, 454, 748-753.

[40] M. A. Meitl, Z. T. Zhu, V. Kumar, K. J. Lee, X. Feng, Y. Y. Huang, I. Adesida, R. G. Nuzzo and J. A. Rogers, Nat. Mater., 2006, 5, 33-38.

[41] Y. H. Zhou, C. Fuentes-Hernandez, J. W. Shim, J. Meyer, A. J. Giordano, H. Li, P. Winget, T. Papadopoulos, H. Cheun, J. Kim, M. Fenoll, A. Dindar, W. Haske, E. Najafabadi, T. M. Khan, H. Sojoudi, S. Barlow, S. Graham, J. L. Bredas, S. R. Marder, A. Kahn and B. Kippelen, Science, 2012, 336, 327-332.

[42] D. Gupta, M. M. Wienk and R. A. J. Janssen, Adv. Energy Mater., 2013, 3, 782.

[43] N. S. Lu, X. Wang, Z. G. Suo and J. Vlassek, Appl. Phys. Lett., 2007, 91, 221909.

[44] D. J. Lipomi, J. A. Lee, M. Vosgueritchian, B. C.-K. Tee, J. A. Bolander and Z. N. Bao, Chem. Mater., 2012, 24, 373-382.

[45] A. Babel and S. A. Jenekhe, Synthetic Met., 2005, 148, 169-173.

CHAPTER 3 – WEARABLE ORGANIC SOLAR CELLS WITH HIGH CYCLIC BENDING STABILITY: MATERIALS SELECTION CRITERIA

Timothy F. O'Connor, Aliaksandr V. Zaretski, Suchol Savagatrup, Adam D. Printz, Cameron D. Wilkes, Mare Ivana Diaz, Eric J. Sawyer, and Darren J. Lipomi*

Department of NanoEngineering, University of California, San Diego

9500 Gilman Drive, Mail Code 0448, La Jolla, CA 92093-0448

3.1 – ABSTRACT

Despite the intrinsic flexibility of organic electronic materials due to their thinness, a deliberate selection of materials on the basis of their mechanical—not just charge-transport—properties is required for applications with mechanically demanding form factors, such as exist in the field of wearable electronics. This paper describes a skin-wearable solar cell enabled by the deliberate selection or intentional plasticization of the components to enable an extreme level of stability under cyclic bending deformations. In particular, poly(3,4-ethylenedioxythiophene):poly(styrenesulfonate) (PEDOT:PSS) films plasticized with 10 percent fluorosurfactant are used for both the anode and cathode, with the cathode layer further modified with polyethyleneimine (PEI) to lower the work function. Use of poly(3-heptylthiophene) (P3HpT) instead of the far more common poly(3-hexylthiophene) (P3HT) as the electron donor permitted extreme deformation because of its increased mechanical compliance (owing to its low glass transition temperature). Cells fabricated on 13-μm polyimide tape and adhered to human

skin show stable performance when compressively strained by approximately 75 percent. These compressive strains produce convex and concave buckles with minimum radii of curvature of ca. 100 μm. Finite-element modeling predicts that the films require the ability to withstand a range of strains of 10 percent, when both convex and concave bends are considered. These devices, enabled by the stretchable semiconductor P3HpT, withstand up to one thousand cycles of compression with less than 20 percent degradation in power conversion efficiency, whereas devices based on P3HT show greater degradation after only five cycles, and fail catastrophically by fifty cycles. The usefulness of the wearable solar cells is demonstrated by their abilities to power an LED and a digital watch.

3.2 – INTRODUCTION

The surest strategy to promote organic solar cells (OSCs) from laboratory-scale demonstrations to use in the real world is to exploit the advantages possessed by organics that would be difficult or impossible to replicate in more-efficient competing technologies.[1] Such advantages include low cost and embodied energy,[2] extreme thinness,[3] tunable color,[4] biodegradability,[5] semitransparency,[6] extreme flexibility,[3] and stretchability.[7] These characteristics suggest that portable power for displays,[8] mobile health monitoring devices, and mitigation of climate change triggered by burning of biomass in the developing world are—far from applications dismissible as "niche"—important problems for which organic solar cells may provide the ideal solutions.[9] While the community has produced impressive demonstrations in ultra lightweight organic solar cells that can tolerate small bending radii,[3] stability under

cyclic deformation—required for real-world applications—has been poor. This fragility is a consequence of the fact that typical systems of materials are optimized overwhelmingly on the basis of efficiency on rigid substrates, as opposed to on the basis of mechanical stability. In this communication, we show that a deliberate selection of materials optimized for their mechanical properties can enable a new type of skin-mountable solar cell that can be used to power wearable electronic devices; these solar cells exhibit unprecedented stability to cyclic bending deformation. We performed these experiments to understand and anticipate routes of mechanical and photochemical degradation for all-organic solar cells under realistic operating conditions.

Despite the attractiveness of organic semiconductors for flexible and stretchable applications,[1] the mechanical properties of these materials are highly variable, and there is a strong competition between compliance and charge transport.[10] The perceived compliance of optoelectronic polymers comes not because of their polymeric character, but because of the extreme thinness possible for the active layers of devices (ca. ≤100 nm).[11] Thus unconventional active materials (e.g., liquid metals),[12] processing conditions, and device layouts[13, 14] are generally required to produce devices stable enough to withstand extreme or repeated deformation, as would be encountered in ultra-thin, portable, or wearable applications.[15] The first wearable OSCs—i.e., integrated with clothing—were reported by Krebs in 2006.[16] While these devices were flexible, the substrates and encapsulants were relatively thick (>250 μm total thickness), and thus mechanical compliance was not maximized.[16]

The first stretchable organic solar cell was reported by Lipomi et al. in 2011.[17] In this device, an organic active layer was coated on a poly(dimethylsiloxane) (PDMS)

substrate under uniaxial tension. Release of the tension produced buckles in the active layer that accommodated subsequent cycles of strain. However, because of the unencapsulated liquid top contact—eutectic gallium-indium, an expensive material necessary to conform to the topography of the buckles—the device was not wearable because it could not be inverted.[17] Later, Kaltenbrunner et al. demonstrated an OSC on an ultrathin (1.4 μm) polyester foil capable of accommodating bending radii ≥10 μm.[3] This device represents the state of the art in ultrathin organic cells, but it showed poor stability under repeated compression when the whole device was mounted to an elastic substrate—27% reduction in efficiency after only 22 cycles of 50% compression—and all devices were measured in a nitrogen-filled glovebox.[3] Our goal was to fabricate devices that retained at least 80% of their initial efficiency up to 1,000 cycles of loading, on the skin, and in outdoor sunlight, by selecting materials optimized on the basis of mechanical stability.

3.3 – RESULTS AND DISCUSSION

Our laboratory and others[18-20] have elucidated many of the molecular and microstructural parameters that permit the coexistence of good electronic performance with extreme mechanical compliance.[7, 15] The process and materials we used are illustrated in **Figure 14**. We designed the device to have the "inverted" geometry (cathode on the bottom) and used a thin (13 μm) polyimide (PI) tape as the substrate. While substrates as thin as 1.4 μm have been used before,[3] these substrates are not available with an adhesive, and are mechanically more fragile than thicker ones. Crucially, we used the elastomeric conjugated polymer poly(3-heptylthiophene)

(P3HpT)[21] —in place of the typical poly(3-hexylthiophene) (P3HT)—because P3HpT is the first poly(3-alkylthiophene) with increasing length of the alkyl side chain whose glass transition is substantially below room temperature.[22] This property renders P3HpT about an order of magnitude less stiff than P3HT, and substantially more ductile.[21] The relative compliance of P3HpT compared to P3HT is preserved even when mixed with the typical fullerene acceptor, [6,6]-phenyl C_{61} butyric acid methyl ester (PCBM), which is an antiplasticizer for poly(3-alkylthiophenes) (P3ATs).[21] (In fact, the stiffening qualities of [60]PCBM are reduced when contaminated by up to 10% [70]PCBM—termed "technical grade" by manufacturers; thus, incompletely separated blends of methanofullerenes are substantially more compliant than pure samples, though we used 99% grade in this study for the sake of reproducibility.)[23] We used the typical transparent conductive polymer poly(3,4-ethylene dioxythiophene):poly(styrene sulfonate) (PEDOT:PSS) as both the anode and cathode.[24] We added 10% w/w Zonyl fluorosurfactant to the PEDOT:PSS solution to permit wetting on the PI substrate and also to plasticize the films by a factor of 100 relative to the unmodified polymer.[25] The cathode layer was modified with poly(ethylene imine) (PEI) to lower the work function.[24] Casting this layer from ethanol instead of the usual methoxyethanol (MOE) produced a substantially more resilient film (crack onset strain 16.5% for ethanol and 3% for methoxyethanol) possibly because methoxyethanol is a better solvent than ethanol for the plasticizer, Zonyl, and washed it away during spin-coating. **Figure 15** is a table summarizing the crack-onset strains for conventional materials, and those modified for increased stability.

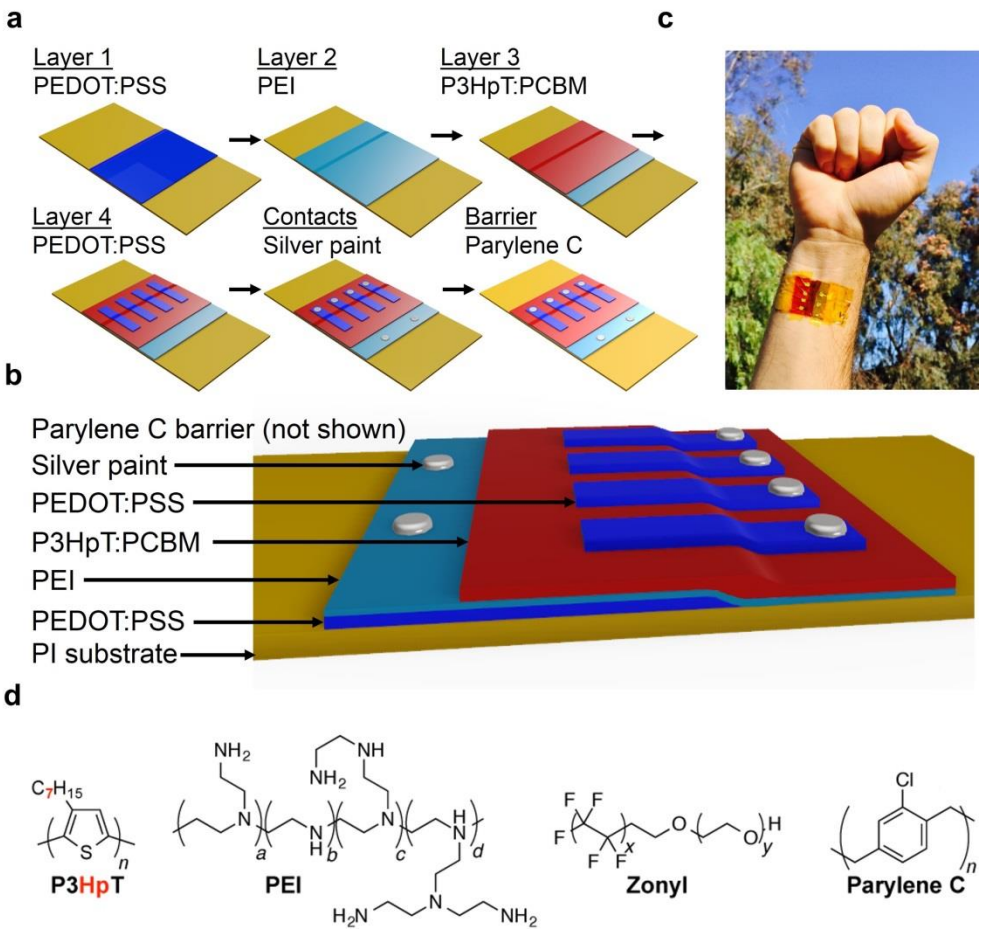

Figure 14: Fabrication of ultra-flexible, wearable OSCs. a) Schematic summary of the process used to fabricate wearable OSCs. Thin (13 µm) PI adhesive substrates were spin-coated with poly(3,4-ethylenedioxythiophene):poly(styrene sulfonate) (PEDOT:PSS), polyethyleneimine (PEI), and P3HpT:PCBM. PEDOT:PSS top-contacts are then transferred on top of the device using thermal release tape, and a strip of the active layer was wiped away to expose the bottom electrode. Silver paint was then applied to make electrical contact. b) Schematic diagram of the cross section of a wearable OSC. c) A photograph of the wearable solar cell on skin. d) Chemical structures of the critical materials used in this study.

Component	Material	Crack-onset strain (%)	Reference
Cathode	Aluminum	<1	this work
	Silver	<1	this work
	PEDOT:PSS:(5%)Zonyl/PEI(MOE)	3	this work
	PEDOT:PSS:(5%)Zony/PEI(EtOH)	**16.5 ± 2**	this work
Active layer (effect of polymer)	P3HT:[60]PCBM (99%)	1	this work
	P3HpT:[60]PCBM (99%)	**4 ± 1**	18
Active layer (effect of fullerene)	P3HT:[60]PCBM (99%)	1.25 ± 0.5	20
	P3HT:[60]PCBM:[70]PCBM (9:1)	1.75 ± 0.5	20
	P3HT:[60]PCBM:[70]PCBM (1:1)	**5.0 ± 1.0**	20
Anode	PEDOT:PSS	5 ± 1	22
	PEDOT:PSS:(10%)Zonyl	**35 ± 2**	22

Figure 15: Summary of crack onset strains on polymeric supports for different materials. The most mechanically stable materials are indicated in bold. All materials were deposited or transferred onto poly(dimethylsiloxane) (PDMS) supports, except for aluminum and silver, which were evaporated directly on polyimide tape.

Optical micrographs of the devices prior to mechanical deformation indicate that the layers are undamaged (**Fig. S1a**). Electron microscopy revealed that the device is smooth at 5,000× magnification (**Fig. S1b**). Devices were conformably adhered to the forearm of the experimenter, who provided written consent (**Figure 16a**). (The only safety concern was the possibility of irritation from contact with the pressure-sensitive adhesive on the polyimide tape, which is sometimes produced by medical bandages, but which we did not observe.) We compressed the devices manually by approximately 75% (**Figure 16b**). **Figure 16c** shows an instance in which the strain was accommodated by a single concave buckle, which corresponds to a radius of curvature of 128 μm. We used finite element analysis (FEA) of the device on skin for both convex and concave buckles to calculate the strain in both tensile (**Figure 16d**) and compressive (**Figure 16e**) modes. Simulations predicted peak strains of ±5%. Since the active areas in the device could

undergo either convex or concave buckling, we concluded that the active materials must be able to tolerate a dynamic range of strain of at least 10%.

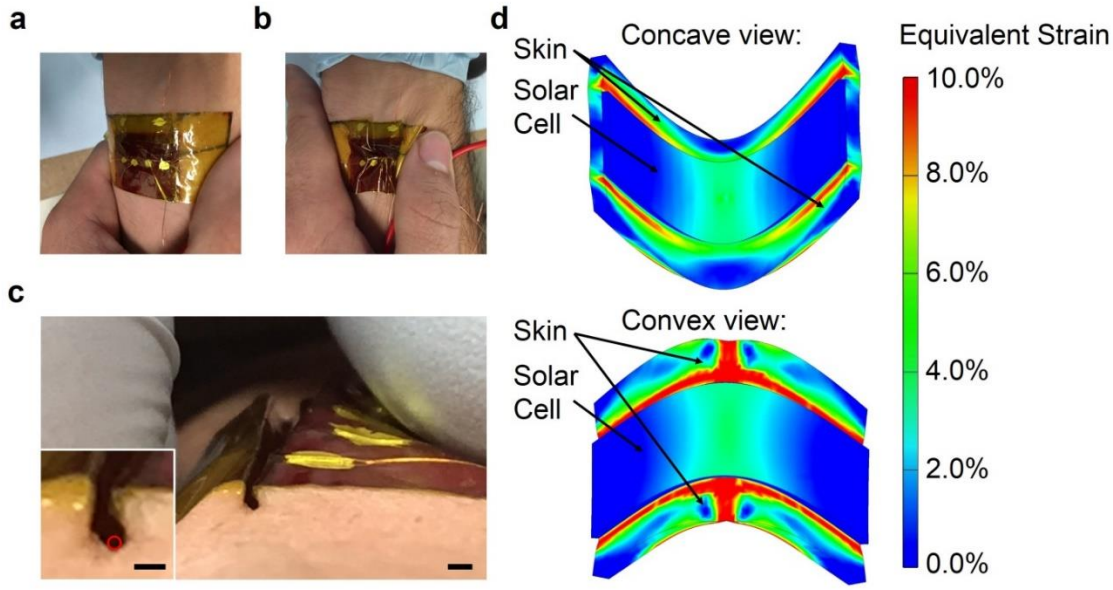

Figure 16: Mechanical deformation of OSCs on skin. a) Photograph of a wearable OSC under compression. b) Magnified image of the compression buckle on the solar cell device for clarity (scale bar = 500 µm). c) Fitted circles of radius 128 µm for an estimate of the radius of curvature (scale bar = 500 µm). d) Finite element analysis of PI substrates deformed with corresponding radius of curvature.

The yield of functional cells was 41 of 44 (93%). One cell from each substrate was selected to measure the stability of the photovoltaic properties when strained. **Figure 17a** shows a representative plot of the evolution of current density vs. voltage (*J*–*V*) for a cell as it was subjected to 1,000 cycles of 75% global compressive strain. Because these unencapsulated devices were measured in the ambient air, the total degradation represents a superposition of the chemical degradation[26] and the mechanical degradation.[15] **Figure 17b** illustrates this point by plotting the average normalized *PCE* of five cells that underwent mechanical deformation as a function of the number of cycles, and of five

cells that were uncycled. For the uncycled samples, the data points correspond to the time (upper *x*-axis) taken to apply strain to the cycled device. On average, devices subjected to 1,000 strain cycles retained 81.5 ± 1.9% of their initial efficiency, while uncycled cells retained 88.4 ± 1.4% (**Figure 17b**). Strained cells exhibited a sharp decrease in performance over the first 100 cycles. Devices exhibited similar behavior when measured in outdoor sunlight (**Figure 17c**). For comparison, seven substrates bearing four devices each were fabricated using P3HT:PCBM—as opposed to P3HpT:PCBM—as the active layer; five devices exhibited catastrophic failure before 400 cycles, and two failed as early as 25 cycles (one of which is represented in **Figure 17d**,). Devices were worn for less than 15 min at a time, and the chemical barrier properties of PI are sufficient to prevent exposure to the organic electronic materials or surfactants.

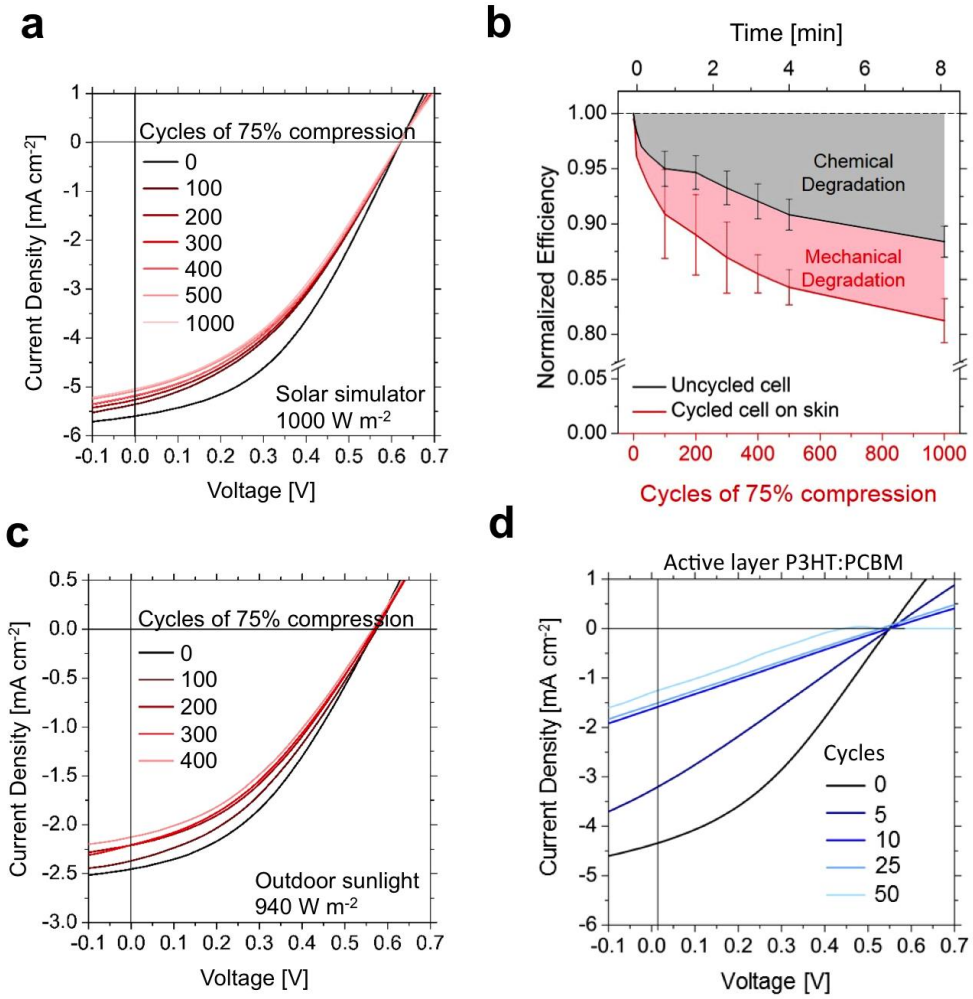

Figure 17: Electrical characteristics of wearable solar cells with mechanical deformation and in the outdoor environment. a) Electronic characterization of the devices measured in air over 1,000 cycles of 75% compression. b) Normalized efficiency of wearable solar cells over 1,000 cycles at 75% strain (red) and of undeformed control cells whose properties were measured at time points that corresponded to the time required to compress the sample (black). c) Degradation over 400 cycles for a wearable solar cell measured in outdoor sunlight. d) Representative plot of the evolution in photovoltaic properties of a wearable solar cell whose active layer comprised P3HT:PCBM (not P3HpT:PCBM) from 0 to 50 cycles of 75% compression.

In order to understand the origin of the reduction in performance, we characterized the cells before and after mechanical cycling using optical microscopy. The optical micrographs depicted in **Fig. S2** exhibit little sign of mechanical deterioration in the cells before mechanical cycling (**Fig. S2a**), whereas devices that had been subjected

to 1,000 strain cycles (**S2b**) showed signs of damage in the form of pinhole fractures and microscopic, localized delamination (**S2c**). To isolate the possible effects of damage to the PEDOT:PSS electrodes, we measured the electrical conductivity of these films (PEDOT:PSS on PI) under the same conditions of cyclic compression as used for the complete cells. We observed no change in resistance over 1,000 cycles of 75% compression.

To increase the stability of the devices against photochemical degradation for outdoor applications, a 1-μm barrier of parylene C was vapor deposited on the devices before attaching them to the skin. The practicality of these devices was then demonstrated by powering three different electronic devices (**Figure 18a-c**). The images in **Figure 18a-b** show wearable OSCs on skin powering a digital watch and an LED under 980 W m^{-2} of natural sunlight, as determined using a Daystar DS-05A digital solar meter. **Figure 18c** shows charging of a portable battery (though this device was powered by the solar simulator in the glovebox, see below). The *I-V* characteristics of these devices are plotted in **Figure 18d-e**. Many low power devices, such as digital watches or biosensors, require only modest currents to function, but larger voltages than are generated by single-cell OSCs (e.g., 1.8 V and ~100 μA in the case of the digital watch). In order to produce the voltages required to power the watch, OSCs on a single substrate were wired in series to produce a device with a V_{OC} of 2.23V, and an operational voltage of V_{watch} = 2.18 when measured in the glovebox. The LED circuit required a minimum of 0.4 V and ~1 mA, which were achieved using two substrates and 8 cells. To activate the charging mode on the portable battery, 15 cells were wired in series yielding a device with a V_{pp} of 4.66 V

and a $I_{\text{max power}}$ of 201 μA. Because of the delicate nature of this device (i.e., number of wires needed to achieve V_{OC} ~ 8 V), it was not removed from the glovebox.

We then analyzed the effect of the 1-μm barrier of parylene C on the degradation of the devices on planar substrates (**Figure 18f**). During the first 10 min (taken to prepare devices for measurement outside the glovebox), we measured an average loss in efficiency of 36.4 ± 1.0% in the devices with no barrier, while protected devices only suffered a decrease of 4.8 ± 2.1%. The degradation was monitored every hour over the course of 5 h, after which the unencapsulated devices retained only 42.5 ± 3.3% of their initial efficiency, while encapsulated cells retained 82.3 ± 3.4%. Contrary to our expectations, the encapsulant did not increase the mechanical stability of these devices despite shifting the active materials closer to the neutral plane.[27] After 1,000 cycles of compression, encapsulated devices retained 68% of their initial efficiency. From this pilot experiment (three devices), the mechanical stability of devices that were encapsulated with 1 μm or 10 μm of parylene C was worse than any device without a barrier. Further, unlike the unencapsulated devices, whose mechanical degradation was insignificant between 500 and 1,000 cycles of compression (**Figure 17a**), encapsulated devices continued to degrade mechanically throughout the experiment. We attribute the increased mechanical degradation of the encapsulated devices to residual interfacial stress between the PEDOT:PSS top contact and the vapor-deposited parylene C film.

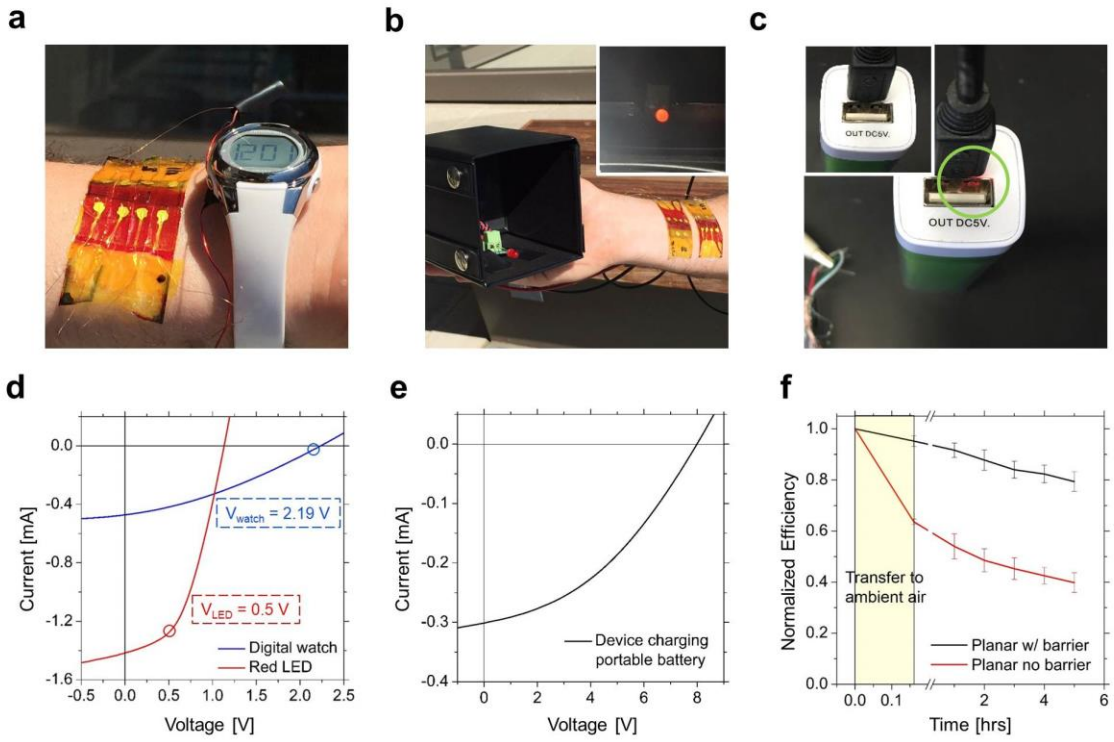

Figure 18: Applications of wearable OSCs. Wearable OSCs on skin powering: a) a wearable digital watch in outdoor sunlight and b) an LED in a minimalist Armstrong self-oscillating voltage booster circuit (a.k.a. a joule thief circuit) in outdoor sunlight (980 W m^{-2}). c) Wearable OSCs on a flat substrate powering a portable battery under 1 sun illumination of a solar simulator (the green circle shows that the battery pack is in charging mode and the inset clarifies that the device is not charging when there is no incident light on the OSC). Devices remained in the glove box and were illuminated by a solar simulator. d) Current-voltage characteristics of P3HpT:PCBM OSCs powering an LED (red), digital watch (blue) and e) charging a portable battery. Measurements were taken in the glove box with illumination provided by a solar simulator. f) Degradation characteristics of bare and parylene C encapulated OSCs in the laboratory air on planar substrates. The shaded area represents the degradation due to transferring the devices from within the glove box to their first measurement t = 0.

3.4 – CONCLUSION

In summary, this work described the first organic solar cell conformally bonded to human skin. This device was enabled by deliberate selection of semiconductors and electrodes that are known to exhibit intrinsic mechanical compliance—as opposed to compliance based on microfabricated relief structures[28] or fractal designs.[29, 30]

While this research used the organic solar cell as a model device, the knowledge generated of the materials, mechanics, and processing should be easily transferred to wearable and textile based organic light-emitters, RFID tags, thermoelectrics, and field-effect transistors for the burgeoning field of wearable electronics, mobile health monitors, electronic skin, and roll-to-roll processed organic devices exhibiting extreme mechanical stability.

3.5 – METHODS

3.5.1 – MATERIALS

Poly(3-hexylthiophene) (P3HT, M_n = 44 kDa, PDI = 2.0) and poly(3-heptylthiophene) (P3HpT, M_n = 35 kDa, PDI = 1.5) were produced by Rieke Metals, Inc. (P3HpT was obtained directly from Rieke Metals, Inc.; P3HT was produced by Rieke Metals, Inc., but sold by Sigma-Aldrich.) PDMS, Sylgard 184 (Dow Corning), was prepared according to the manufacturer's instructions at a ratio of 10:1 (base:crosslinker) and cured at room temperature for 36 to 48 h before it was used for mechanical testing. (Tridecafluoro-1,1,2,2-tetrahydrooctyl)-1-trichlorosilane (FOTS) was obtained from Gelest. PEDOT:PSS (Clevios PH1000) was purchased from Heraeus. DMSO was purchased from BDH with purity of 99.9% and Zonyl (FS-300) fluorosurfactant were purchased from Sigma-Aldrich. Chloroform ($CHCl_3$), ortho-dichlorobenzene (ODCB), acetone, isopropyl alcohol (IPA), and ITO-coated glass slides were obtained from Sigma-Aldrich and used as received. Zonyl (FS-300) fluorosurfactant, PEI, chloroform, ODCB, and isopropanol were purchased from Alfa Aesar. The PI tape was obtained from

Caplinq, product number PIT0.5S-UT/25.4. Leitsilber conductive silver paste was obtained from Ted Pella Inc. Thermal release tape (Revalpa 3196) was obtained from Nitto Denko.

3.5.2 – FABRICATION OF WEARABLE SOLAR CELLS

A step-by-step summary of the process used to fabricate the epidermal OSCs is shown in **Figure 14a**. The total thickness of the device was 13.7 μm, which comprised a 13-μm-thick PI substrate bearing a pressure-sensitive adhesive, a 190 nm PEDOT:PSS bottom-contact with a 10 nm PEI surface treatment to lower its work function (cathode),[20] a 130 nm P3HpT active layer, and a 250 nm PEDOT:PSS top-contact (anode). The substrate was prepared by adhering a 1×2-in strip of 13 μm PI tape to a glass slide, upon which the bottom electrode was deposited by spin coating a solution of PEDOT:PSS/DMSO/Zonyl (84:6:10) for 240 s at 400 rpm. The bottom contact was then heated for 30 min at 120 ˚C. Scotch tape was then used to pattern the bottom contact (by stripping unwanted regions) into a 1×0.75-in rectangle, such that the 1-in side occupied the entire width of the tape. Subsequently, the work function of the bottom electrode was lowered by depositing a surface layer of PEI by spin coating a 1.5% w/w solution of PEI in EtOH. The PEI was spin-coated in a 1x1-in region, as it also promoted the adhesion between P3HpT:PCBM and the PI tape in the subsequent step. The PEI layer was then heated at 110 ˚C for 10 min. The active layer was then added by spin-coating a 40 mg mL^{-1} solution of P3HpT:PCBM (1:1) in ODCB for 240 s at 500 rpm, then 15 s at 2 krpm. The device was then heated at 110 ˚C for 22 min in inert atmosphere. The top contacts

were transferred to the device using thermal release tape. PEDOT:PSS/DMSO/Zonyl was spin coated on the adhesive side of the thermal release tape for 240 s at 400 rpm. The tape was then cut into strips of the desired contact size and adhered to the surface of the device such that the PEDOT/PSS/Zonyl layer was in direct interface with the P3HpT:PCBM layer. The transfer was completed in an inert atmosphere by placing the devices on a hotplate that had been pre-heated to 135 ˚C for 30 s. It is critical to note that the top contact was positioned in an offset fashion from the bottom contact, such that a portion of the top contact did not have the bottom contact below it (see **Figure 14b**). If the silver paint was applied to the top-contact while the bottom contact was directly below, the silver paint shorted the top and bottom electrodes. The devices were then transferred from their glass substrates to wax paper substrates. The low energy surface of the wax paper reduced the adhesion of the substrate to its platform, and significantly decreased the incidence of delamination of the silver contact during transfer from the substrate used for fabrication to the skin. Lastly, silver paint and copper wires were added to the top contacts to make electrical contact with measurement equipment. Small strips of PI tape were used to secure the silver contacts during transfer and compression.

3.5.3 – YIELD

Of the forty-four devices prepared during the course of this study, three were not operational. Two of these devices exhibited short circuits and one exhibited an open circuit due to failure of a top contact to transfer. The average initial power conversion efficiency (*PCE*) for substrate-mounted devices in the glovebox was 1.02%, with a range from 0.7% to 1.71%. The initial average *PCE* of skin-mounted devices (before

mechanical testing) was 1.16% with a range of 0.79% to 1.39% and the average final efficiency (1,000 cycles of 75% compression) was measured to be 0.96% with a range of 0.6% to 1.19%. The reported average PCE for the skin-mounted cells is higher than the average for substrate-mounted cells because the skin-mounted cells (the best cell on each of five substrate bearing four cells each) were the best-performing subset of all devices made (all working cells on all substrates). As the goal of this study was to demonstrate a new purpose for ultra-flexible OSCs, we did not try to optimize the efficiency. The use of PEDOT:PSS as both the top and bottom contacts—and in particular, the lack of a reflective electrode, which ordinarily permits light to pass through the active layer a second time—and the roughness of the PI tape (**Fig. S2a**) could partially explain the initial efficiency that is less than that reported by other groups for ultrathin substrates.[3] The films were not observed to be rough on the nanoscale (**Fig. S2b**).

3.5.4 – MECHANICAL SIMULATIONS.

In order to obtain the strain distribution maps of the cells under compression cycles, a computer-assisted design (CAD) model of a skin patch with the polyimide tape attached to it was created in Autodesk Inventor 2015 suite with the corresponding material parameters applied to both parts. The modeled PI tape dimensions were 13 by 400 by 1200 μm, the skin patch dimensions were 52 by 800 by 1200 μm. A static linear finite element analysis (FEA) simulation of the buckling of the cells was then performed by bending the skin-supported PI tape around a rigid cylinder of the appropriate radius that corresponded to the typical experimentally measured bending radius of the cells, i.e., 128 μm. For the simulation, the skin/PI interface was selected as “bonded,” while the

skin/cylinder interface was selected as “sliding/no separation” in order to avoid extraneous stress on the assembly. The mesh size was selected as the 0.05 fraction of the smallest dimension of a part, while the minimal element size was the 0.1 fraction of the mesh size. The constraints were the following: the cylinder was fixed with zero degrees of freedom and the assembly was symmetrically aligned to the axis of the cylinder while maintaining the tangential constraint between the cylinder surface and the skin surface (in the case of concave bending) and the PI film surface (in the case of convex bending). Further a 0.1 N force was applied to the PI film edges parallel to the cylinder axis in order to induce bending. Maps of equivalent strain were obtained and the color bar scale was constrained to represent maximum 10% strain in order to not oversaturate the strain map on the PI surface (skin has a much lower elastic modulus and strains to a much higher degree). We note that the deformation of the skin in the vicinity of the device is substantial because of the mismatch in mechanical properties between the PI tape (tensile modulus = 2.5 GPa) and the skin (0.02 GPa).

3.5.5 – CYCLING STUDIES

Wearable OSCs were transferred from their fabrication platforms to the skin, then cycled at 75% strain in ambient conditions (i.e., outside of the glovebox) for up to 1,000 cycles. The strain cycling was performed by manually compressing the device by 75%. Image analysis was used to measure the amount of compression. OSCs were also subjected to cycling outdoors, under natural sunlight.

3.5.6 – CRACK-ONSET MEASUREMENTS

To measure crack on-set strain, the polymer films were prepared by spin-coating to produce a film of ~100 nm thickness. The films were then transferred onto unstrained PDMS rectangles. The rectangles were then stretched from 0% to the crack-onset strain using a linear actuator with a step size of 0.5% using a computer-controlled stage. At each step, optical microscope images of the films were taken in order to observe the generation of cracks. The crack on-set strain of each conjugated polymer was defined as the strain at which the first crack was observed. To determine the crack-onset of metal films, the metals were deposited onto PI substrates though thermal evaporation, and subsequently strained on the PI substrates, without transfer to PDMS.

3.5.7 – BARRIER STUDIES

A parylene C barrier of 1 μm thickness was deposited on wearable OSCs by means of vapor deposition using a PDS 2010 Parylene Coater. OSCs were transported to the parylene coater in inert atmosphere, limiting the effect of chemical degradation to roughly 30 s. After encapsulation, devices were protected from light as they were transported back to inert atmosphere for measurement and storage. Encapsulated and unencapsulated solar cells were subject to ambient conditions (i.e., atmospheric environment and 0.03 W m^{-2} of light) between measurements and were only exposed to intense (1,000 W m^{-2}) illumination during measurement.

3.5.8 – POWERING DEVICES

The digital watch was powered by a four solar cells on a single substrate. The cells were separated using a razor blade, then wired together in series. The LED circuit

was powered using two substrates. The four cells on each substrate were first wired together in parallel, creating a two devices each with four times the effective area. These two devices were then wired in series. The portable battery was powered by wiring 15 cells in series. All of the individual cells had areas of approximately 0.1 cm^2.

3.6 – ACKNOWLEDGEMENTS

This work was supported by the Air Force Office of Scientific Research (AFOSR) Young Investigator Program, grant number FA9550-13-1-0156. T.O. acknowledges support from the National Defense Science and Engineering Graduate Fellowship. S.S. and A.Z. acknowledge support provided by the National Science Foundation Graduate Research Fellowship.

Chapter 3, in full, is a reprint of the material as it appears in . "Wearable organic solar cells with high cyclic bending stability: Materials selection criteria," Timothy F. O'Connor, Aliaksandr V. Zaretski, Suchol Savagatrup, Adam D. Printz, Cameron D. Wilkes, Mare Ivana Diaz, Eric J. Sawyer, and Darren J. Lipomi. Solar Energy Materials and Solar Cells, 2016. The dissertation author was the primary investigator and author of this paper.

3.7 – REFERENCES

[1] L.T. Dou, J.B. You, Z.R. Hong, Z. Xu, G. Li, R.A. Street, Y. Yang, 25th Anniversary article: A decade of organic/polymeric photovoltaic research, Adv. Mater., 25 (2013) 6642-6671.

[2] N. Espinosa, M. Hosel, D. Angmo, F.C. Krebs, Solar cells with one-day energy payback for the factories of the future, Energ. Environ. Sci., 5 (2012) 5117-5132.

[3] M. Kaltenbrunner, M.S. White, E.D. Glowacki, T. Sekitani, T. Someya, N.S. Sariciftci, S. Bauer, Ultrathin and lightweight organic solar cells with high flexibility, Nat. Comm., 3 (2012) 770.

[4] C.M. Amb, M.R. Craig, U. Koldemir, J. Subbiah, K.R. Choudhyry, S.A. Gevorgyan, M. Jorgensen, F.C. Krebs, F. So, J.R. Reynolds, Aesthetically pleasing conjugated polymer:fullerene blends for blue-green solar cells via roll-to-roll processing, ACS Appl. Mater. Interfaces, 4 (2012) 1847-1853.

[5] M. Strange, D. Plackett, M. Kaasgaard, F.C. Krebs, Biodegradable Polymer Solar Cells, Sol. Energy Mater. Sol. Cells, 92 (2008) 805-813.

[6] J.Y. Lee, S.T. Connor, Y. Cui, P. Peumans, Semitransparent Organic Photovoltaic Cells with Laminated Top Electrode, Nano Lett., 10 (2010) 1276.

[7] S. Savagatrup, A.D. Printz, T.F. O'Connor, A.V. Zaretski, D.J. Lipomi, Molecularly stretchable electronics, Chem. Mater., 26 (2014) 3028-3041.

[8] M.S. White, M. Kaltenbrunner, E.D. Glowacki, K. Gutnichenko, G. Kettlgruber, I. Graz, S. Aazou, C. Ulbricht, D.A.M. Egbe, M.C. Miron, Z. Major, M. Scharber, T. Sekitani, T. Someya, S. Bauer, N.S. Sariciftci, Ultrathin, highly flexible and stretchable PLEDs, Nat. Photonics, 7 (2013) 811-816.

[9] F.C. Krebs, T.D. Nielsen, J. Fyenbo, M. Wadstrom, M.S. Pedersen, Manufacture, integration and demonstration of polymer solar cells in a lamp for the "Lighting Africa" initiative, Energ. Environ. Sci., 3 (2010) 512-525.

[10] O. Awartani, B. Lemanski, H.W. Ro, L.J. Richter, D.M. DeLongchamp, B.T. O'Connor, Correlating Stiffness, Ductility, and Morphology of Polymer:Fullerene Films for Solar Cell Applications, Adv. Energy Mater., 3 (2013) 399-406.

[11] J.A. Rogers, M.G. Lagally, R.G. Nuzzo, Synthesis, assembly and applications of semiconductor nanomembranes, Nature, 477 (2011) 45-53.

[12] J.H. So, H.J. Koo, M.D. Dickey, O.D. Velev, Ionic current rectification in soft-matter diodes with liquid-metal electrodes, Adv. Funct. Mater., 22 (2012) 625-631.

[13] M. Kaltenbrunner, T. Sekitani, J. Reeder, T. Yokota, K. Kuribara, T. Tokuhara, M. Drack, R. Schwodiauer, I. Graz, S. Bauer-Gogonea, S. Bauer, T. Someya, An ultra-lightweight design for imperceptible plastic electronics, Nature, 499 (2013) 458-463.

[14] H.S. Wu, S. Kustra, E.M. Gates, C.J. Bettinger, Topographic substrates as strain relief features in stretchable organic thin film transistors, Org. Electron., 14 (2013) 1636-1642.

[15] S. Savagatrup, A.D. Printz, T.F. O'Connor, A.V. Zaretski, D. Rodriquez, E.J.

Sawyer, K.M. Rajan, R.I. Acosta, S.E. Root, D.J. Lipomi, Mechanical degradation and stability of organic solar cells: molecular and microstructural determinants, Energy Environ. Sci., 8 (2015) 55-80.

[16] F.C. Krebs, M. Biancardo, B. Winther-Jensen, H. Spanggard, J. Alstrup, Strategies for incorporation of polymer photovoltaics into garments and textiles, Sol. Energy Mater. Sol. Cells, 90 (2006) 1058-1067.

[17] D.J. Lipomi, B.C.-K. Tee, M. Vosgueritchian, Z.N. Bao, Stretchable Organic Solar Cells, Adv. Mater., 23 (2011) 1771-1775.

[18] J. Liang, L. Li, K. Tong, Z. Ren, W. Hu, X.F. Niu, Y.S. Chen, Q.B. Pei, Silver nanowire percolation network soldered with graphene oxide at room temperature and its application for fully stretchable polymer light-emitting diodes, ACS Nano, 8 (2014) 1590-1600.

[19] J.J. Liang, L. Li, X.F. Niu, Z.B. Yu, Q.B. Pei, Elastomeric polymer light-emitting devices and displays, Nat. Photonics, 7 (2013) 817-824.

[20] Z.B. Yu, X.F. Niu, Z. Liu, Q.B. Pei, Intrinsically stretchable polymer light-emitting devices using carbon nanotube-polymer composite electrodes, Adv. Mater., 23 (2011) 3989-3994.

[21] S. Savagatrup, A.D. Printz, H.S. Wu, K.M. Rajan, E.J. Sawyer, A.V. Zaretski, C.J. Bettinger, D.J. Lipomi, Viability of stretchable poly(3-heptylthiophene) (P3HpT) for organic solar cells and field-effect transistors, Synth. Met., 203 (2015) 208-214.

[22] S. Savagatrup, A.D. Printz, D. Rodriquez, D.J. Lipomi, Best of both worlds: Conjugated polymers exhibiting good photovoltaic performance and high tensile elasticity, Macromolecules, 47 (2014) 1981-1992.

[23] S. Savagatrup, D. Rodriquez, A.D. Printz, A. Sieval, J.C. Hummelen, D.J. Lipomi, [70]PCBM and incompletely separated grades of methanofullerenes produce bulk heterojunctions with increased robustness for ultra-flexible and stretchable electronics, Chem. Mater., 27 (2015) 3902-3911.

[24] Y.H. Zhou, C. Fuentes-Hernandez, J.W. Shim, J. Meyer, A.J. Giordano, H. Li, P. Winget, T. Papadopoulos, H. Cheun, J. Kim, M. Fenoll, A. Dindar, W. Haske, E. Najafabadi, T.M. Khan, H. Sojoudi, S. Barlow, S. Graham, J.L. Bredas, S.R. Marder, A. Kahn, B. Kippelen, A universal method to produce low-work function electrodes for organic electronics, Science, 336 (2012) 327-332.

[25] S. Savagatrup, E. Chan, S. Renteria-Garcia, A.D. Printz, A.V. Zaretski, T.F. O'Connor, D. Rodriquez, E. Valle, D.J. Lipomi, Plasticization of PEDOT:PSS by common additives for mechanically robust organic solar cells and wearable

sensors, Adv. Funct. Mater., 25 (2015) 427-436.

[26] M. Jorgensen, K. Norrman, S.A. Gevorgyan, T. Tromholt, B. Andreasen, F.C. Krebs, Stability of polymer solar cells, Adv. Mater., 24 (2011) 580-612.

[27] D.H. Kim, J.A. Rogers, Stretchable Electronics: Materials Strategies and Devices, Adv. Mater., 20 (2008) 4887-4892.

[28] J. Lee, J.A. Wu, M.X. Shi, J. Yoon, S.I. Park, M. Li, Z.J. Liu, Y.G. Huang, J.A. Rogers, Stretchable GaAs Photovoltaics with Designs That Enable High Areal Coverage, Adv. Mater., 23 (2011) 986-991.

[29] J.A. Fan, W.H. Yeo, Y.W. Su, Y. Hattori, W. Lee, S.Y. Jung, Y.H. Zhang, Z.J. Liu, H.Y. Cheng, L. Falgout, M. Bajema, T. Coleman, D. Gregoire, R.J. Larsen, Y.G. Huang, J.A. Rogers, Fractal design concepts for stretchable electronics, Nat. Comm., 5 (2014) 3266.

[30] D.H. Kim, N.S. Lu, R. Ma, Y.S. Kim, R.H. Kim, S.D. Wang, J. Wu, S.M. Won, H. Tao, A. Islam, K.J. Yu, T.I. Kim, R. Chowdhury, M. Ying, L.H. Xu, M. Li, H.J. Chung, H. Keum, M. McCormick, P. Liu, Y.W. Zhang, F.G. Omenetto, Y. Huang, T. Coleman, J.A. Rogers, Epidermal Electronics, Science, 333 (2011) 838-843.

CHAPTER 4 – THE LANGUAGE OF GLOVE: WIRELESS GESTURE DECODER WITH LOW-POWER AND STRETCHABLE HYBRID ELECTRONICS

Timothy F. O'Connor,[1] Matthew Fach,[2] Rachel Miller,[1] Samuel E. Root,[1] Patrick P. Mercier,[2] and Darren J. Lipomi[1]*

[1]*Department of NanoEngineering, University of California, San Diego, 9500 Gilman Drive, Mail Code 0448, La Jolla, CA 92093-0448*

[2]*Department of Electrical and Computer Engineering, University of California, San Diego, 9500 Gilman Drive, Mail Code, La Jolla, CA 92093-0409*

4.1 – ABSTRACT

This chapter describes a glove capable of wirelessly translating the American Sign Language (ASL) alphabet into text displayable on a computer or smartphone. The key components of the device are strain sensors comprising a piezoresistive composite of carbon particles embedded in a fluoroelastomer. These sensors are integrated with a wearable electronic module consisting of digitizers, a microcontroller, and a Bluetooth radio. Finite-element analysis predicts a peak strain on the sensors of 5% when the knuckles are fully bent. Fatigue studies suggest that the sensors successfully detect the articulation of the knuckles even when bent to their maximal degree 1,000 times. In concert with an accelerometer and pressure sensors, the glove is able to translate all 26 letters of the ASL alphabet. Lastly, data taken from the glove are used to control a virtual hand; this application suggests new ways in which stretchable and wearable electronics can enable humans to interface with virtual environments. Critically, this system was

constructed of components costing less than $100 and did not require chemical synthesis or access to a cleanroom. It can thus be used as a test bed for materials scientists to evaluate the performance of new materials and flexible and stretchable hybrid electronics.

4.2 – INTRODUCTION

This paper describes a sensor glove capable of converting hand gestures to text wirelessly using American Sign Language (ASL), and of controlling a virtual hand. The components of the entire system cost less than $100.00 (**SI Figure 23**) (excluding the laptop or smartphone). Low-cost, experimentally accessible platforms can allow laboratories to accelerate the discovery of materials designed to be integrated into whole devices in realistic scenarios.[1][2] The key enabling feature of the system is the use of a solution-processed, commercial conductive fluoroelastomer as a strain gauge that is stable over several months in the ambient air and over a thousand strain cycles. It is our hope that this material could play a role in stretchable hybrid electronics similar to the role played by poly(dimethylsiloxane) (PDMS) in soft lithography[3] and soft robotics.[4] That is, an inexpensive, commercially available material with reproducible properties in prototype devices.

Currently, the primary methods for tracking the positions of the human body[5] are through optical systems, by using an electromagnetic field, or by employing arrays of wearable sensors.[6] Optical systems comprising infrared emitters and receivers, in particular, have been successfully developed into systems for virtual reality and biomechanical analysis.[7][8] While these systems have low latencies and high spatial resolution, they require expensive and immovable infrastructure. Cameras, which make

systems for tracking mobile in either the visible or infrared regimes, have also been successfully implemented,[9] but such systems need to be positioned away from the human body, sometimes awkwardly to maintain line-of-sight, and further have large power requirements for sophisticated image acquisition and processing hardware. A portable, wearable system, in contrast, does not have these constraints. We chose a glove as the test-bed system because it is the archetypal form factor for intuitive human-machine interfaces. That is, unlike other remote controls (e.g., a mouse, game controller, keyboard, and joystick), gloves interface directly with human hands. A gesture-tracking glove could thus enable a more seamless interface for consumer electronics, virtual and augmented reality, telesurgery,[10] technical training,[11] and wearable devices for covert operations—from piloting areal drones[12] to controlling bomb-diffusing robots.[13]

Many approaches have been used to develop wearable strain sensors and to integrate them with computation and communication. Stretchable piezoresistive strain sensors made from patterned silicon nanomembranes,[14] composite nanomaterials,[15] conjugated polymers,[16] graphene,[17] and many other material systems[18] possess a number of desirable qualities such as ultra-thinness, flexibility or stretchablility,[19] or ease of fabrication by printing.[20] Work has begun to develop more complex systems that integrate stretchable circuitry,[21][22] sensing,[23] computation,[24] and communication,[25] as human-machine interfaces using systems of advanced materials. These systems employ pressure and capacitive transducers made of microcracked gold to measure the articulation of fingers,[26] composites of gold nanowires and polyaniline to control a robot arm,[15] patterned graphene heterostructures[27] and silver nanowires to control a virtual hand,[28] and carbon nanotubes for tracking human movement.[29] Such materials,

however, can require expensive starting materials and complex processing. An alternative approach using readily available materials would benefit the field. As a model application, we designed a system to translate the ASL alphabet because it requires a sophisticated integration of at least three types of sensors with electronics and data processing.

4.3 – MATERIALS AND METHODS

4.3.1 – FABRICATION OF PIEZORESISTIVE STRAIN SENSORS

A schematic diagram of the fabrication process is depicted in **SI Figure 24** Poly(dimethylsiloxane) (PDMS) (Dow Corning Slygard 184 with a base to cross-linker ratio of 20:1) was pour cast in a Petri dish and cured at 70 °C for 1 h. To create the substrate, the PDMS was cut into strips with dimensions 3 cm × 0.5 cm × 340 μm. Carbon paint (Ted Pella DAG-T-502) was then painted on produce a piezoresistive film roughly 50 μm in thickness. Copper tape was then wrapped around each end of the sensor while a stainless steel thread was added to provide a secure electrical contact. Additional carbon paint was added on top of the device to reinforce the mechanical and electrical interface. Finally, the strain sensor was dipped in 10% polyurethane (PU) in tetrahydrofuran (THF) to provide an encapsulating layer.

4.3.2 – CHARACTERIZATION OF STRAIN SENSORS

Stress strain curves were measured using a Mark 10 pull tester and electrical measurements were performed with a Keithley 2400 sourcemeter.

4.3.3 – FABRICATION OF THE SENSOR GLOVE

Nine piezoresistive sensors were fabricated and placed on the back of a leather athletic glove in locations corresponding with the metacarpal and proximal knuckles. Industrial strength, elastomeric adhesive E6000 (Eclectic Products, Inc) was used to bond the sensors to the glove. Conductive metal thread made from stainless steel was used to make the wearable circuits. E6000 was also used to adhere the thread and to insulate them from shorting with each other. Also using E6000, the custom designed PCB was adhered to the back of the leather glove on the Velcro strap to allow the wearer to easily put on and take off the glove.

4.3.4 – DESIGNING THE CIRCUIT BOARD

The circuit board was designed in EAGLE CAD and schematics can be found below in SI Figure 1. Schematics for the circuits on the PCB are found in **SI Figure 25 - 35**. The PCB was designed to carry an on/off switch, a battery, power regulators, resistors, capacitors, inputs for the Teensy 3.1, the BLE nrf8001, the MPU 6050, and nine voltage divider circuits. The gerber files (“gerber.zip”) are attached to the SI and the PCB board was fabricated at 4pcb.com.

4.3.5 – FINITE ELEMENT ANALYSIS

FEA models were produced in Autodesk Inventor, where the simulated sensor was deformed to the same radius of curvature as the wearable strain sensor (0.49 cm).

The bottom edges of both sides of the sensor were constrained while 1.05×10^{-3} Pa were applied to the bottom face in an upward direction.

4.3.6 – LETTER SELECTION

Letters were selected by monitoring the state of each sensor, assigning a 0 or 1 depending on the amount the finger was bent (0 for relaxed, 1 for bent). The individual numbers for each knuckle were then concatenated into a nine-digit code by summing powers of 10 (see code). For example, if the hand were completely relaxed, the code would read "000000000" and if a fist were formed, bending all knuckles, the code would be "111111111." Each letter was assigned a nine-digit key. The table used to determine which letter would be assigned which key is shown below in **SI Figure 36** and **SI Figure 37** shows the table for determining between degenerate letters. This image shows the table, the order of the sensors in building the key, and which letters have degenerate keys along with which hardware would be required to differentiate between those letters.

4.3.7 – CODE

The Teensy was coded in the Arduino IDE. This code is available upon for download at http://journals.plos.org/plosone/article?id=10.1371/journal.pone.0179766.

4.3.8 – VIRTUAL HAND

The glove sensor was interfaced with a virtual hand using a custom-built, object-oriented Python code. First, a twenty-four-node hand model was constructed in Cartesian coordinates. Each proximal and metacarpal knuckle was associated with three nodes to

form a joint object. Each joint object had a bending state associated with it, as well as a method for adjusting the bending state using a standard geometrical transformation. A simple algorithm was designed to take in the voltage signals from the Arduino (either through a serial port, or a text file) and match the bending state of each knuckle on the virtual hand to that of the real hand. The trajectory of the hand was saved to a file for subsequent visualization with the open visualization tool OVITO[30]. The code is openly available on the following github repository: https://github.com/seroot/Glove.

4.4 – RESULTS AND DISCUSSION

The key aspects of the system are illustrated in **Figure 19**. The system prototype was constructed on the dorsal side of a leather athletic glove and comprised two main components: one for sensing, and one for computation (**Figure 19a**). The sensing component used nine elastomeric strain sensors, placed over each metacarpal and proximal knuckle, and one pressure sensor placed on the thumb. The computation component, detailed in **Figure 19b**, employed a custom printed circuit board (PCB) that integrated a microprocessor (Teensy 3.1), Bluetooth low-energy chip (BLE 4.0 nRF8001), and 6-axis accelerometer/gyroscope (MPU 6050) (**Figure 19b**). The PCB also incorporated nine voltage divider circuits (**Figure 19c**), which were used to convert the dynamically-varying resistance of each strain sensor into a voltage. Conductive thread was used to connect each sensor to the PCB. A schematic diagram of the flow of information is depicted in **Figure 19d**. The process began with a physical gesture, whereby the bending of different knuckles exerted different amounts of strain on each of the sensors. When the fingers were bent, the sensors underwent a reversible increase in

their measured resistance. The complete process occurred in four steps: (1) a gesture was made and the strain sensors transduced the positions of the knuckles into variable resistance values; (2) the values of resistance were converted into voltages using the voltage dividers; (3) the Teensy microcontroller unit (MCU) measured each of the nine voltages and used them to generate a 9-bit binary key describing the state of each knuckle; and (4) the binary key was used to determine which letter was to be transmitted wirelessly. The computation was done onboard the wearable device to limit the amount of information that needed to be sent wirelessly and to keep the power consumption of the system low. An accelerometer and commercially available pressure sensor were added to enable the system to distinguish between letters with degenerate codes (E/S, G/L, H/K, R/U/V) or that required motion (I/J and D/Z). The glove was able to successfully determine all 26 letters of the alphabet.

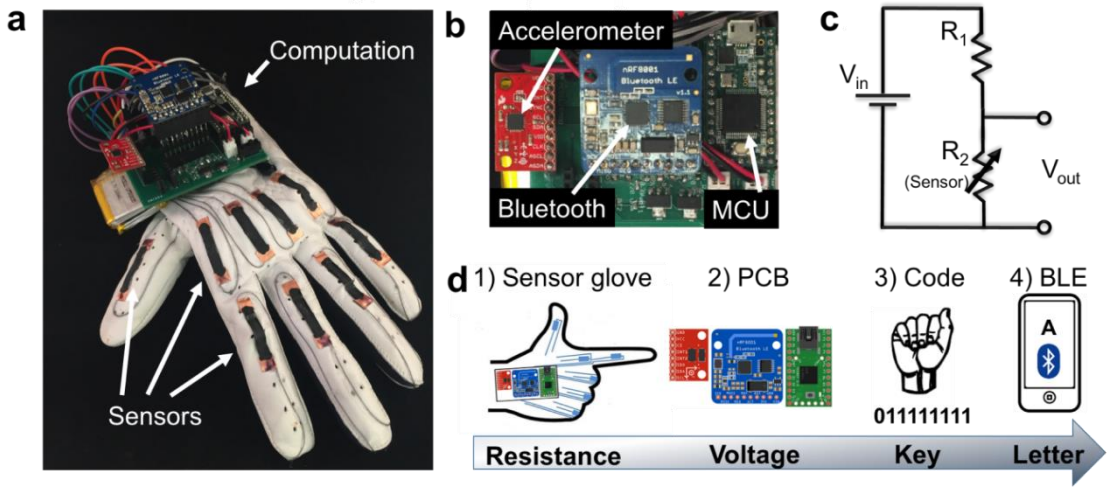

Figure 19: Overview of the gesture-decoding glove. (a) Photograph of the glove. (b) Photograph detailing the breakout boards for the MCU, accelerometer, and Bluetooth on the PCB. (c) A circuit diagram of a voltage divider. (d) Schematic drawing of wireless gesture recognition system and the flow of information. Step 1: a gesture was made and the strain sensors transduced the positions of the knuckles into variable resistance values. Step 2: the variable values of resistance were converted into voltages by the voltage dividers. Step 3: the MCU measured the nine voltages and, through a binary comparison process, used them to generate a nine-bit key. Step 4: the binary key was used to determine which letter was to be transmitted wirelessly.

To transduce the bending motions of the knuckles into an electrical signal, mechanically compliant strain sensors were fabricated using a commercially available conductive composite (DAG-T-502, Ted Pella, Inc.) as the piezoresistive material (**Figure 20a**). **Figure 20b** illustrates the device layers in an exploded view. The sensors were fabricated by painting the composite layer (~50 μm) onto a PDMS substrate (~350 μm). Copper tape and stainless steel thread were then added before encapsulating the device in polyurethane (PU, ~200 μm). The average total thickness of the devices was 616 μm ± 50.2 μm. The PU encapsulant increased the durability of the sensor against abrasion, reinforced the weak interface between the copper tape and carbon ink, and prevented the delamination of the piezoresistive layer and the PDMS substrate after repeated cycles of deformation. A scanning electron microscope (SEM) image of the

cross-sectional interface of the devices is shown in **Figure 20c**. Further magnification of the composite films (**Figure 20d**) shows that the piezoresistive layer consists of nanoscale carbon particles (~100 nm) connected by an amorphous, elastomeric network. The sensors were designed to be low-cost and easy to process, have an easily measureable change in resistance (ΔR) when bent on the knuckles, and to output a consistent electrical signal over many strain cycles without interfering with the movement of the glove.

Materials for the piezoresistive sensor were selected because of their mechanical durability, ease of processing, low cost and commercial availability. The DAG-T-502 was mechanically stable enough to accommodate the interface between the stretchable conducting material and the copper contacts. PDMS substrates were simple to cast as smooth, thin substrates and the PU encapsulant provided increased mechanical stability using a simple dip coating method. Both the PDMS substrate (20:1 base:crosslinker) and PU encapsulant have low tensile moduli, 1 MPa[31] and 7.5 MPa.[32] Conductive thread was used instead of metal wiring to better integrate the circuitry with textiles. Open-source electronics were chosen for their low cost, availability, and ease of integrating the whole system. The goal was thus to make rapid prototyping and testing of new materials and hybrid electronic devices a realistic process for research laboratories who may not be experts in electrical engineering.

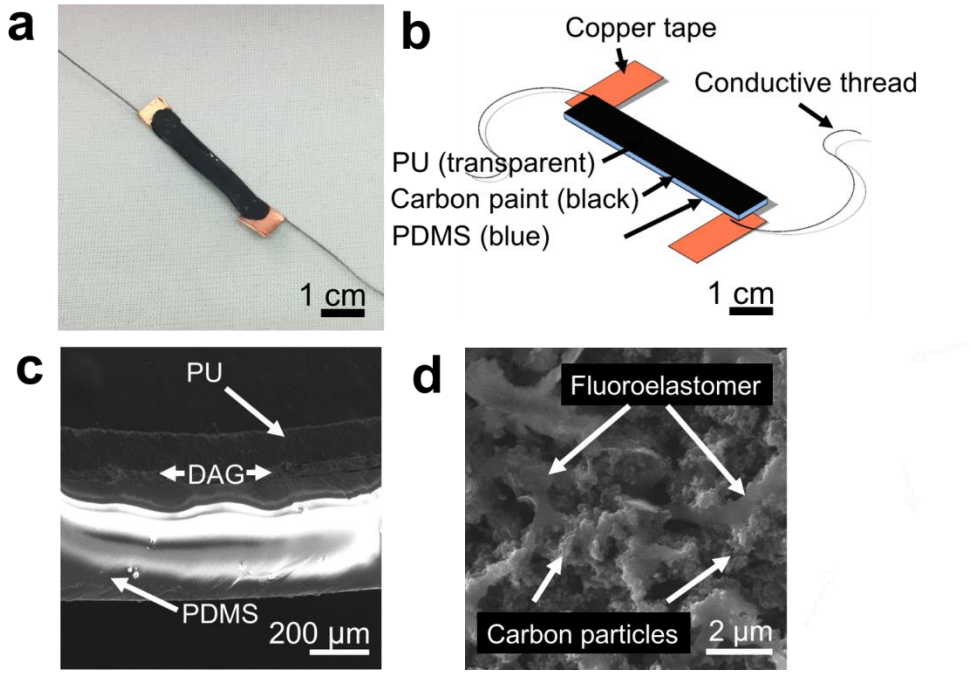

Figure 20: Overview of the wearable piezoresistive sensors. (a) Photograph of the sensor. (b) Schematic diagram of the sensor. (c) Cross-sectional optical micrograph of the sensor. (d) SEM image of the surface of the conductive fluoroelastomer.

To investigate the strain distribution and fatigue experienced by the sensors during bending, four sensors were selected for electromechanical characterization. The sensors were adhered to the middle metacarpal position of a glove and a fist was tightly formed. The induced deformation and strain produced an average increase in resistance from R_{unbent} 560 ± 120 Ω to R_{bent} 1120 ± 280 Ω, corresponding an increase of resistance of a factor of 2 (**Figure 21a, red curve**). (Variation between sensors was attributed to the hand painting of the piezoelectric carbon layer and the distribution of resistance values can easily be accounted for in the calibration of the sensor system.) The sensor was then removed from the glove and placed on a linear actuator where controlled amounts of strain were used to achieve the same increase in resistance (**Figure 21a, black curve**).

From this measurement, an average strain of 4.5 ± 1% was estimated across the sensor when the strain was applied linearly (**Figure 21b top**). Using FEA modeling, the strain distribution of a sensor under linear strain and of a sensor that was bent to the same radius of curvature as a knuckle-mounted sensor were simulated **(Figure 21b bottom)**. From the FEA model of the bent sensor, the peak strain was estimated to be around 5.5%.

Figure 21c (red curve) shows the experimentally measured non-linear resistance as a function of strain. Analysis of the stress-strain curve (**Figure 21c, black curve**) revealed a tensile modulus of 3.9 MPa and elastic behavior within the working range of the sensors. Though the modulus is still roughly 100 times that of skin,[33] the sensors are not perceptible by the user the through the glove, which is much stiffer than the sensors. Finally, the elastomeric sensors were repeatedly strained to their peak strain to determine the effect of fatigue on the electrical signal (**Figure 21d**). After 1,000 cycles, the relative change in resistance increased from 1.2 to 2.9, but the ability of the system to determine the correct letter was preserved, as the code responsible for letter detection is only dependent on the resistance exceeding a preset threshold voltage. In fact, a larger increase in resistance with strain potentially improve the ability to detect the letter, as it is the differences in resistance that matter.

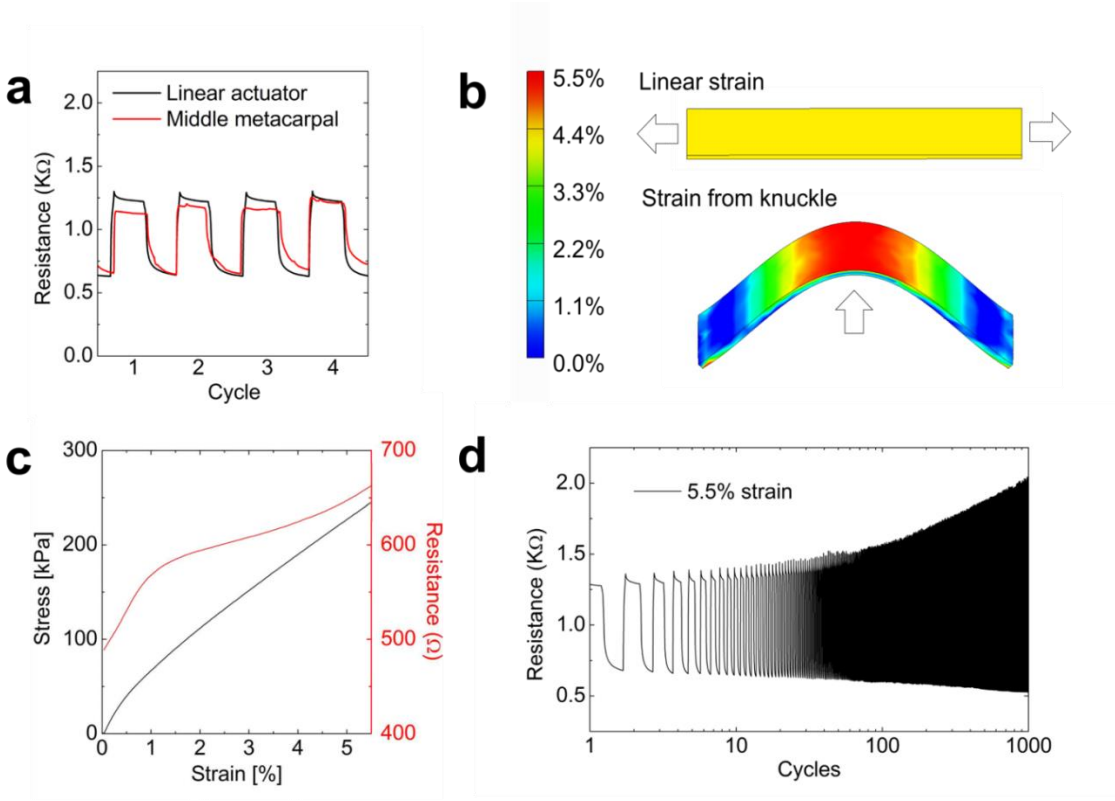

Figure 21: Characterization of the piezoresistance and FEA strain modeling of the sensors. (a) Resistance vs. strain of a representative strain sensor on the hand (red) and under controlled stretching conditions on a linear actuator (black). (b) Finite-element model simulating the strain distribution across the surface of the sensor in a linear stretching mode (top) and a knuckle strain regime (bottom). (c) Stress-strain (black) and resistance-strain (red) curves of the sensors measuring a tensile modulus of 3.9 MPa. (d) Resistance vs. strain of the same sample when cycled up to 1,000 times at 5.5%.

The MCU was programmed to determine the correct letter by generating a nine-digit binary key based on the on/off states of the nine sensors. The red curves in **Figure 22a** show the voltage values associated with each sensor as the hand signed the letters of the ASL alphabet in order. When the knuckle was bent, the value of resistance across the sensor (and thus the value of the voltage measured by the MCU) increased. If the value of the voltage was measured to be higher than that of the pre-programmed threshold value (dotted horizontal line in each chart), the sensor was assigned a 1. A knuckle not sufficiently bent was assigned a 0. A nine-digit key was then formed by concatenating the

individual values assigned to each sensor. **Figure 22b** shows the hand in configurations corresponding to the letters ‘U’ ‘C’ ‘S’ and ‘D’. These letters were sent wirelessly to a smartphone (**Figure 22c**). By feeding the serial output of the sensors into a model of a virtual hand, we were able to make a virtual hand reproduce the ASL sign gestures (**Figure 22d)**. Using an accelerometer and pressure sensor to enable the system to distinguish between letters with degenerate codes (E/S, G/L, H/K, R/U/V) or that required motion (I/J and D/Z), the glove was able to determine all 26 letters of the alphabet.

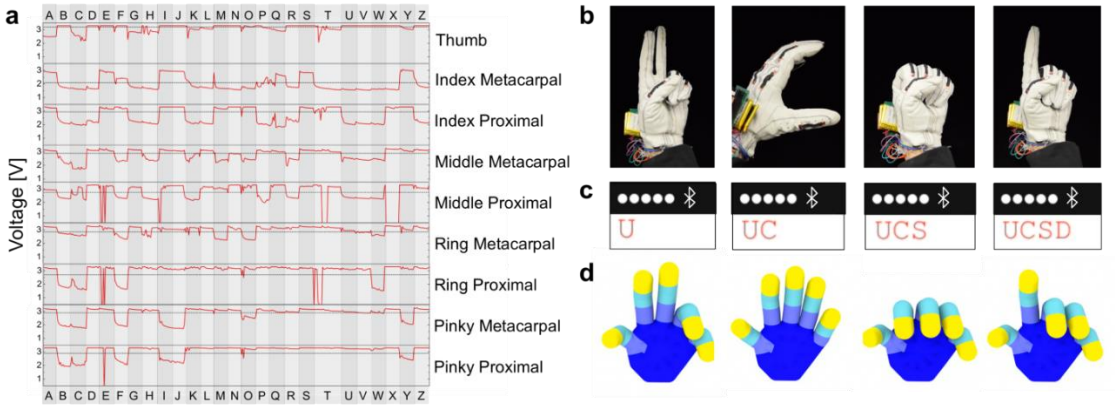

Figure 22: Process by which the glove converted gestures into the letters of ASL. (a) Voltage values associated with each knuckle while as the hand signs the letters of the ASL alphabet in order. Each sign was given ~30 s to form and hold the letter and, with the use of a pressure sensor and accelerometer, all 26 letters were successfully transcribed. The dotted lines represent the threshold value to determine the on/off state of the sensor. (b) Photographs of the hand in configurations corresponding to the ASL gestures for the letters ‘U’ ‘C’ ‘S’ and ‘D’. (c) Screen shots of a smartphone as the letters were received to construct a word. (d) Images of a virtual hand in which the bending state of each finger corresponded to the resistance values of the sensors.

4.5 – CONCLUSION

Through the integration of piezoresistive elastomers, open-source computation, and low-energy Bluetooth, we developed a low-cost system for decoding and transmitting human hand gestures. This system can serve as a test-bed platform for new materials, flexible hybrid electronics, and low-power circuits in human-machine interfaces. Attractive features of the system are low-cost (less than $100), modularity (the materials and components can be exchanged), and a complete description (in the Supporting Information), which will allow other laboratories to use the system. In particular, the stretchable conductive elastomer used as the piezoresistive sensors is commercially available and thus may play a similar role in stretchable electronics for human-machine interfaces as PDMS now plays in micropatterning and soft robotics. While the electronic components used to decode and transmit the data are modified from rigid, off-the-shelf components, there is an opportunity to make purpose-designed components in flexible, hybrid form factors. The materials and methods described here for the recognition of human gestures could also be applied to gather biometric and diagnostic data. The availability of open-sourced, test-bed systems can accelerate the development of materials and integration strategies for low-cost human-machine interfaces.

4.6 – SUPPORTING INFORMATION

4.6.1 – PARTS LIST AND COST

Part	Cost	Adjusted Cost	Provider
Leather sporting glove	$14.99	$14.99	Target
DAG-T-502 30 g	$9.65	≤ $1.00	Ted Pella Inc
PDMS 500 g	$47.42	≤ $1.00	Dow Corning
THF 1L	$56.20	≤ $1.00	Sigma Aldrich
PU 1 lb	$22.46	≤ $1.00	The Lubrizol Corporation
Copper tape 1 spool	$12.31	≤ $1.00	Amazon
Conductive thread 1 spool	$6.95	≤ $1.00	Adafruit
PCB	$33.00	$33.00	Advanced Circuits
Teensy 3.1	$19.95	$19.95	Amazon
Accelerometer MPU6050	$2.99	$2.99	eBay
Bluetooth nrf8001	$19.95	$19.95	Adafruit
Miscellaneous electronics	$5.00	$5.00	Amazon
Total	$250.87	$95.88	

Figure 23: Cost of parts to fabricate the sensor glove. Adjusted costs were estimated at $1.00 for cases in which a very small amount of the contents of the container indicated were used.

4.6.2 – FABRICATION SCHEMATIC OF PIEZORESISTIVE STRAIN SENSORS.

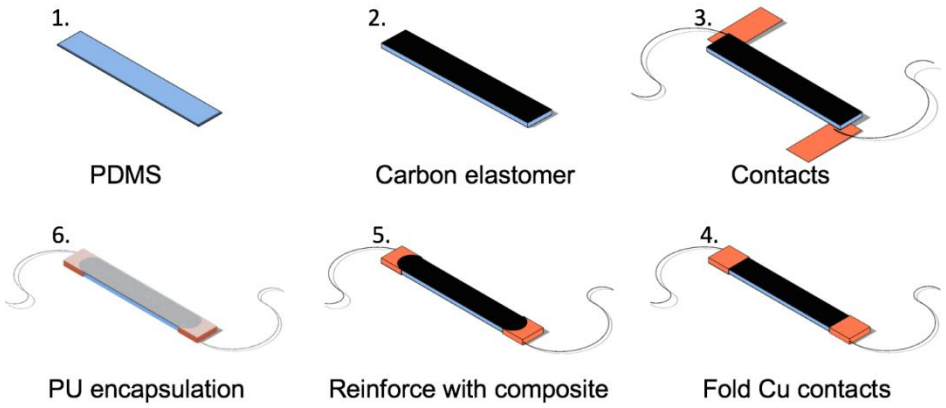

Figure 24: Fabrication schematic of the piezoresistive sensors.

4.7.3 PCB SCHEMATICS AND CIRCUIT DIAGRAMS

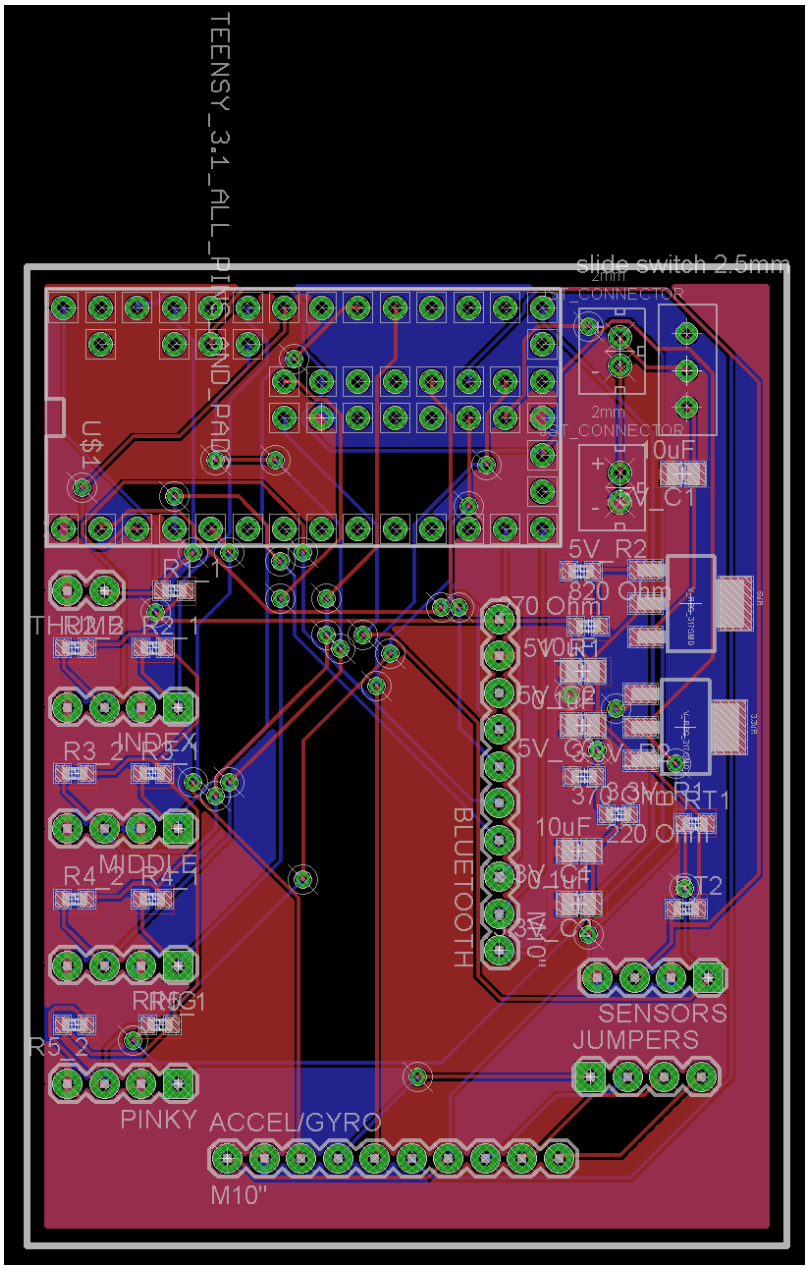

Figure 25: Image of the EAGLE CAD board.

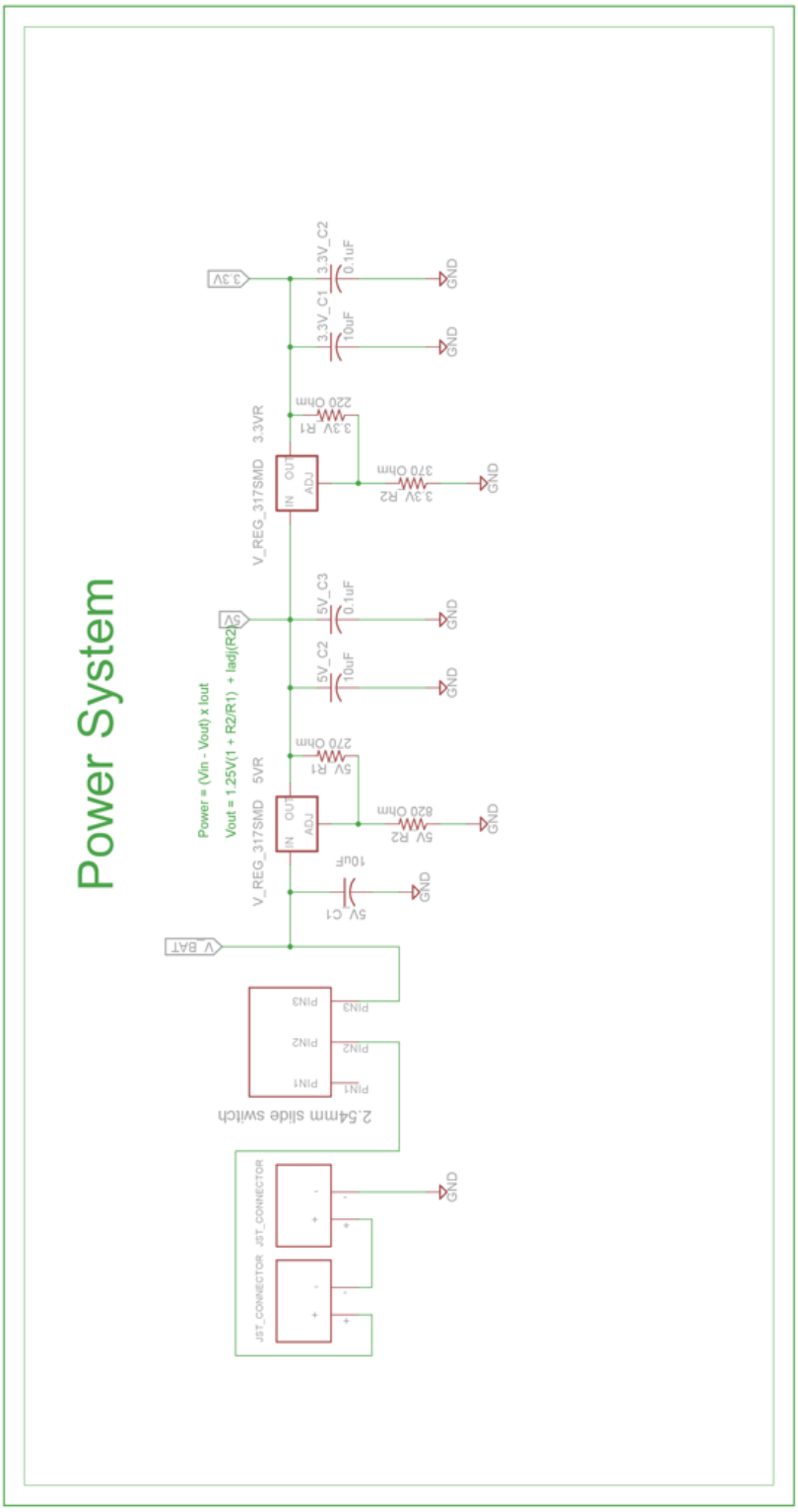

Figure 26: Image of the EAGLE CAD board.

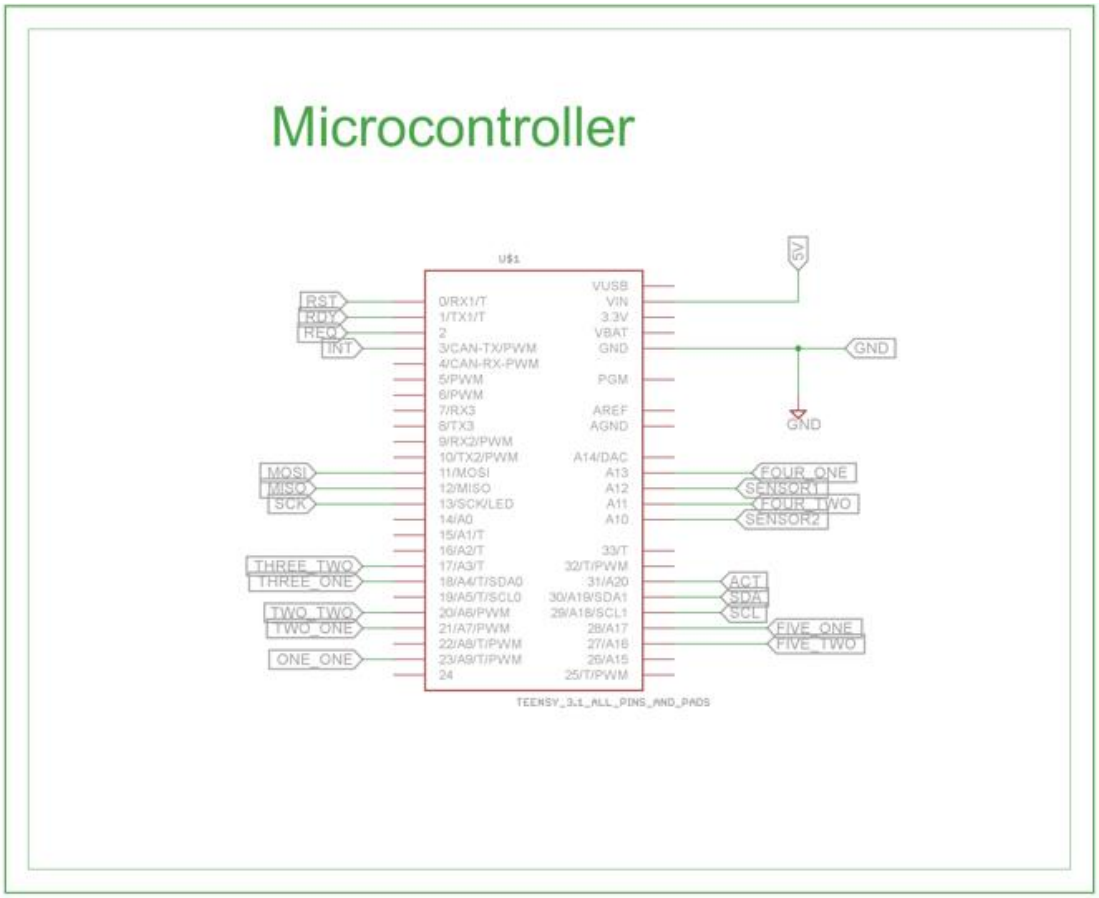

Figure 26: EAGLE CAD circuit schematic for the microcontroller.

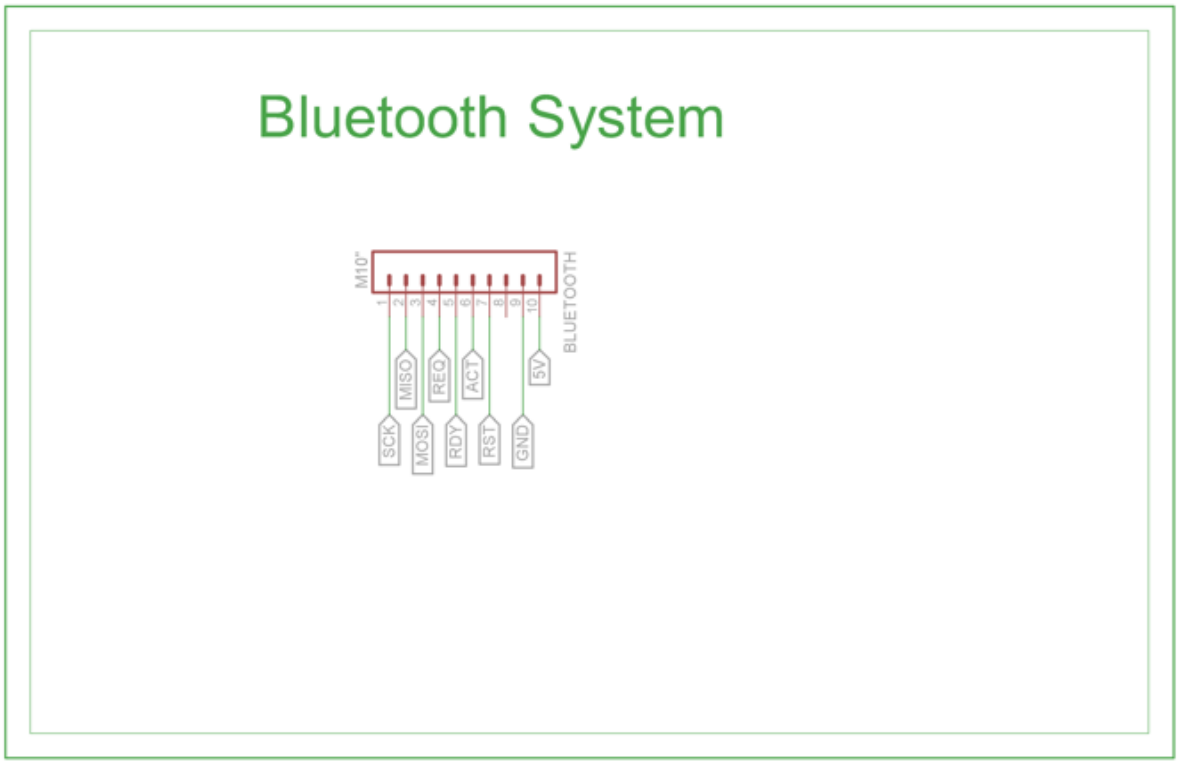

Figure 27: EAGLE CAD circuit schematic for the Bluetooth system.

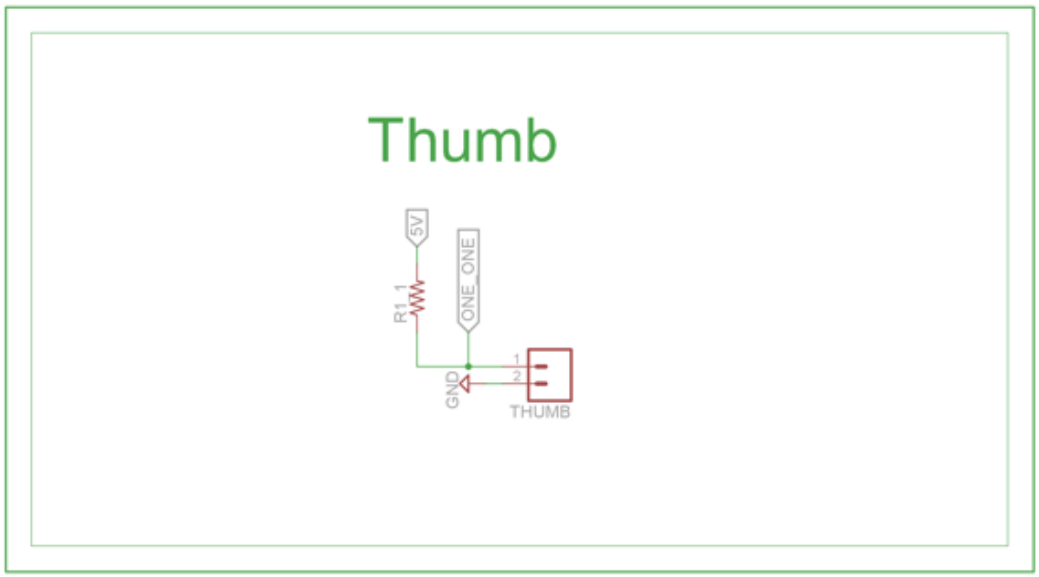

Figure 28: EAGLE CAD circuit schematic for the thumb sensor.

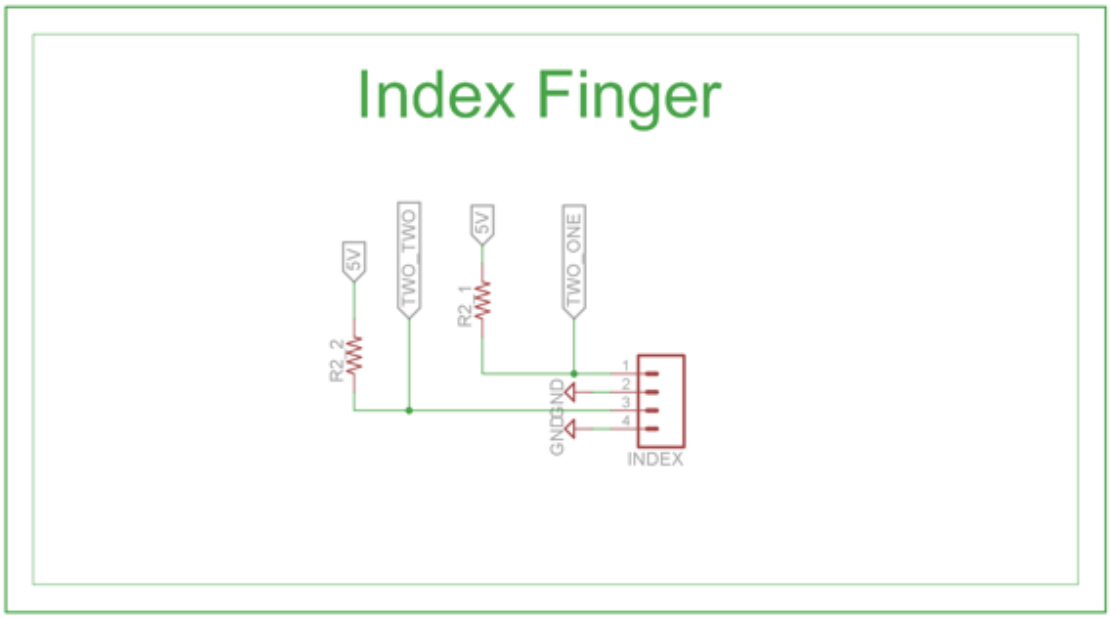

Figure 29: EAGLE CAD circuit schematic for the index sensors.

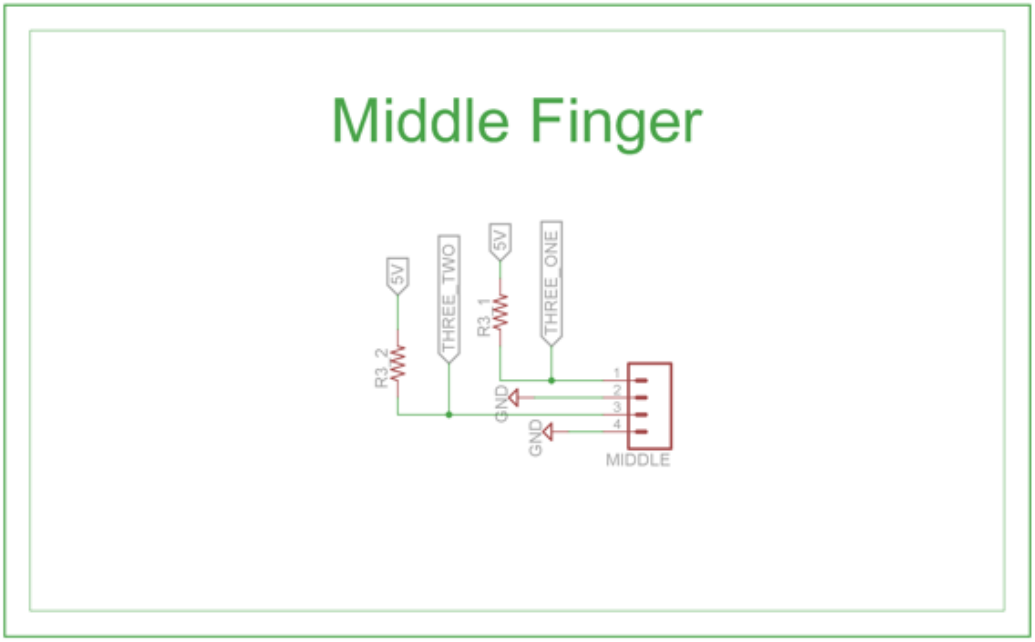

Figure 30: EAGLE CAD circuit schematic for the middle finger sensors.

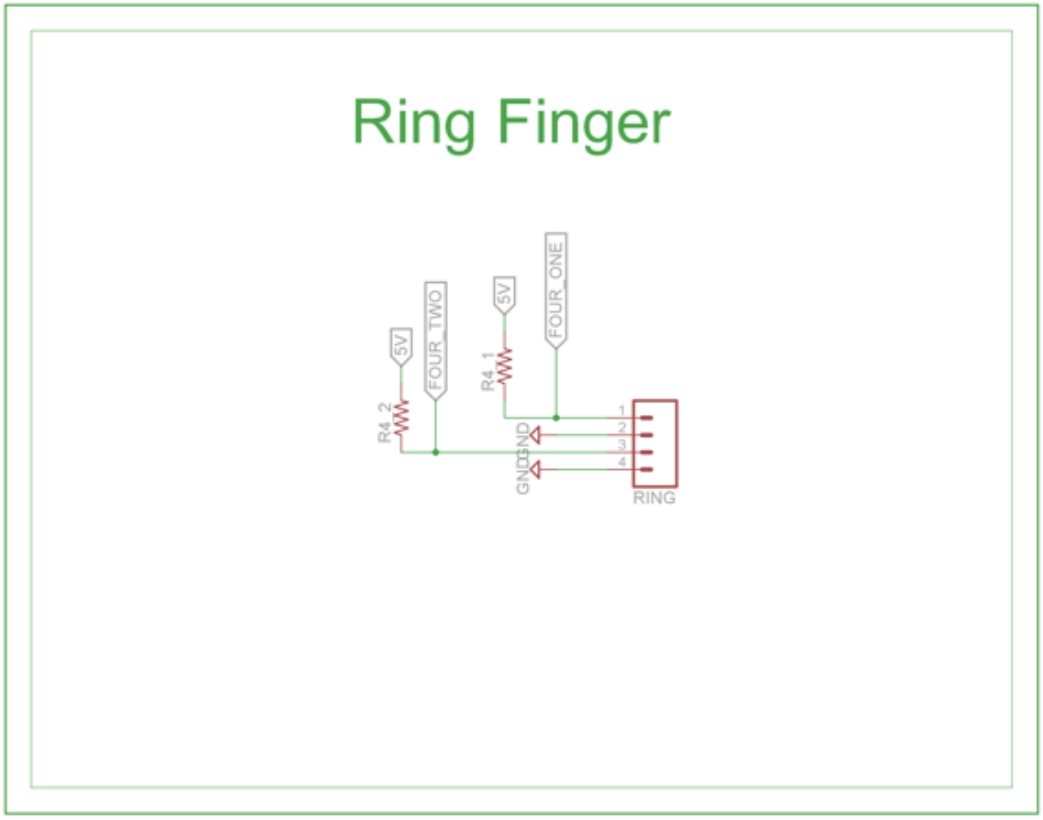

Figure 31: EAGLE CAD circuit schematic for the ring finger sensors.

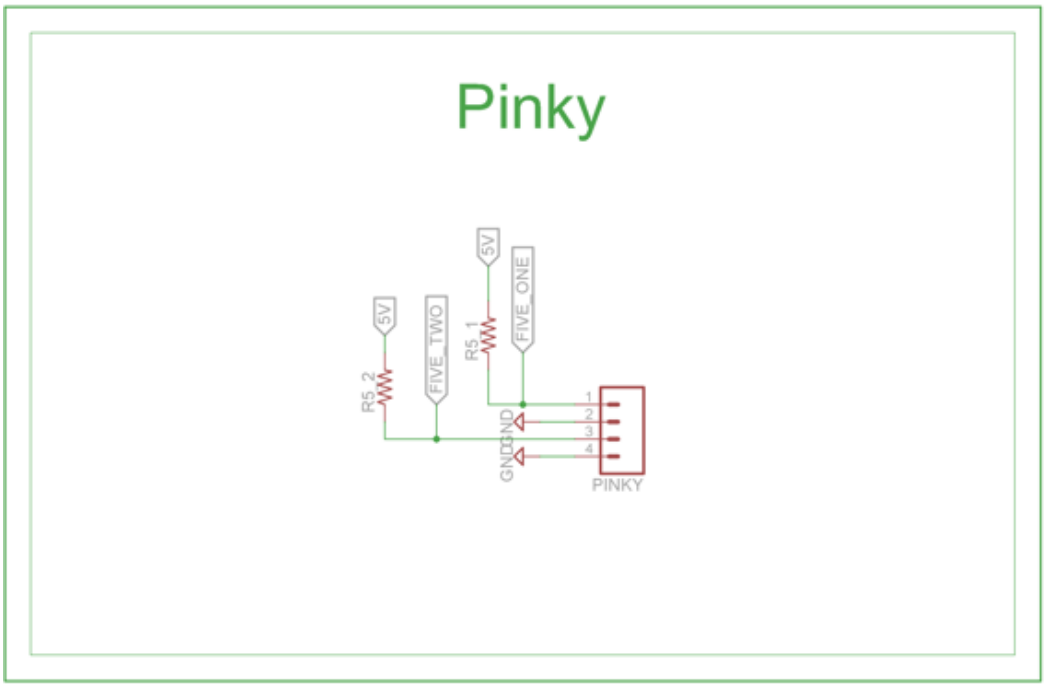

Figure 32: EAGLE CAD circuit schematic for the pinky sensor system.

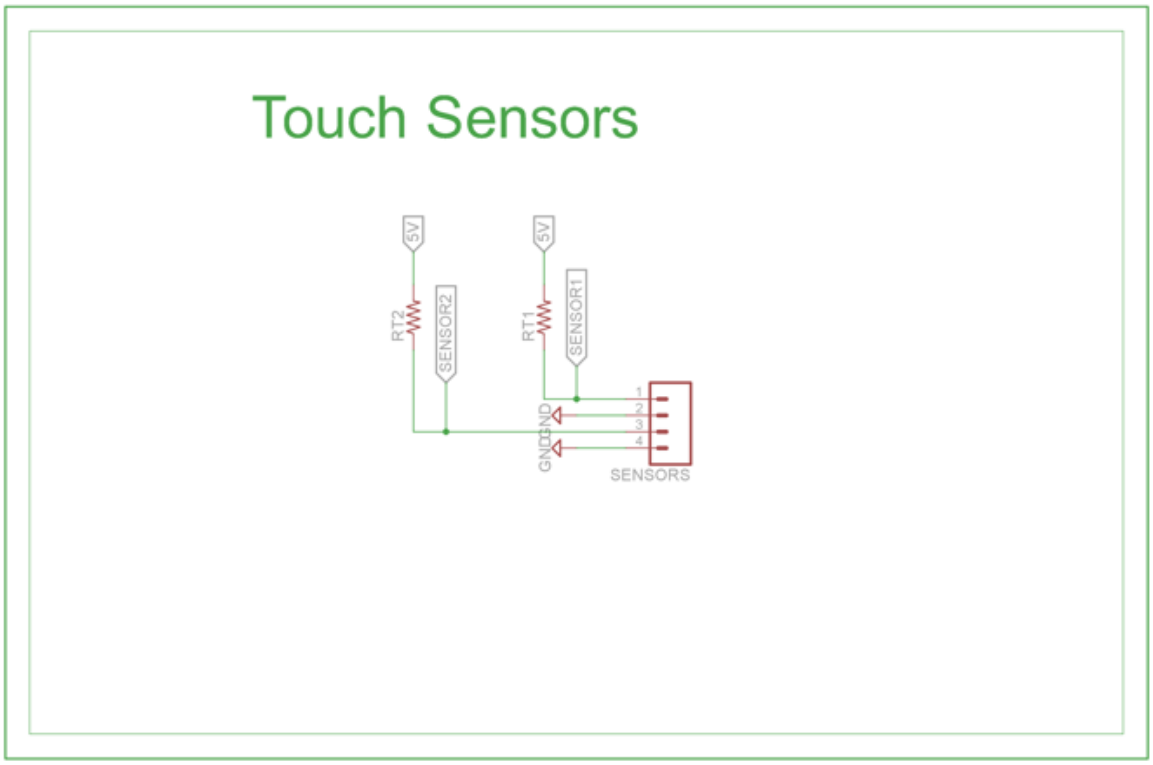

Figure 33: EAGLE CAD circuit schematic for the touch sensor (two were designed, only one was needed)

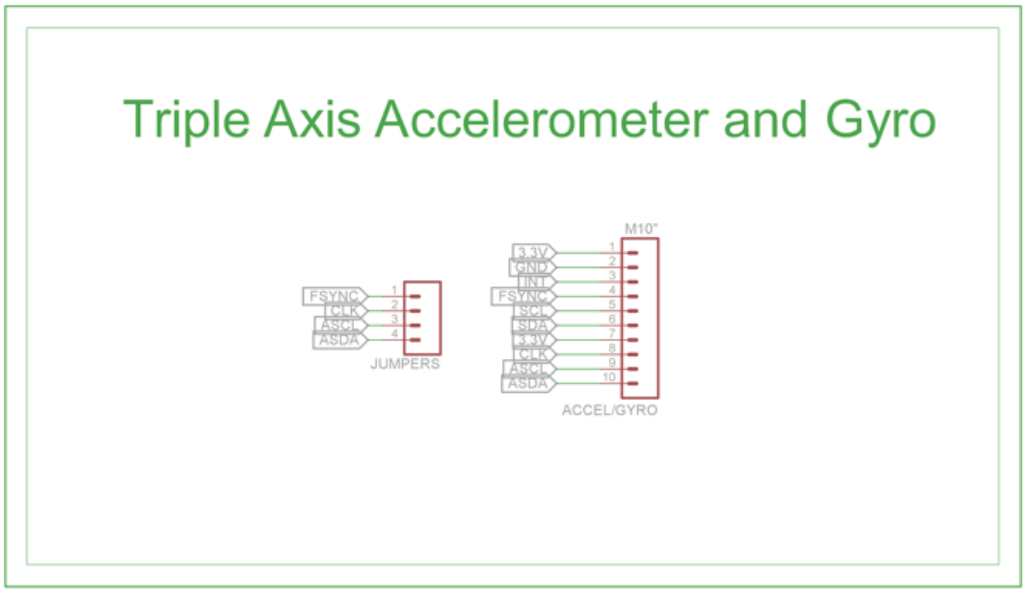

Figure 34: EAGLE CAD circuit schematic for the accelerometer/gyroscope.

4.6.4 – KEY GENERATION TABLE

	Thumb	I-meta	I-proxy	m-meta	m-proxy	r-meta	r-proxy	p-meta	p-proxy		number code		19 unique letters
A	0	1	1	1	1	1	1	1	1		11111111	11111111	Overlaps:
B	1	0	0	0	0	0	0	0	0		100000000	100000000	D = Z (accel)
C	0	0	0	0	0	0	0	0	0		0	0	G = L (pressure)
D	1	0	0	1	1	1	1	1	1		100111111	100111111	H = K (pressure)
E	0	1	1	1	1	1	1	1	1		111111111	111111111	I = J (accel)
F	1	1	1	0	0	0	0	0	0		111000000	111000000	U = V = R (pressure)
G	0	0	0	1	1	1	1	1	1		111111	111111	E = S (pressure)
H	0	0	0	0	0	1	1	1	1		1111	1111	
I	1	1	1	1	1	1	1	0	0		111111100	111111100	
J	1	1	1	1	1	1	1	0	0		111111100	111111100	
K	0	0	0	0	0	1	1	1	1		1111	1111	
L	0	0	0	1	1	1	1	1	1		111111	111111	
M	1	1	0	1	0	1	0	1	1		110101011	110101011	
N	1	1	0	1	0	1	1	1	1		110101111	110101111	
O	1	0	1	0	1	0	1	0	1		101010101	101010101	
P	0	0	0	1	0	1	1	1	1		101111	101111	
Q	0	1	0	1	1	1	1	1	1		10111111	10111111	
R	1	0	0	0	0	1	1	1	1		100001111	100001111	
S	1	1	1	1	1	1	1	1	1		111111111	111111111	
T	0	0	1	1	1	1	1	1	1		1111111	1111111	
U	1	0	0	0	0	1	1	1	1		100001111	100001111	
V	1	0	0	0	0	1	1	1	1		100001111	100001111	
W	1	0	0	0	0	0	0	1	1		100000011	100000011	
X	1	0	1	1	1	1	1	1	1		101111111	101111111	
Y	0	1	1	1	1	1	1	0	0		11111100	11111100	
Z	1	0	0	1	1	1	1	1	1		100111111	100111111	

Figure 35:. Key generation table indicating which letters correspond to which keys. The table also shows which letters have redundant keys and which type of hardware was used to differentiate those redundant letters.

4.6.5 – DEGENERATE LETTER DETERMINATION

Letter	T	IM	IP	MM	MP	RM	RP	PM	PP	Key	Accx	Pressure
D	3.30	2.07	2.57	3.06	3.30	3.30	3.24	3.30	3.30	100111111	**-57**	High
Z	3.30	2.00	2.61	3.04	3.30	3.30	3.21	3.30	3.30	100111111	**-18466**	high
E	3.30	3.16	3.30	3.23	3.30	3.30	3.30	3.30	3.30	111111111	-511	**high**
S	3.30	2.94	3.30	3.19	3.30	3.30	3.30	3.30	3.30	111111111	-448	**low**
G	3.13	2.04	2.59	3.19	3.30	3.30	3.26	3.30	3.30	000111111	-697	**low**
L	3.18	2.15	2.68	3.16	3.30	3.30	3.25	3.30	3.30	000111111	-860	**high**
H	3.05	1.98	2.71	3.03	2.96	3.30	3.25	3.30	3.30	000001111	-657	**low**
K	3.15	2.01	2.65	2.85	2.94	3.30	3.26	3.30	3.30	000001111	-411	**high**
I	3.30	3.00	3.30	2.83	3.30	2.91	2.08	3.22	2.33	111111100	**-74**	high
J	3.30	3.02	3.30	2.78	3.30	3.00	2.10	3.25	2.47	111111100	**-3652**	low
R	3.30	1.99	2.75	2.66	2.94	3.30	3.27	3.30	3.30	100001111	-661	**high**
U	3.30	1.99	2.79	2.61	2.93	3.30	3.25	3.30	3.30	100001111	-445	**low**
V	3.30	1.98	2.81	2.68	2.94	3.30	3.25	3.30	3.30	100001111	-637	**med**

Figure 36: Table depicting the serial outputs of the parameters used to differentiate between letters with degenerate keys. A pressure sensor was used to differentiate between E/S, G/L, H/K, and R/U/V while an accelerometer was used to decouple the letters D/Z and I/J. The threshold for the x-acceleration was set to |3000|, while the pressure sensor was set to Pressure = 3.3 for high, 3.3 > Pressure ≥ 1.0 for med, and 1.0 > Pressure for low.

4.7 – ACKNOWLEDGEMENTS

This work was supported by the National Institutes of Health Director's New Innovator Award number 1DP2EB022358-01. An earlier prototype of the device that used conductive polymers as the strain sensors, and from which we drew inspiration for the device in its current form was supported by the Air Force Office of Scientific Research Young Investigator Program grant number FA9550-13-1-0156. Additional support was provided by the Center for Wearable Sensors in the Jacobs School of Engineering at the University of California San Diego, and member companies Qualcomm, Sabic, Cubic, Dexcom, Honda, Samsung, and Sony. T. F. O. acknowledges support from the National Defense Science and Engineering Graduate fellowship program sponsored by the Office of Navy Research.

Chapter 4, in full, is a reprint of the material as it appears in "The Language of Glove: Wireless gesture decoder with low-power and stretchable hybrid electronics," Timothy F. O'Connor, Matthew Fach, Rachel Miller, Samuel E. Root, Patrick P. Mercier, and Darren J. Lipomi.PLoS ONE, 2017. The dissertation author was the primary investigator and author of this paper.

4.8 – REFERENCES

[1] Albert DR, Todt MA, Davis HF. A low-cost quantitative absorption spectrophotometer. J Chem Educ. 2012;89: 1432–1435. doi:10.1021/ed200829d

[2] Schausberger SE, Kaltseis R, Drack M, Cakmak UD, Major Z, Bauer S. Cost-Efficient Open Source Desktop Size Radial Stretching System With Force Sensor. IEEE Access. 2015;3: 556–561. doi:10.1109/ACCESS.2015.2433398

[3] Xia Y, Whitesides GM. Soft Lithography. Angew Chem Int Ed. 1998;37: 550–575. doi:10.1146/annurev.matsci.28.1.153

[4] Zhao H, O ’brien K, Li S, Shepherd RF. Optoelectronically innervated soft prosthetic hand via stretchable optical waveguides. Sci Robot. 2016;7529: eaai7529. doi:10.1126/scirobotics.aai7529

[5] Zhou H, Hu H. Human motion tracking for rehabilitation-A survey. Biomed Signal Process Control. 2008;3: 1–18. doi:10.1016/j.bspc.2007.09.001

[6] Zhou H, Stone T, Hu H, Harris N. Use of multiple wearable inertial sensors in upper limb motion tracking. Med Eng Phys. 2008;30: 123–133. doi:10.1016/j.medengphy.2006.11.010

[7] Maletsky LP, Sun J, Morton NA. Accuracy of an optical active-marker system to track the relative motion of rigid bodies. J Biomech. 2007;40: 682–685. doi:10.1016/j.jbiomech.2006.01.017

[8] Milne AD, Chess DG, Johnson JA, King G. Accuracy of an electromagnetic tracking device: A study of the optimal operating range and metal interference. J Biomech. 1996;29: 791–793. doi:10.1016/0021-9290(96)83335-5

[9] Mastorakis G, Makris D. Fall detection system using Kinect???s infrared sensor. J Real-Time Image Process. 2012;9: 635–646. doi:10.1007/s11554-012-0246-9

[10] Marescaux J, Leroy J, Gagner M, Rubino F, Mutter D, Vix M. Transatlantic robot-assisted telesurgery. Nature. 2001;413: 379–380. doi:10.1038/35096636

[11] Datta V, Mackay S, Mandalia M, Darzi A. The use of electromagnetic motion tracking analysis to objectively measure open surgical skill in the laboratory-based model. J Am Coll Surg. 2001;193: 479–485. doi:10.1016/S1072-7515(01)01041-9

[12] Nagi J, Giusti A, Di Caro GA, Gambardella LM. Human Control of UAVs using Face Pose Estimates and Hand Gestures. Proc 2014 ACM/IEEE Int Conf Human-robot Interact - HRI ’14. 2014; 252–253. doi:10.1145/2559636.2559833

[13] Lapides P, Sharlin E, Sousa MC. Three Dimensional Tangible User Interface for Controlling a Robotic Team. Human-Robot Interact (HRI), 2008 3rd ACM/IEEE Int Conf. 2008; 343–350. doi:10.1145/1349822.1349867

[14] Ying M, Bonifas AP, Lu N, Su Y, Li R, Cheng H. Silicon nanomembranes for fingertip electronics. Nanotechnology. 2012;23: 344004. doi:10.1088/0957-4484/23/34/344004

[15] Gong S, Lai DTH, Wang Y, Yap LW, Si KJ, Shi Q. Tattoolike Polyaniline Microparticle-Doped Gold Nanowire Patches as Highly Durable Wearable Sensors. ACS Appl Mater Interfaces. 2015;7: 19700–19708. doi:10.1021/acsami.5b05001

[16] Savagatrup S, Chan E, Renteria-Garcia SM, Printz AD, Zaretski A V., O’Connor

TF. Plasticization of PEDOT:PSS by common additives for mechanically robust organic solar cells and wearable sensors. Adv Funct Mater. 2015;25: 427–436. doi:10.1002/adfm.201401758

[17] Yan C, Wang J, Kang W, Cui M, Wang X, Foo CY. Highly stretchable piezoresistive graphene-nanocellulose nanopaper for strain sensors. Adv Mater. 2014;26: 2022–2027. doi:10.1002/adma.201304742

[18] Park J, You I, Shin S, Jeong U. Material approaches to stretchable strain sensors. ChemPhysChem. 2015;16: 1155–1163. doi:10.1002/cphc.201402810

[19] Sekitani T, Someya T. Stretchable, large-area organic electronics. Adv Mater. 2010;22: 2228–2246. doi:10.1002/adma.200904054

[20] Muth JT, Vogt DM, Truby RL, Meng???? Y, Kolesky DB, Wood RJ. Embedded 3D printing of strain sensors within highly stretchable elastomers. Adv Mater. 2014;26: 6307–6312. doi:10.1002/adma.201400334

[21] Akter T, Kim WS. Reversibly stretchable transparent conductive coatings of spray-deposited silver nanowires. ACS Appl Mater Interfaces. 2012;4: 1855–1859. doi:10.1021/am300058j

[22] Lin Y, Cooper C, Wang M, Adams JJ, Genzer J, Dickey MD. Handwritten, Soft Circuit Boards and Antennas Using Liquid Metal Nanoparticles. Small. 2015;11: 6397–6403. doi:10.1002/smll.201502692

[23] Wang T, Guo Y, Wan P, Zhang H, Chen X, Sun X. Flexible Transparent Electronic Gas Sensors. Small. 2016; 3748–3756. doi:10.1002/smll.201601049

[24] Ch EAR. Re s ear ch | r e p o r t s. 2008;21.

[25] Haj-Omar A, Thompson WL, Kim YS, Glick P, Tolley M, Coleman TP. Stretchable and flexible adhesive-integrated antenna for biomedical applications. 2016 IEEE Antennas Propag Soc Int Symp APSURSI 2016 - Proc. 2016; 459–460. doi:10.1109/APS.2016.7695938

[26] Gerratt AP, Michaud HO, Lacour SP. Elastomeric electronic skin for prosthetic tactile sensation. Adv Funct Mater. 2015;25: 2287–2295. doi:10.1002/adfm.201404365

[27] Lim S, Son D, Kim J, Lee YB, Song JK, Choi S. Transparent and stretchable interactive human machine interface based on patterned graphene heterostructures. Adv Funct Mater. 2015;25: 375–383. doi:10.1002/adfm.201402987

[28] Amjadi M, Pichitpajongkit A, Lee S, Ryu S, Park I. Highly stretchable and sensitive strain sensor based on silver nanowire-elastomer nanocomposite. ACS Nano. 2014;8: 5154–5163. doi:10.1021/nn501204t

[29] Yamada T, Hayamizu Y, Yamamoto Y, Yomogida Y, Izadi-Najafabadi A, Futaba DN. A stretchable carbon nanotube strain sensor for human-motion detection. Nat Nanotechnol. Nature Publishing Group; 2011;6: 296–301. doi:10.1038/nnano.2011.36

[30] Stück R, Burger M, Hohage T. The iteratively regularized Gauss–Newton method with convex constraints and applications in 4Pi microscopy. Inverse Probl. 2012;28: 15012. doi:10.1088/0266-5611/28/1/015012

[31] Wang Z, Volinsky AA, Gallant ND. Nanoindentation study of polydimethylsiloxane elastic modulus using berkovich and flat punch tips. J Appl Polym Sci. 2015;132: 1–7. doi:10.1002/app.41384

[32] Nunes RCR, Fonseca JLC, Pereira MR. Polymer-filler interactions and mechanical properties of a polyurethane elastomer. Polym Test. 2000;19: 93–103. doi:10.1016/S0142-9418(98)00075-0

[33] Pailler-Mattei C, Bec S, Zahouani H. In vivo measurements of the elastic mechanical properties of human skin by indentation tests. Med Eng Phys. 2008;30: 599–606. doi:10.1016/j.medengphy.2007.06.011